



Calhoun: The NPS Institutional Archive
DSpace Repository

Theses and Dissertations

1. Thesis and Dissertation Collection, all items

2006-12

Direct electric field visualization in semiconductor planar structures

Andrikopoulos, Pavlos

Monterey California. Naval Postgraduate School

<http://hdl.handle.net/10945/2398>

Downloaded from NPS Archive: Calhoun



Calhoun is a project of the Dudley Knox Library at NPS, furthering the precepts and goals of open government and government transparency. All information contained herein has been approved for release by the NPS Public Affairs Officer.

Dudley Knox Library / Naval Postgraduate School
411 Dyer Road / 1 University Circle
Monterey, California USA 93943

<http://www.nps.edu/library>



NAVAL POSTGRADUATE SCHOOL

MONTEREY, CALIFORNIA

THESIS

**DIRECT ELECTRIC FIELD VISUALIZATION
IN SEMICONDUCTOR PLANAR STRUCTURES**

by

Pavlos Andrikopoulos

December 2006

Thesis Advisor:
Co-Advisor:

Nancy M. Haegel
David Jenn

Approved for public release; distribution is unlimited

THIS PAGE INTENTIONALLY LEFT BLANK

REPORT DOCUMENTATION PAGE			Form Approved OMB No. 0704-0188	
Public reporting burden for this collection of information is estimated to average 1 hour per response, including the time for reviewing instruction, searching existing data sources, gathering and maintaining the data needed, and completing and reviewing the collection of information. Send comments regarding this burden estimate or any other aspect of this collection of information, including suggestions for reducing this burden, to Washington headquarters Services, Directorate for Information Operations and Reports, 1215 Jefferson Davis Highway, Suite 1204, Arlington, VA 22202-4302, and to the Office of Management and Budget, Paperwork Reduction Project (0704-0188) Washington DC 20503.				
1. AGENCY USE ONLY (Leave blank)		2. REPORT DATE December 2006	3. REPORT TYPE AND DATES COVERED Master's Thesis	
4. TITLE AND SUBTITLE Direct Electric Field Visualization in Semiconductor Planar Structures			5. FUNDING NUMBERS	
6. AUTHOR(S) Pavlos Andrikopoulos				
7. PERFORMING ORGANIZATION NAME(S) AND ADDRESS(ES) Naval Postgraduate School Monterey, CA 93943-5000			8. PERFORMING ORGANIZATION REPORT NUMBER	
9. SPONSORING / MONITORING AGENCY NAME(S) AND ADDRESS(ES) National Science Foundation Division of Materials Research (DMR)			10. SPONSORING/MONITORING AGENCY REPORT NUMBER	
11. SUPPLEMENTARY NOTES The views expressed in this thesis are those of the author and do not reflect the official policy or position of the Department of Defense or the U.S. Government.				
12a. DISTRIBUTION / AVAILABILITY STATEMENT Approved for public release; distribution is unlimited			12b. DISTRIBUTION CODE	
13. ABSTRACT (maximum 200 words) A new technique for imaging the 2D transport of free charge in semiconductor structures is used to directly map electric field distributions in operating devices. Direct transport imaging is demonstrated in a scanning electron microscope, using an optical microscope and a high sensitivity charge coupled device. Transport behavior under the combined influence of both diffusion and drift is predicted by modeling the drift and diffusion in 2D following generation at a point source. This is the first demonstration of a technique that allows the mapping of the electric field by determining not only the direction but especially the magnitude of the electric field with high resolution. The measured results show excellent agreement with theoretical predictions simulated with COMSOL software. The transport imaging technique also allows measurement of the contact resistance in a new way that is non-destructive and based on a two-point contact only. The technique illustrates the device's characteristics by determining the exact activation point of the diode and the deviations from an ideal I-V behavior. The method is extremely useful since the complexity and miniaturization of current devices do not allow for multiple wiring that standard four point measurement demands. Finally, a suggestion for further research of the effects of electromigration by using the direct transport imaging technique is offered. The latter is a subject of high importance in electronic device reliability.				
14. SUBJECT TERMS Diffusion, Direct Transport Imaging Technique, Drift, Electric Field Mapping, Minority Carrier Lifetime, Minority Carrier Mobility, Semiconductors			15. NUMBER OF PAGES 145	
			16. PRICE CODE	
17. SECURITY CLASSIFICATION OF REPORT Unclassified	18. SECURITY CLASSIFICATION OF THIS PAGE Unclassified	19. SECURITY CLASSIFICATION OF ABSTRACT Unclassified	20. LIMITATION OF ABSTRACT UL	

NSN 7540-01-280-5500

Standard Form 298 (Rev. 2-89)
Prescribed by ANSI Std. Z39-18

THIS PAGE INTENTIONALLY LEFT BLANK

Approved for public release; distribution is unlimited

**DIRECT ELECTRIC FIELD VISUALIZATION
IN SEMICONDUCTOR PLANAR STRUCTURES**

Pavlos Andrikopoulos
Major, Hellenic Army
B.S., Hellenic Military Academy, 1992

Submitted in partial fulfillment of the
requirements for the degree of

**MASTER OF SCIENCE IN APPLIED PHYSICS
and
MASTER OF SCIENCE IN SYSTEMS ENGINEERING**

from the

**NAVAL POSTGRADUATE SCHOOL
December 2006**

Author: Pavlos Andrikopoulos

Approved by: Nancy M. Haegel
Thesis Advisor

David Jenn
Co-Advisor

James H. Luscombe
Chairman, Department of Physics

Dan C. Boger
Chairman, Department of Information Sciences

THIS PAGE INTENTIONALLY LEFT BLANK

ABSTRACT

A new technique for imaging the 2D transport of free charge in semiconductor structures is used to directly map electric field distributions in operating devices. Direct transport imaging is demonstrated in a scanning electron microscope, using an optical microscope and a high sensitivity charge coupled device. Transport behavior under the combined influence of both diffusion and drift is predicted by modeling the drift and diffusion in 2D following generation at a point source. This is the first demonstration of a technique that allows the mapping of the electric field by determining not only the direction but especially the magnitude of the electric field with high resolution. The measured results show excellent agreement with theoretical predictions simulated with COMSOL software.

The transport imaging technique also allows measurement of the contact resistance in a new way that is non-destructive and based on a two-point contact only. The technique illustrates the device's characteristics by determining the exact activation point of the diode and the deviations from an ideal I-V behavior. The method is extremely useful since the complexity and miniaturization of current devices do not allow for multiple wiring that standard four point measurement demands.

Finally, a suggestion for further research of the effects of electromigration by using the direct transport imaging technique is offered. The latter is a subject of high importance in electronic device reliability.

THIS PAGE INTENTIONALLY LEFT BLANK

TABLE OF CONTENTS

I.	INTRODUCTION.....	1
A.	DIRECT TRANSPORT IMAGING AND ELECTRIC FIELD VISUALIZATION IN SEMICONDUCTOR PLANAR STRUCTURES ...	1
B.	MILITARY RELEVANCE	3
C.	THESIS OVERVIEW	4
II.	BACKGROUND.....	7
A.	CONDUCTION IN SEMICONDUCTORS	7
B.	DOUBLE-HETEROSTRUCTURE (DH) DEVICE	8
C.	CARRIER TRANSPORT PHENOMENA.....	10
D.	LUMINESCENCE PHENOMENA IN SEMICONDUCTORS.....	13
E.	CATHODOLUMINESCENCE.....	15
F.	CATHODOLUMINESCENCE INTENSITY	16
III.	EXPERIMENTAL APPROACH.....	19
A.	DIRECT TRANSPORT IMAGING	19
B.	SCANNING ELECTRON MICROSCOPE (SEM)	20
1.	SEM Components	20
2.	SEM Basic Parameters	22
3.	Electron Beam-Specimen Interactions	22
4.	SEM Imaging Process	25
a.	<i>Picture Mode</i>	25
b.	<i>Line Mode</i>	26
c.	<i>Spot Mode</i>	27
5.	Laboratory's SEM	27
C.	AlGaAs/GaAs/AlGaAs HETEROSTRUCTURE SAMPLE	28
D.	SIMULATIONS.....	31
1.	DC Modeling.....	31
2.	AC Modeling.....	36
IV.	ELECTRIC FIELD DISTRIBUTIONS: SIMULATION AND MEASUREMENT	43
A.	2-D ELECTRIC FIELD SIMULATIONS.....	43
1.	Case 1	43
2.	Case 2	48
3.	Case 3	52
4.	Case 4	56
5.	Case 5	60
6.	Case 6	64
B.	VISUALIZATION OF THE ELECTRIC FIELD.....	68
C.	COMSOL MULTIPHYSICS	72
V.	APPLICATIONS OF THE TRANSPORT IMAGING TECHNIQUE	75
A.	CONTACT RESISTANCE MEASUREMENTS	75

1.	Case 1	75
2.	Case 2	82
B.	COMPARISON OF ELECTRIC FIELD MAGNITUDE DETERMINED EXPERIMENTALLY TO COMSOL MODELING	89
C.	EVALUATION OF THE ELECTRIC FIELD MAGNITUDE IN SEMICONDUCTOR PLANAR STRUCTURES OF CONSTRICTED GEOMETRY	91
VI.	CONCLUSIONS AND SUGGESTIONS FOR FURTHER RESEARCH	97
A.	SUMMARY AND CONCLUSION	97
B.	SUGGESTIONS FOR FURTHER RESEARCH	99
1.	Reliability of Semiconductor Devices	99
2.	Electromigration Issues	100
	APPENDIX A. MATLAB CODE FOR EVALUATING THE DC MATHEMATICAL MODEL	105
	APPENDIX B. MATLAB CODE FOR MAPPING ELECTRIC FIELD VIA TRANSPORT IMAGING TECHNIQUE	109
	APPENDIX C. MATLAB CODE FOR EVALUATION OF CONTACT RESISTANCE	115
	APPENDIX D. MATLAB CODE FOR COMSOL DATA	123
	LIST OF REFERENCES.....	125
	INITIAL DISTRIBUTION LIST	127

LIST OF FIGURES

Figure 1.	Double-Heterostructure Diode. {After [3]}.	8
Figure 2.	Energy Band Diagram with no bias. {After [3]}.	9
Figure 3.	Energy Band Diagram with forward bias. {After [3]}.	9
Figure 4.	Direct and Indirect Energy Band Diagram. {After [3]}.	13
Figure 5.	Indirect Energy Band Diagram with Recombination Center. {After [3]}.	14
Figure 6.	The depth-dose curves for Si. {From [5]}.	16
Figure 7.	Spot mode imaging in a p-type AlGaAs/GaAs/AlGaAs heterostructure in two different cases of applied electric field [(a) and (b) 216 μm X 190 μm].	19
Figure 8.	Electron Column.	20
Figure 9.	Control Console.	21
Figure 10.	Deflection system inside the SEM. {From [6]}.	22
Figure 11.	Major electron beam parameters. {From [6]}.	22
Figure 12.	Interaction Volume for a 20 keV beam striking Si. {From [7]}.	23
Figure 13.	Picture Mode image with application of 15V AC in a p-type AlGaAs/GaAs/AlGaAs heterostructure (874 μm X 589 μm).	26
Figure 14.	Line Scan Mode image with application of 15V DC in a p-type AlGaAs/GaAs/AlGaAs heterostructure (872 μm X 293 μm).	26
Figure 15.	Spot Mode image with application of 15V DC in a specific point of a p-type AlGaAs/GaAs/AlGaAs heterostructure (216 μm X 190 μm).	27
Figure 16.	JEOL 840A SEM.	28
Figure 17.	SEM Overall Schematic Operation and Components {From [9]}.	28
Figure 18.	AlGaAs/GaAs/AlGaAs heterostructure sample.	29
Figure 19.	Part of Sample #9 Structure (3482 μm X 2611 μm).	31
Figure 20.	Intensity distribution in x, y direction based on simulation for DC applied field.	33
Figure 21.	Simulation for varying values of DC applied field.	34
Figure 22.	Intensity ratio vs. applied electric field based on simulation for DC applied field.	35
Figure 23.	Curve fitting for DC field simulation.	36
Figure 24.	Intensity distribution in x, y direction based on simulation for AC applied field.	37
Figure 25.	Simulation for varying values of AC applied field.	38
Figure 26.	Comparison of normalized intensity ratios for different times.	39
Figure 27.	Intensity ratio vs. applied electric field based on simulation for AC applied field.	40
Figure 28.	Curve fitting for AC field simulation.	40
Figure 29.	Comparison of DC and AC simulation models for E-field amplitude of 209.50E-4 V/ μm .	41
Figure 30.	Sample #9 - Case 1.	44

Figure 31.	Normalized intensity ratio vs. Distance for Case 1 (DC applied field).....	45
Figure 32.	E-Field vs. Distance for Case 1 (DC applied field).....	45
Figure 33.	Normalized intensity ratio vs. Distance for Case 1 (AC applied field).....	46
Figure 34.	E-Field vs. Distance for Case 1 (AC applied field).....	46
Figure 35.	Comparison of the results of magnitude of electric field with DC and AC bias for Case 1.	47
Figure 36.	Sample #9 - Case 2.....	48
Figure 37.	Normalized intensity ratio vs. Distance for Case 2 (DC applied field).....	49
Figure 38.	E-Field vs. Distance for Case 2 (DC applied field).....	49
Figure 39.	Normalized intensity ratio vs. Distance for Case 2 (AC applied field).....	50
Figure 40.	E-Field vs. Distance for Case 2 (AC applied field).....	50
Figure 41.	Comparison of the results of magnitude of electric field with DC and AC bias for Case 2.	51
Figure 42.	Sample #9 - Case 3.....	52
Figure 43.	Normalized intensity ratio vs. Distance for Case 3 (DC applied field).....	52
Figure 44.	E-Field vs. Distance for Case 3 (DC applied field).....	53
Figure 45.	Sample #9 (Reversed cabling and polarity).....	53
Figure 46.	Normalized intensity ratio vs. Distance for Case 3 (DC applied field, reversed cabling and polarity).	54
Figure 47.	E-Field vs. Distance for Case 3 (DC applied field, reversed cabling and polarity).....	54
Figure 48.	Comparison for Case 3 results (DC applied field, reversed cabling and polarity).....	55
Figure 49.	Sample #9 (SEM photo) – Case 4 (2031 μm X 2090 μm).	56
Figure 50.	Sample #9 – Case 4 (Created in COMSOL MULTIPHYSICS).	56
Figure 51.	Normalized intensity ratio vs. Distance for Case 4 (DC applied field).....	57
Figure 52.	E-Field vs. Distance for Case 4 (DC applied field).....	57
Figure 53.	Normalized intensity ratio vs. Distance for Case 4 (AC applied field).....	58
Figure 54.	E-Field vs. Distance for Case 4 (AC applied field).....	58
Figure 55.	Comparison of the results of magnitude of electric field with DC and AC bias for Case 4.	59
Figure 56.	Sample #9 (SEM photo) – Case 5 (2031 μm X 2090 μm).	60
Figure 57.	Sample #9 – Case 5 (Created in COMSOL MULTIPHYSICS).	60
Figure 58.	Normalized intensity ratio vs. Distance for Case 5 (DC applied field).....	61
Figure 59.	E-Field vs. Distance for Case 5 (DC applied field).....	61
Figure 60.	Normalized intensity ratio vs. Distance for Case 5 (AC applied field).....	62

Figure 61.	E-Field vs. Distance for Case 5 (AC applied field).....	62
Figure 62.	Comparison of the results of magnitude of electric field with DC and AC bias for Case 5.	63
Figure 63.	Sample #9 (SEM photo) – Case 6 (2031 μm X 2090 μm).	64
Figure 64.	Sample #9 – Case 6 (Created by COMSOL MULTIPHYSICS).	64
Figure 65.	Normalized intensity ratio vs. Distance for Case 6 (DC applied field).....	65
Figure 66.	E-Field vs. Distance for Case 6 (DC applied field).....	65
Figure 67.	Normalized intensity ratio vs. Distance for Case 6 (AC bias).	66
Figure 68.	E-Field vs. Distance for Case 6 (AC bias).	66
Figure 69.	Comparison of the results of magnitude of electric field with DC and AC bias for Case 6.	67
Figure 70.	DC and AC bias comparison (different scaling).	67
Figure 71.	Direction of the electric field with SEM in line mode (874 μm X 589 μm).	68
Figure 72.	Line mode in defining the direction of the electric field (each image is 872 μm X 293 μm).	69
Figure 73.	Various cases of direction of diffusion length according to the applied voltage (each image is 874 μm X 589 μm).....	70
Figure 74.	Various positions of electron beam (spot mode) in Sample #9 (874 μm X 589 μm).....	71
Figure 75.	Direction of the electric field in case 5 based on the positions specified in Figure 74 for DC bias (each image is 266 μm X 239 μm).	71
Figure 76.	Direction of the electric field in case 5 based on the positions specified in Figure 74 for AC bias (each image is 266 μm X 239 μm).	72
Figure 77.	Configuration of Sample #9 for defining the contact resistance with 2-point measurement (2090 μm X 2031 μm).....	75
Figure 78.	COMSOL simulation of the electric field potential for Case 1.....	76
Figure 79.	COMSOL simulation of the electric field (x-component) for Case 1. ..	77
Figure 80.	COMSOL simulation of the electric field (y-component) for Case 1. ..	77
Figure 81.	COMSOL simulation of the electric field (z-component) for Case 1. ..	78
Figure 82.	Electric field (x-component) for Case 1.....	79
Figure 83.	Electric field (y-component) for Case 1.....	79
Figure 84.	Electric field (z-component) for Case 1.....	80
Figure 85.	Total electric field for Case 1.....	80
Figure 86.	Intensity ratio vs. applied voltage for Case 1.....	81
Figure 87.	Electric field vs. applied voltage for Case 1.....	82
Figure 88.	Configuration of Sample #9 for defining the drop of voltage between the contacts with 2-point measurement.	83
Figure 89.	COMSOL simulation of the electric field potential for Case 2.....	83
Figure 90.	COMSOL simulation of the electric field (x-component) for Case 2. ..	84
Figure 91.	COMSOL simulation of the electric field (y-component) for Case 2. ..	84
Figure 92.	COMSOL simulation of the electric field (z-component) for Case 2. ..	85

Figure 93.	Electric field (x-component) for Case 2.....	85
Figure 94.	Electric field (y-component) for Case 2.....	86
Figure 95.	Electric field (z-component) for Case 2.....	86
Figure 96.	Total electric field for Case 2.....	87
Figure 97.	Intensity ratio vs. applied voltage for Case 2.....	88
Figure 98.	Electric field vs. applied voltage for Case 2.....	88
Figure 99.	Electric field vs. applied voltage for Case 2 (log-log scale).....	89
Figure 100.	Part of Sample #9 for comparison of the COMSOL simulation with the experimental method.....	90
Figure 101.	Comparison of the electric field as a function of position for 15 V DC applied bias.....	90
Figure 102.	Part of Sample #9 with special geometry characteristics.....	91
Figure 103.	Spot mode images at point of charge generation with zero bias (a), +7 V DC bias (b) and -7 V DC bias (c).	92
Figure 104.	SEM operation in line mode for Sample #9 for the case study.	92
Figure 105.	Line mode images (vertical red line) with zero bias (a), +7 V DC bias (b) and -7 V DC bias (c).	93
Figure 106.	Line mode images (horizontal green line) with zero bias (a), +7 V DC bias (b) and -7 V DC bias (c).	93
Figure 107.	E-Field vs. distance for points along (in the direction shown) of the red vertical line of Figure 104 with – 7 V DC applied bias.	94
Figure 108.	E-Field vs. distance for points along (in the direction shown) of the green horizontal line of Figure 104 with – 7 V DC applied bias.	94
Figure 109.	Areas of interest for determination of the electric field behavior.	95
Figure 110.	SEM images in spot mode operation for point charge generation.	98
Figure 111.	Sample #9 for electromigration study (each image is 874 μm X 589 μm).	100
Figure 112.	E-Field values with respect to time due to temperature increase.	101
Figure 113.	Points with high injected charge density (each image is 247 μm X 215 μm).	102
Figure 114.	Part of Sample #9 for studying the effects of thermal excitation (874 μm X 589 μm).	103
Figure 115.	E-Field values vs. times of power cycling.	104

LIST OF TABLES

Table 1.	Selected Semiconductor Materials.....	8
Table 2.	Selected Elements of the Periodic Table.....	8
Table 3.	Parameters for the evaluation of DC model for the simulation of diffusion/ drift behavior in x and y direction.....	32
Table 4.	Parameters for the evaluation of DC model for the simulation of diffusion/ drift behavior.	34
Table 5.	Parameters for the evaluation of AC model for the simulation of diffusion/ drift behavior in x and y direction.....	37
Table 6.	Parameters for the evaluation of AC model for the simulation of diffusion/ drift behavior.	38

THIS PAGE INTENTIONALLY LEFT BLANK

ACKNOWLEDGMENTS

I would first like to express my deep appreciation to my thesis advisor Dr. Nancy M. Haegel for her continuous efforts, guidance and support for more than a year, while working for my thesis. The every-day interaction with her in our laboratory, the free exchange of ideas and the direct responses to all my questions – concerns were invaluable, constituting simultaneously a unique learning experience. The challenge of selecting a thesis topic that is based on experimental work, acquaintance with high-tech instruments and combination of physical, mathematical and numerical ideas and analysis is tremendous and the objective tasks seem sometimes unreachable. Her help was the “bridge” to overcome all my problems and for her contribution I feel extremely lucky that I had her for my advisor. I would also like to express my sincere appreciation to my thesis co-advisor Dr. David Jenn for his important contribution to the completion of this thesis.

Additionally I would like to thank Dr. Thomas Boone at Hitachi Global Storage for his remarks and recommendations for my work, Jeff Beeman at Lawrence Berkeley National Laboratory for manufacturing the various samples that I have worked on, Dr. Matt Coleman and Mike Talmadge of Fairfield University for their help concerning the mathematical simulation models used in this thesis and Captain David R. Luber (USMC) for his work that was my starting point and a valuable reference during my thesis work.

This work was supported by the National Science Foundation through Grants DMR-0203397 and DMR-0526330.

I would like to express my appreciation to Dr. Bill Maier and Donald Snyder for allowing me freely to use the COMSOL MULTIPHYSICS software in their laboratory, helping me simultaneously to get familiar with it.

I am grateful to the Hellenic Army General Staff for giving me the opportunity to expand my knowledge in this institute and the NPS faculty that I had the chance to have them as instructors, for their continuous and great effort to promote teaching and research ideas to a higher level.

Finally, I would like to thank my wife, Iliana, for her understanding, patience and support for the whole period of my studies in the Naval Postgraduate School and my mother, Meropi, for teaching me to try every day to be a better man.

I. INTRODUCTION

A. DIRECT TRANSPORT IMAGING AND ELECTRIC FIELD VISUALIZATION IN SEMICONDUCTOR PLANAR STRUCTURES

Electro-optics is the field of systems that convert photons to electrons regardless of the wavelength [1]. Detectors are used across the full range of electromagnetic (EM) spectrum, with special military interest in the near or short wave infrared [(SWIR), 0.7-2 μm], in the midwave infrared [(MWIR), 3-5 μm] and in the long-wavelength infrared [(LWIR), 8-12 μm] regions. The sensitivity of these detectors of photons and of high energy particles depend on the generation and subsequent motion and collection of free charge. Similarly, a wide range of devices depend upon the fabrication of contacts that can uniformly inject and remove charge. New efforts in materials and devices must be accompanied by improved understanding of local transport behavior [2].

In particular it is of high importance to be able to directly image the injection and motion of free charge with high resolution since a macroscopic current-voltage measurement is based on the averaging of local transport behavior. Various techniques have been adopted in order to study the luminescent phenomena and transport properties of structures used in sensor device manufacture. The work described in this thesis is based on cathodoluminescence scanning electron microscopy, which allows for spatial characterization of light emission.

In this thesis, a technique for imaging the 2D transport of free charge in planar semiconductor structures has been developed in our laboratory [2]. This technique is used to image the motion of minority carriers in a heavily doped p-type AlGaAs/GaAs/AlGaAs heterostructure, under a range of applied electric fields. The laboratory's scanning electron microscope (SEM) is a JEOL 840A with an internal optical microscope, connected to an external thermoelectrically cooled charge coupled device (CCD) camera. An electron beam is generated through thermionic emission and interacts with the specimen, creating electron-

hole pairs and finally the emission of photons. By generating charge at a fixed point, it is possible to monitor the subsequent drift and diffusion by imaging the distribution of the free carrier recombination path [2].

The main objective of this thesis is to demonstrate electric field mapping by determining not only the direction but especially the magnitude of the field locally. In order to determine the extent to which transport imaging can be used to map local electric fields with high resolution, charge motion as a function of applied electric field has been imaged. Transport behavior under the combined influence of both diffusion and drift is predicted by modeling the drift and diffusion in 2D following generation at a point source. Subsequent measurements of electric field profiles have been done in both uniform (parallel plate structure) and non-uniform regions.

With the method mentioned above it is also possible to measure the contact resistance in a new way. In order to be able to define the applied electric field strength in an area where drift measurements take place, a four point measurement is an efficient way. The disadvantage of the method is that the complexity and small size of newly manufactured semiconductor planar devices does not allow multiple wiring for additional current carrying and voltage measuring probes. By applying the electron beam in the uniform region between two metal contacts superjacent to semiconductor material, study of the transport behavior under the influence of both diffusion and drift at the point source in a range of applied voltage allows accurate measurement of the contact resistance with only two-point wiring. The technique illustrates the device's characteristics by determining the "turn on voltage" of the diode and further deviations from an ideal linear I-V behavior.

Finally, an investigation of electric field distributions relevant to electromigration has been started for potential future applications. In particular, an effort to generate electromigration in a specimen has been performed in order to study how the electric field profiles of specific devices are affected in an Electronic Warfare environment (e.g., radiation from electronic attack).

Nevertheless, the characteristics of the interaction between current carriers and migrating atoms are not entirely understood. Further applications of the direct transport imaging technique can be used for future study of the electromigration. The latter is currently a subject of high importance in electronic device reliability.

B. MILITARY RELEVANCE

The detector is the component of the sensor system which transforms the optical signal into an electrical signal. The spectral response is determined by the detector characteristics and the operating temperature. The sensitivity of the material used (threshold wavelength) is determined by its energy bandgap (E_g). The wavelength of a photon has to be short enough so that the photon energy exceeds a material's bandgap energy level for absorption. Intrinsic detectors are constructed with semiconductor crystals with no introduced impurities or lattice defects, while extrinsic detectors have impurities introduced in order to change the effective bandgap energy [1].

In the case of photon or quantum detectors, the change in charge carrier state changes the electrical properties of the material indicating the amount of incident optical power. Depending on their characteristics, photon detectors can be distinguished as photoconductive, photovoltaic and photoemissive devices [1]. From all the above it is obvious that the key component of each type of detector is the semiconductor material that converts the absorbed photon in the desired electrical signal.

Military systems for target detection, ranging and remote observation are highly dependent upon advanced photonic and optoelectronic devices. It is critical that these devices are highly sensitive, reliable and cost effective in operation. The military, along with all other sectors of the economy, has benefited greatly from the advances in semiconductor technology over recent decades.

New demands constantly require new devices. Recent examples would include the production of lasers and LEDs for the blue and UV parts of the spectrum, improved radiation sensors for room temperature operation, high temperature materials, such as SiC and GaN, for demanding environments and

the renewed interest in terahertz detectors for explosive detection. In all these cases, new materials and new contact technologies must be developed.

In this development process, characterization tools are required that provide the needed information in a cost effective, timely manner. The characterization tool that is developed and tested in this thesis will provide a means for direct characterization of new nanostructures and other devices that are being considered for next generation electronics. In addition, because it utilizes a scanning electron microscope, which is an existing tool for high throughput, commercial applications, the technique has the potential to provide rapid, large scale transport characterization. This could reduce the cost of new devices by providing early, device-critical feedback with a characterization tool that requires minimal device processing.

Finally, device reliability in operation requires a full understanding of material defects as well as the interaction of material with the environment, such as in the radiation behavior of devices in space. This technique has the potential to provide detailed defect characterization of devices during operation. By mapping the electric field on a micron scale, early indication can be obtained of future failure modes. As will be demonstrated, this technique has the potential to measure local electric fields at about 10% variation, providing a very sensitive measure of developing defect behavior that could ultimately affect device scale performance. This capability is essential due to miniaturization of the current devices and the complexity of the influence that various defects have on their electrical behavior.

C. THESIS OVERVIEW

Chapter I states the purpose of the thesis providing an overview of the experimental technique of direct transport imaging in order to locally map and measure the electric field in semiconductor planar structures. Chapter II provides background information concerning the physics of semiconductor materials and luminescent phenomena in semiconductors and an overview of cathodoluminescence. Chapter III describes the experimental approach of the

cathodoluminescence scanning electron microscopy followed in the current work. It includes a description of the laboratory's equipment, the specimen used, the overall procedure and the mathematical models used. In Chapter IV, a number of cases are illustrated in order to demonstrate the validity and potential of the method described in Chapter III. In Chapter V, a potential method of evaluating the contact resistance with a new two-point measurement has been presented. Additionally, in the same chapter, a method of evaluating the electric field magnitude in semiconductor planar structures with constricted geometry has been presented. Chapter VI refers to electromigration issues and provides conclusions and suggestions for future work.

THIS PAGE INTENTIONALLY LEFT BLANK

II. BACKGROUND

A. CONDUCTION IN SEMICONDUCTORS

In semiconductors, there are two types of free charge carriers: electrons and holes. A hole is effectively an empty electronic state in the valence band (VB) that behaves as if it were a positively charged particle free to respond to an applied electric field. Free electrons that exist in the conduction band (CB) can also move in the crystal and contribute to the electrical conduction when an electric field is applied.

When small amounts of impurities are introduced into an otherwise pure crystal structure, it is possible to obtain a semiconductor in which the concentration of carriers of one polarity is much in excess of the other type. This kind of semiconductor is called an extrinsic semiconductor. If the impurities have a smaller valency than the equivalent of the pure semiconductor material, the result is an excess of holes over electrons. This is a p-type semiconductor. A characteristic example is the p-type material created by Si doped with B, Si:B.

Si has $Z=14$ and electronic structure $[\text{Ne}]3s^2p^2$ and B has $Z=5$ and electronic structure $[\text{He}]2s^2p^1$. It can be seen that B has three valence electrons and Si four valence electrons. So, when B shares its valence electrons with four Si atoms, one of the bonds has a missing electron which is a hole. This effective empty state in the valence band results in the characterization of B as an acceptor (electron acceptor) impurity as it accepts an additional electron in order to form four covalent bonds around it. The primary material used in this thesis is GaAs:Be which is, according to the above, a p-type semiconductor material.

When an electron in the CB meets a hole in the VB, the electron occupies the hole since it found a state of lower energy. This recombination process results in the annihilation of an electron in the CB and a hole in the VB. The excess energy of the electron returning from CB to VB in certain semiconductors such as GaAs is emitted as a photon [3]. It is this emission process that is

monitored in this thesis in order to image the transport of free charge in planar semiconductor structures under the influence of applied electric field.

B. DOUBLE-HETEROSTRUCTURE (DH) DEVICE

A junction between two different bandgap semiconductors is called a heterojunction. A semiconductor device structure that has junctions between different bandgap materials is called a heterostructure device [3].

GaAs and AlGaAs are two semiconductors with the characteristics in Table 1.

Semiconductor Active Layer	Structure	Bandgap
GaAs	DH	Direct ($E_g \approx 1.4\text{eV}$)
$\text{Al}_x\text{Ga}_{1-x}\text{As}$ ($0 < x < 0.4$)	DH	Direct ($E_g \approx 2\text{eV}$)
DH=Double Heterostructure		

Table 1. Selected Semiconductor Materials.

Element	Symbol	Z	Electronic Structure
Gallium	Ga	31	$[\text{Ar}]3d^{10}4s^2p^1$
Arsenic	As	33	$[\text{Ar}]3d^{10}4s^2p^3$
Aluminum	Al	13	$[\text{Ne}]3s^2p^1$
Boron	B	5	$[\text{He}]2s^2p^1$
Beryllium	Be	4	$[\text{He}]2s^2$

Table 2. Selected Elements of the Periodic Table.

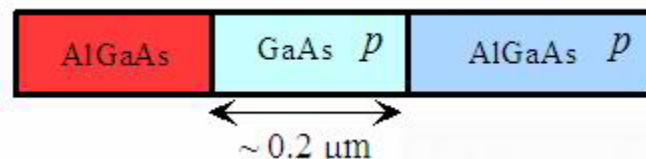


Figure 1. Double-Heterostructure Diode. {After [3]}.

The double heterostructure diode in Figure 1 has an n^+p heterojunction between n^+ -AlGaAs and p - GaAs and another heterojunction between p - GaAs and p - AlGaAs.

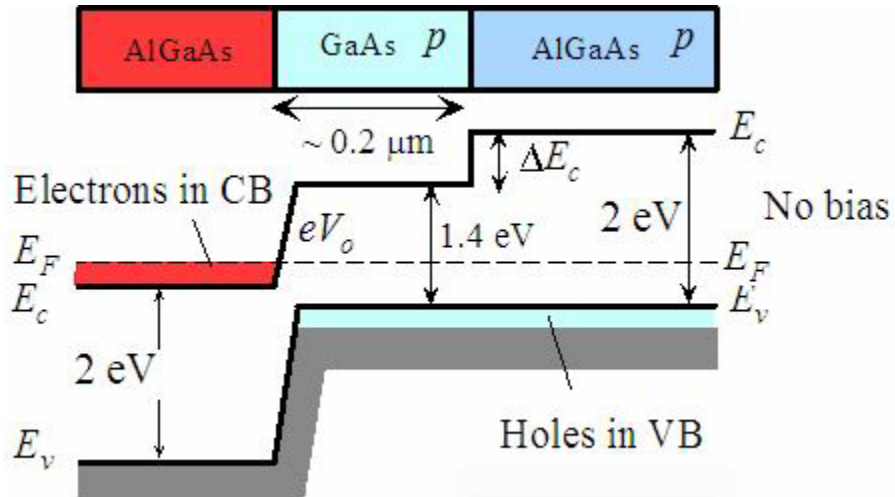


Figure 2. Energy Band Diagram with no bias. {After [3]}.

If no bias is applied in the above double heterostructure, the energy band diagram can be seen in Figure 2. The Fermi energy (E_F) level is uniform. There is a potential energy barrier eV_0 for electrons in the CB of n^+ -AlGaAs against diffusion into p - GaAs. ΔE_c is a potential energy barrier that prevents any electrons in the CB in p - GaAs moving to the CB of p - AlGaAs.

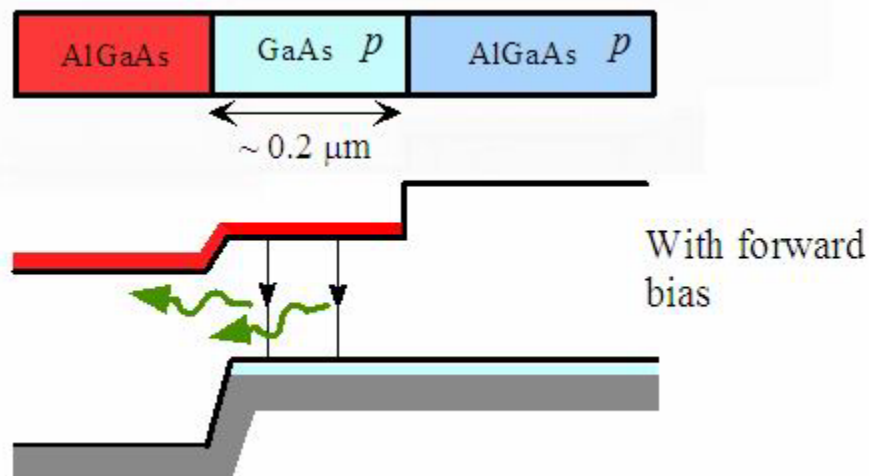


Figure 3. Energy Band Diagram with forward bias. {After [3]}.

When a forward bias is applied, the potential energy barrier eV_0 is reduced and electrons in the CB of n^+ -AlGaAs are injected into p-GaAs as shown in Figure 3. Nevertheless, the energy barrier ΔE_c confine these electrons in the p-GaAs region not allowing them to diffuse to the p-AlGaAs region. The recombination of injected electrons to the holes that already exist in this p-GaAs layer results in spontaneous photon emission.

The example mentioned above is a characteristic example of a double heterostructure (DH) laser diode based on two junctions between different semiconductor materials with different energy bandgaps (n-p-p type material). The reason for describing the principles of operation of this kind of diode is that the experimental approach developed in this thesis is based on a solid source molecular beam epitaxy-grown $\text{Al}_{0.90}\text{Ga}_{0.10}\text{As}/\text{GaAs}/\text{Al}_{0.90}\text{Ga}_{0.10}\text{As}$ double heterostructure sample, so it is important to be able to understand the carrier concentration in the GaAs layer in order to study the transport behavior of free charge.

C. CARRIER TRANSPORT PHENOMENA

When an electric field \vec{E}_x is applied to a semiconductor material, electrons in the CB move opposite to the direction of the electric field, gain energy from the field and lose energy from collisions due to thermal vibrations. This process is called drift of the electrons in an applied field. Similarly, the holes in the VB also drift in an applied field \vec{E}_x but now the drift is in the direction of the electric field. Since both electrons and holes contribute to electrical conduction, current density J is given by:

$$J = env_{de} + epv_{dh} \quad (1)$$

where n is the electron concentration in the CB, p is the hole concentration in the VB, e is the electron charge and v_{de} , v_{dh} are the drift velocities of electrons and holes respectively [3].

The drift velocities of electrons v_{de} and holes v_{dh} in response to an applied electric field \vec{E}_x are given by:

$$v_{de} = \mu_e E_x \quad (2)$$

$$v_{dh} = \mu_h E_x \quad (3)$$

where μ_e and μ_h are the electron and hole drift mobilities [3].

Drift mobility is the constant of proportionality between the drift velocity v_d and the applied electric field \vec{E}_x . The drift mobility μ_e of the electrons and the drift mobility μ_h of the holes are given by:

$$\mu_e = \frac{e\tau_e}{m_e^*} \quad (4)$$

$$\mu_h = \frac{e\tau_h}{m_h^*} \quad (5)$$

where τ_e and τ_h are the mean free times between scattering events and m_e^* and m_h^* are the effective electronic mass and effective mass of a hole respectively [3]. The conductivity of a semiconductor σ is then given by [3]:

$$\sigma = en\mu_e + ep\mu_h \quad (6)$$

The diffusion coefficient is a measure of the ease with which the diffusing charge carriers move in the medium. Diffusion is the random process by which particles move from high concentration regions to low concentration regions. Similarly, drift mobility is a measure of the ease with which the charge carriers move in the medium due to an applied electric field [3]. The above two quantities are related through the Einstein relation:

$$\frac{D_e}{\mu_e} = \frac{kT}{e} \Rightarrow D_e = \mu_e \frac{kT}{e} \quad (7)$$

$$\frac{D_h}{\mu_h} = \frac{kT}{e} \Rightarrow D_h = \mu_h \frac{kT}{e} \quad (8)$$

where D_e and D_h are drift coefficients, μ_e and μ_h are drift mobilities of electrons and holes respectively, k is the Boltzmann constant and T is the

absolute temperature. The $\frac{kT}{e}$ quantity facilitates the use of units of eV for the determination of kT .

It can be seen from equations (7) and (8) that the diffusion coefficient is proportional to the temperature and mobility. This is reasonable since when temperature is increased, diffusion will be enhanced too.

The diffusion coefficient is also affected by the distance l that a free electron (or hole) covers before scattering, in time τ by [3]:

$$D = \frac{l^2}{\tau} \quad (9)$$

Based on equation (9), the diffusion length of holes is given by [3]:

$$L_h = \sqrt{(D_h) \times (\tau_h)} \quad (10)$$

In a p-type semiconductor, holes are the majority carriers and electrons are the minority carriers. Minority carrier concentration in this case is termed as n_{po} where the subscript “po” refers to p-type semiconductor at thermal equilibrium. Thermal equilibrium means that the mass action law is obeyed [3]:

$$n_{po}p_{po} = n_i^2 \quad (11)$$

where n_i is the intrinsic carrier concentration.

It should be mentioned that in equation (10), the term τ_h stands for the minority carrier lifetime which is the average time that a hole exists in the VB from its generation to its recombination with an electron. Recombination time τ_h depends on the semiconductor material, impurities, crystal defects, temperatures and so forth, and there is no typical value to quote (varies from nanoseconds to seconds). In heavily doped semiconductor material $\tau_s \approx \tau_{recom}$. which means that the scattering time is almost identical to the recombination time.

D. LUMINESCENCE PHENOMENA IN SEMICONDUCTORS

Luminescence is the process of photon emission when a solid is supplied with a certain form of energy [4]. Different names are used depending on the source of the excitation. In photoluminescence the excitation is due to absorption of photons. In cathodoluminescence the excitation is being done by absorption of energetic electrons or cathode rays. In chemiluminescence the required energy for the excitation is supplied by chemical reaction. In electroluminescence the excitation is due to the application of an electric field. In semiconductors, luminescence is generally due to the radiative recombination of electron-hole pairs.

The emission of photons in luminescence is due to the electronic transition between the initial energy state E_i and the final energy state E_f . The energy and the wavelength of the emitted photon can be found from the equation:

$$E = E_f - E_i = h\nu = \frac{hc}{\lambda} \quad (12)$$

where ν and λ are the frequency and wavelength of the transmitted photon, h is Planck's constant and c is the speed of light.

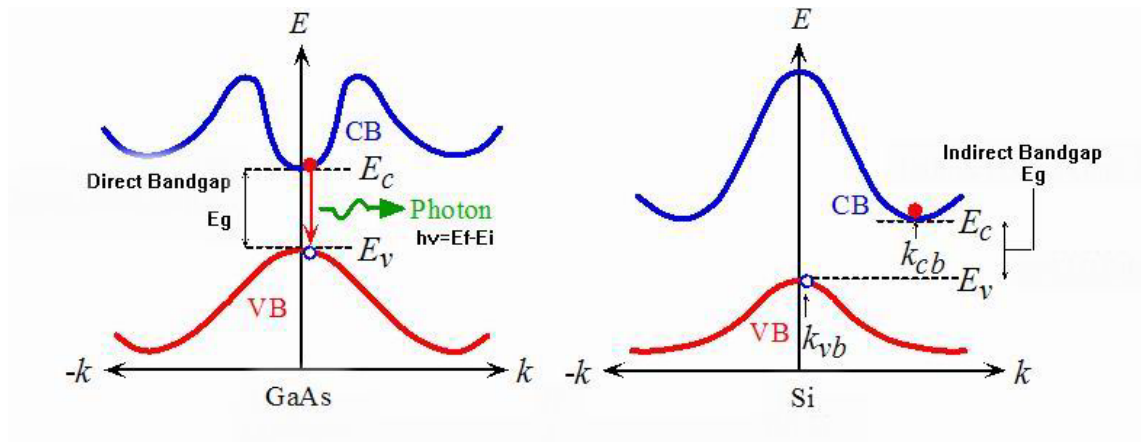


Figure 4. Direct and Indirect Energy Band Diagram. {After [3]}.

In the first case illustrated in Figure 4, GaAs is a direct bandgap semiconductor. During the recombination of electron-hole pair, the electron drops

from the bottom of the CB to the top of the VB without any change in its k value (k is the wave vector) and the momentum is conserved ($\hbar k$) [3]. The result of the recombination is the emission of a photon.

In the second case illustrated in Figure 4, Si is an indirect bandgap semiconductor since the minimum of the CB is not directly above the maximum of the VB. If there is an electron at the bottom of the CB, it cannot recombine directly with a hole at the top of the VB because momentum is not conserved ($k_{cb} \neq k_{vb}$) [3]. In order for an electron to recombine with a hole in such a material, an intermediate recombination center with energy E_r should be used, as shown in Figure 5 below.

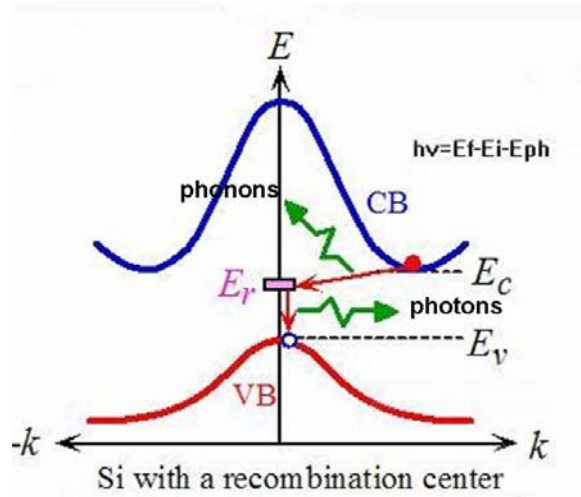


Figure 5. Indirect Energy Band Diagram with Recombination Center. {After [3]}.

In this case, part of the energy of the electron is lost by the emission of phonons that correspond to lattice vibrations. Nevertheless, in some indirect bandgap semiconductors, the recombination process via a recombination center results in photon emission [3]. Such a process has a much lower probability of occurrence than direct transitions and so fundamental emission in indirect-gap semiconductors is relatively weak.

E. CATHODOLUMINESCENCE

Electron beam excitation may produce orders of magnitude greater carrier generation rates than typical optical excitation. The generation factor, which is the number of electron-hole pairs generated per incident electron beam, is given by:

$$G = \frac{E_b(1-\gamma)}{E_i} \quad (13)$$

where E_b is the electron beam energy, E_i is the ionization energy (the energy required for the formation of the electron-hole pair) and γ is the fractional electron beam energy loss due to the backscattered electrons [4].

The ionization energy E_i is related with the band gap of the material by:

$$E_i = 2.8E_g + M \quad (14)$$

In equation (14), $0 < M < 1$ eV. M depends on the material and is independent of the electron beam energy [4].

The local generation rate of carriers is:

$$g(r, z) = \langle g \rangle \frac{GI_b}{e} \quad (15)$$

where $\langle g \rangle$ is the normalized distribution of the ionization energy in the generation volume, I_b is the electron beam current and e is the electronic charge [4].

The local generation rate of carriers has been determined experimentally for silicon and a universal depth-dose function $g(z)$ is given by:

$$g(z) = 0.60 + 1.21z - 12.40z^2 + 5.69z^3 \quad (16)$$

Equation (16) represents the number of electron-hole pairs generated per electron of energy E per unit depth per unit time. Graphically it can be represented as shown in Figure 6 [4]. GaAs will show a similar behavior for varying values of incident beam energy.

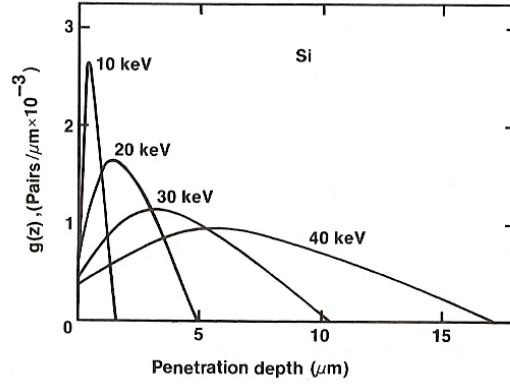


Figure 6. The depth-dose curves for Si. {From [5]}.

F. CATHODOLUMINESCENCE INTENSITY

The CL intensity represents the number of photons emitted per unit time and is given by [4]:

$$L_{CL}(r) = \int_V f \frac{\Delta n(r)}{\tau_{rr}} d^3r \quad (17)$$

where τ_{rr} is the radiative recombination lifetime, $\frac{\Delta n(r)}{\tau_{rr}}$ is the radiative recombination rate, $\Delta n(r)$ is the excess minority carrier density and f is a function containing correction parameters of the CL detection system and factors that account for the fact that not all photons generated in the material are emitted (due to optical absorption and reflection losses) [4].

For a spherically symmetric distribution far from the point source:

$$\Delta n(r) = C \frac{e^{-\frac{r}{L}}}{r} \quad (18)$$

where C is a constant and $L = \sqrt{D\tau}$ is the minority carrier diffusion length [4]. It should be noted that equation (18) refers to diffusion in three dimensions. In this thesis where the sample is a thin layer and a 2D distribution from the point source is used, equation (18) becomes:

$$\Delta n(r) = CK_0 \left(\frac{r}{L} \right) \quad (19)$$

where K_0 is the zeroth order modified Bessel function of the second kind (the 2D case is described in Chapter III of the current thesis).

The luminescence intensity due to the radiative recombination in a layer of thickness dz at a depth z is:

$$L_{CL}(z)dz \propto \frac{\Delta n(r)}{\tau_r} \propto \frac{GI_b L e^{-\frac{z}{L}} dz}{e\tau_r D} \quad (20)$$

More specifically the intensity is given by:

$$L_{CL} = f_D f_A f_R \frac{GI_b \tau}{e\tau_r} \quad (21)$$

where f_D is a constant that accounts for parameters of the CL detection system such as the overall collection efficiency of the light collector, f_A and f_R are factors that account for absorption and internal reflection losses [4].

An understanding of the cathodoluminescent intensity is crucial because the work presented in this thesis is based on the direct transport imaging of free charge carriers by simultaneously evaluating the luminescent intensity due to radiative recombination in a point source. The values of the intensity that can be acquired by using an appropriate 2D mathematical model for DC and AC electric fields will be used in order to be able to determine the values of the electric field locally in planar semiconductor material.

THIS PAGE INTENTIONALLY LEFT BLANK

III. EXPERIMENTAL APPROACH

A. DIRECT TRANSPORT IMAGING

It is very important to be able to directly image the injection and the motion of free charge in planar semiconductor structures, with high resolution. By doing this, much more can be learned than from macroscopic current-voltage measurements that are based on the average of local transport behavior. The small size of current semiconductor devices used in industry, the structure complexity, the role of the material non-uniformity, the effects of various defects and the necessity of a non-destructive approach are some of the reasons that make the direct transport imaging technique an efficient way to study the electric behavior of semiconductor devices, particularly sensors and detectors that depend on the collection of photo-generated charge.

The direct transport imaging technique described in this thesis is based on the capability to image the motion of free carriers in planar semiconductor structures under a range of applied electric fields via the luminescence emission. This is illustrated in Figure 7 below.

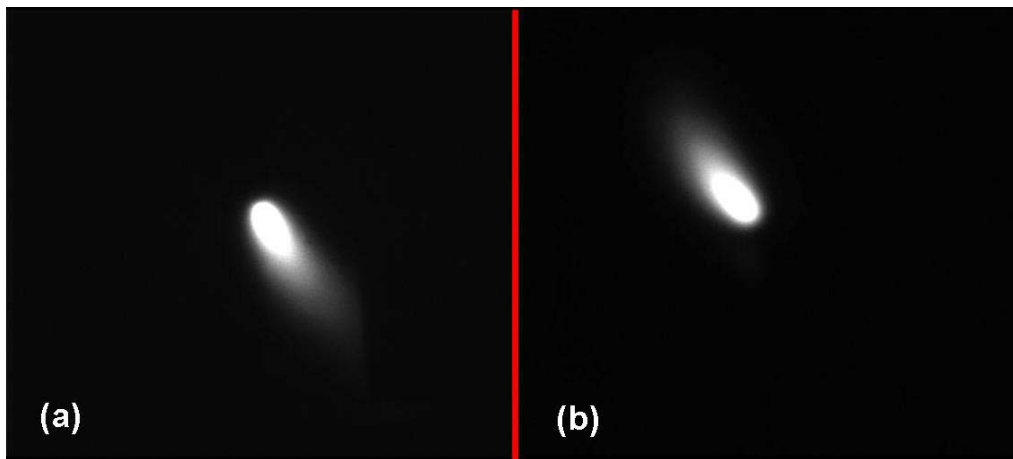


Figure 7. Spot mode imaging in a p-type AlGaAs/GaAs/AlGaAs heterostructure in two different cases of applied electric field [(a) and (b) 216 μm X 190 μm].

As in CL, the recombination of electron – hole pairs created by the interaction of the electron beam with the planar structure results in photon emission. The difference with the conventional CL technique is that the electron beam is held fixed over a predefined location [2]. By doing this, the generation point (of e-h pairs) is held fixed too. The largest fraction of the photon signal due to the recombination is created at or near the point of charge generation. However there is a small fraction of the photon signal that is created due to carrier diffusion or drift. If conventional CL is used, the actual distribution of luminescence is lost [2]. In direct transport imaging, the light created by the recombination retains the spatial information of its origin. By maintaining the actual distribution of the luminescence, the motion of the minority charge due to carrier diffusion or drift can be observed.

B. SCANNING ELECTRON MICROSCOPE (SEM)

1. SEM Components

The two major components of an SEM are the electron column and the control console (Figures 8, 9). The electron column consists of the electron gun and various lenses that control the beam path. The electron beam motion occurs in an evacuated tube whose base pressure is maintained at $\sim 10^{-4} - 10^{-5}$ Pa [6].



Figure 8. Electron Column.

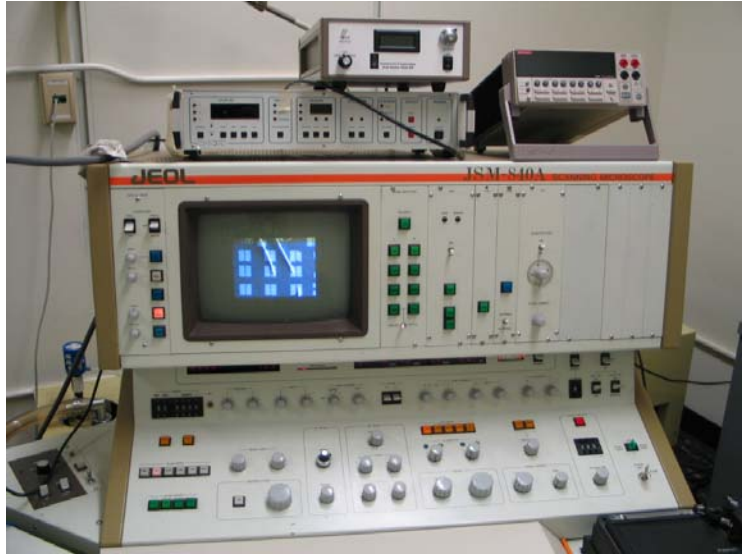


Figure 9. Control Console.

The electron gun produces an electron beam by thermionic emission after heating a tungsten filament to a temperature of about 2000-2700 K. It accelerates electrons in the range 0.1-40 keV. Spot size at the specimen is less than 10 nm at the lowest probe current and penetration depth is ~ about 1-10 μm depending on the material and the energy of the incident beam. The deflection system controls the magnification. The magnification M of the image is the ratio of the length of the raster on the viewing screen to the corresponding length of the raster on the specimen L (Figure 10). So magnification 1000X corresponds to a 100 μm -wide raster on the specimen displayed on a 10 cm-wide viewing screen [6].

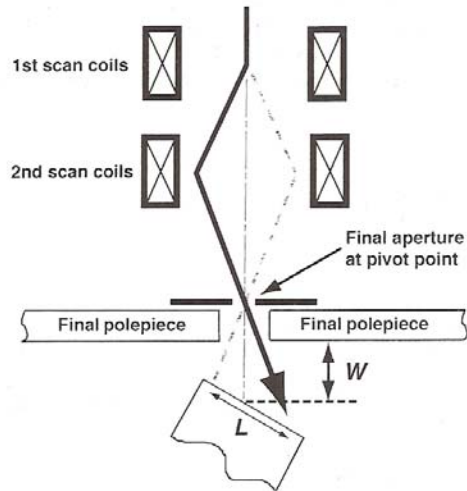


Figure 10. Deflection system inside the SEM. {From [6]}.

2. SEM Basic Parameters

The electron probe size d_p is the diameter of the final beam at the surface of the specimen. The electron probe current i_p is the current that impinges upon the specimen and generates the various imaging signals. The electron probe convergence angle α_p is the half-angle of the cone of electrons converging onto the specimen. Finally the accelerating voltage (V_o) of the electron beam defines the electron beam's energy [6]. All these parameters are illustrated in Figure 11.

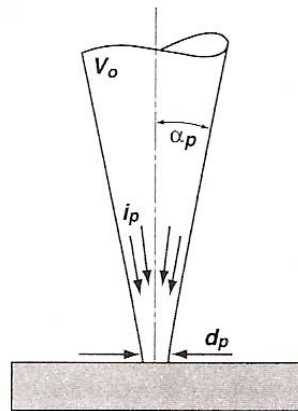


Figure 11. Major electron beam parameters. {From [6]}.

3. Electron Beam-Specimen Interactions

If a 20 kV accelerating potential is used, electrons travel with energy equal to 20 keV with a deviation of 0.5 eV. Due to the fact that the SEM column is

under vacuum (10^{-5} Pa), there are very few gas molecules that can collide with electrons and deflect them out of the beam. So almost all the electrons created will strike the surface of the specimen in a circle of minimum diameter of ≈ 1 nm.

As the beam electrons enter the specimen, they interact as negatively charged particles with the specimen atoms and their corresponding electrical fields. The initial interaction of the electron beam with the atoms of the specimen results in an elastic scattering of the electrons with no kinetic energy loss. Electrons, due to this elastic scattering, spread out from the incident beam footprint. After numerous elastic scattering events, a portion of electrons finally leave the specimen by a process called “backscattering.” Simultaneously with elastic scattering, beam electrons gradually lose energy, transfer their energy to specimen atoms (inelastic scattering) and secondary electrons are created. Backscatter and secondary electrons are the basis of the SEM imaging process. Additionally, the initial probe diameter of 1 nm has no relevance to the image resolution. In fact, a 20 keV, 1 nm diameter initial probe, has 103 times greater linear dimensions on the entrance surface and 109 times greater volume dimensions than the atomic layer under the beam footprint [6].

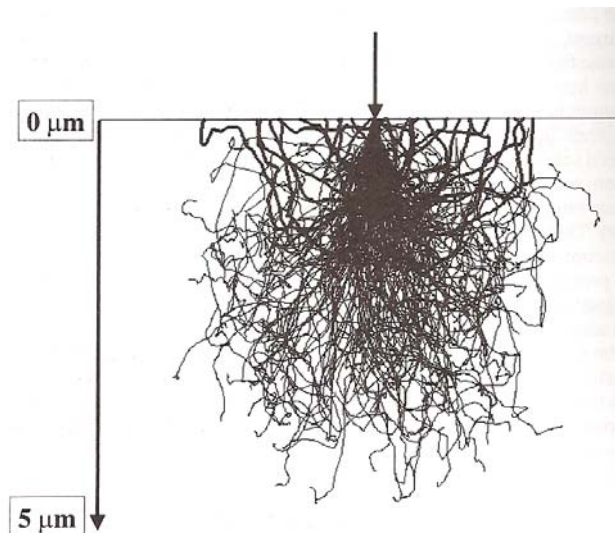


Figure 12. Interaction Volume for a 20 keV beam striking Si. {From [7]}.

In Figure 12, the electron trajectories have been evaluated with the Monte-Carlo simulation method. The beam electron trajectories that emerge as backscattered electrons are shown as thick traces.

All the above can be expressed mathematically with the following equations [6]:

$$Q(> \varphi_0) = 1.62 \times 10^{-20} \times \left(\frac{Z^2}{E^2} \right) \times \cot^2 \left(\frac{\varphi_0}{2} \right) \quad (22)$$

$$\frac{dE}{ds} \left(\frac{keV}{cm} \right) = -7.85 \times 10^{-4} \frac{Z\rho}{AE_i} \ln \left(\frac{1.166E_i}{J} \right) \quad (23)$$

In equation (22) Q is the probability of elastic scattering for angles greater than the specified angle φ_0 , Z is the atomic number of the specimen's material and E is the electron energy. In equation (23) $\frac{dE}{ds}$ is the rate of energy loss dE with distance traveled ds , ρ is the density of the material in $\frac{g}{cm^3}$, E_i is the electron energy at any point in the specimen in (keV), A is the atomic weight in $\frac{g}{mole}$ and J is the average loss in energy per event. The negative sign represents energy loss.

As the beam energy increases, from equation (22) it can be seen that the electrons penetrate more deeply into the specimen since the probability of elastic scattering is decreased. From equation (23) it can be seen also that as energy increases, the penetration depth will be larger since electrons enter the specimen with more energy and the rate of energy loss is smaller.

In order to avoid the complexity of the 3-dimensional interaction volume, the latter can be estimated by only one parameter which is electron range and it is given by (due to Kanaya and Okayama) [8]:

$$R_{KO}(\mu m) = \frac{0.0276A}{Z^{0.89} \rho} E_0^{1.67} \quad (24)$$

where A is the atomic weight in $\frac{g}{mole}$, Z is the atomic number of the specimen's material, ρ is the density of the material in $\frac{g}{cm^3}$, E_0 is the beam energy in keV and R_{KO} is the electron range in μm . In this thesis the basic semiconductor material used is GaAs, so by using equation (24) for evaluating the electron range for a GaAs sample under the influence of a beam with energy $E_0 = 30 keV$:

$$R_{KO}(\mu m) = \frac{0.0276A}{Z^{0.89}\rho} E_0^{1.67} = \frac{0.0276 \times (69.72 + 74.92) \frac{g}{mole}}{32^{0.89} \times 5.32 \frac{g}{cm^3}} \times (30 keV)^{1.67} = 10 \mu m \quad (25)$$

The result of equation (25) is valid if it is assumed that the specimen is flat, thick enough to be electron-opaque and of sufficiently large lateral extent that there are no edges or boundaries within R_{KO} of the beam, and the incident electron beam is placed normal to the specimen surface. Due to various uncertainties of the method, the result should not be stated beyond two significant figures [6].

4. SEM Imaging Process

The information flow from the SEM consists of the scan location in x-y space and a corresponding set of intensities from the set of detectors (backscattered electron, secondary electron, transmitted electron, specimen current, cathodoluminescence) that monitor the beam-specimen interactions simultaneously. In this thesis, secondary electron and CL signals are collected simultaneously.

a. Picture Mode

In picture mode, the electron beam is scanned on the specimen and the resulting luminescence pattern is recorded by the Charge Coupled Device (CCD) camera. An example of a picture of a specimen which is going to be described later in this thesis (AlGaAs/GaAs/AlGaAs heterostructure), taken by this mode of SEM operation, is shown in Figure 13.



Figure 13. Picture Mode image with application of 15V AC in a p-type AlGaAs/GaAs/AlGaAs heterostructure (874 μm X 589 μm).

In Figure 13, it is interesting to observe the change in the direction of the electron drift which is towards the plate when the applied electric field is positive (+15V) and outwards in the opposite case [negative electric field, (-15V)].

b. Line Mode

In the line scan mode, the beam is scanned along a single vector on the specimen. With this method, dynamic electric fields can be visualized better when applied to relatively large areas. An example of an image taken with line scan mode is shown in Figure 14. In Figure 14, the direction of the electron drift indicates that the plate (shown in red color for identification purposes only) is positively charged. Also it should be noted that the larger spot in the left side of the line scan is due to the fact that the SEM always holds the beam longer at one edge of the scanning area.

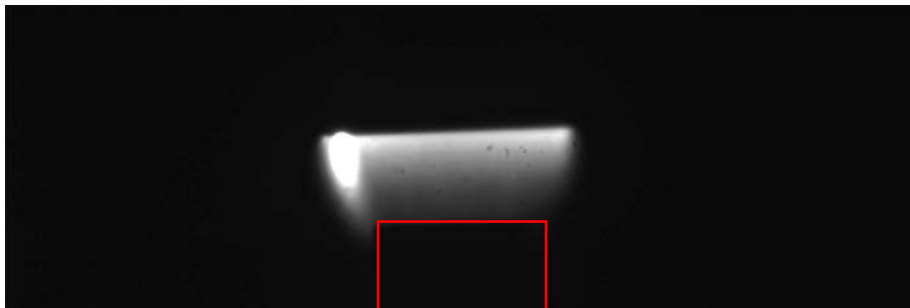


Figure 14. Line Scan Mode image with application of 15V DC in a p-type AlGaAs/GaAs/AlGaAs heterostructure (872 μm X 293 μm).

c. Spot Mode

The majority of the SEM imaging, in order to make measurements of local minority charge carrier transport, has been done with the spot mode of operation. In this mode, the electron beam is held fixed over a specific point of the specimen. An example of this mode is shown in Figure 15.



Figure 15. Spot Mode image with application of 15V DC in a specific point of a p-type AlGaAs/GaAs/AlGaAs heterostructure (216 μm X 190 μm).

The spot shown in Figure 15 is the luminescence created by the recombination of e-h pairs in response to the interaction of the electron beam with the specimen. Explanation of the shape of the drift tail will be done in the next chapter. All the light collected retains the spatial information of its point of origin. The optical image is acquired from the CCD camera using “MicroCCD - Version 3.13 - Diffraction Limited – 1999”, an image analysis software package. One effective way to study the material’s minority carrier properties is to extract each “TIFF” image created in MicroCCD to a MATLAB file and analyze the results of the intensity of luminescence with a method explained later in this thesis.

5. Laboratory’s SEM

In the current work, the SEM used is a JEOL 840A SEM with electron energy range up to 40 keV. In order to observe luminescence for sample temperatures from 5-300 K there is a liquid helium-cooled SEM stage (Oxford Instruments). The optical detector is a thermoelectrically cooled Si CCD camera

with a resolution of 0.4 $\mu\text{m}/\text{pixel}$. The equipment is shown in Figure 16 and an overall schematic representation of the system is given in Figure 17.

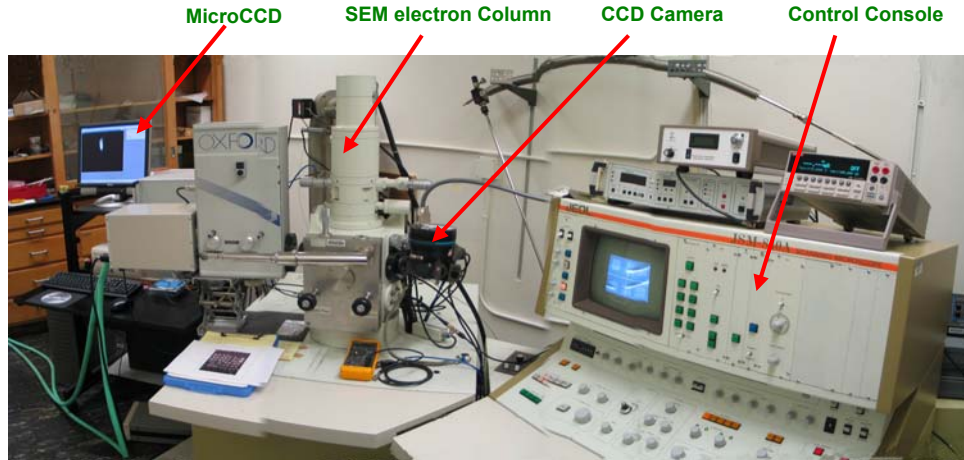


Figure 16. JEOL 840A SEM.

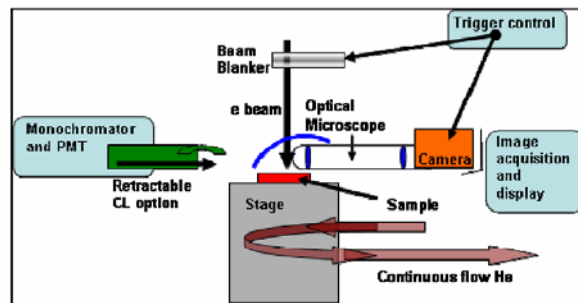


Figure 17. SEM Overall Schematic Operation and Components {From [9]}.

C. AlGaAs/GaAs/AlGaAs HETEROSTRUCTURE SAMPLE

Figure 18 shows the solid source molecular beam epitaxy (MBE)-grown $\text{Al}_{0.90}\text{Ga}_{0.10}\text{As}/\text{GaAs}/\text{Al}_{0.90}\text{Ga}_{0.10}\text{As}$ double heterostructure, which will be referred to as “Sample #9” (designed by Dr. Thomas Boone, Hitachi Global Storage).

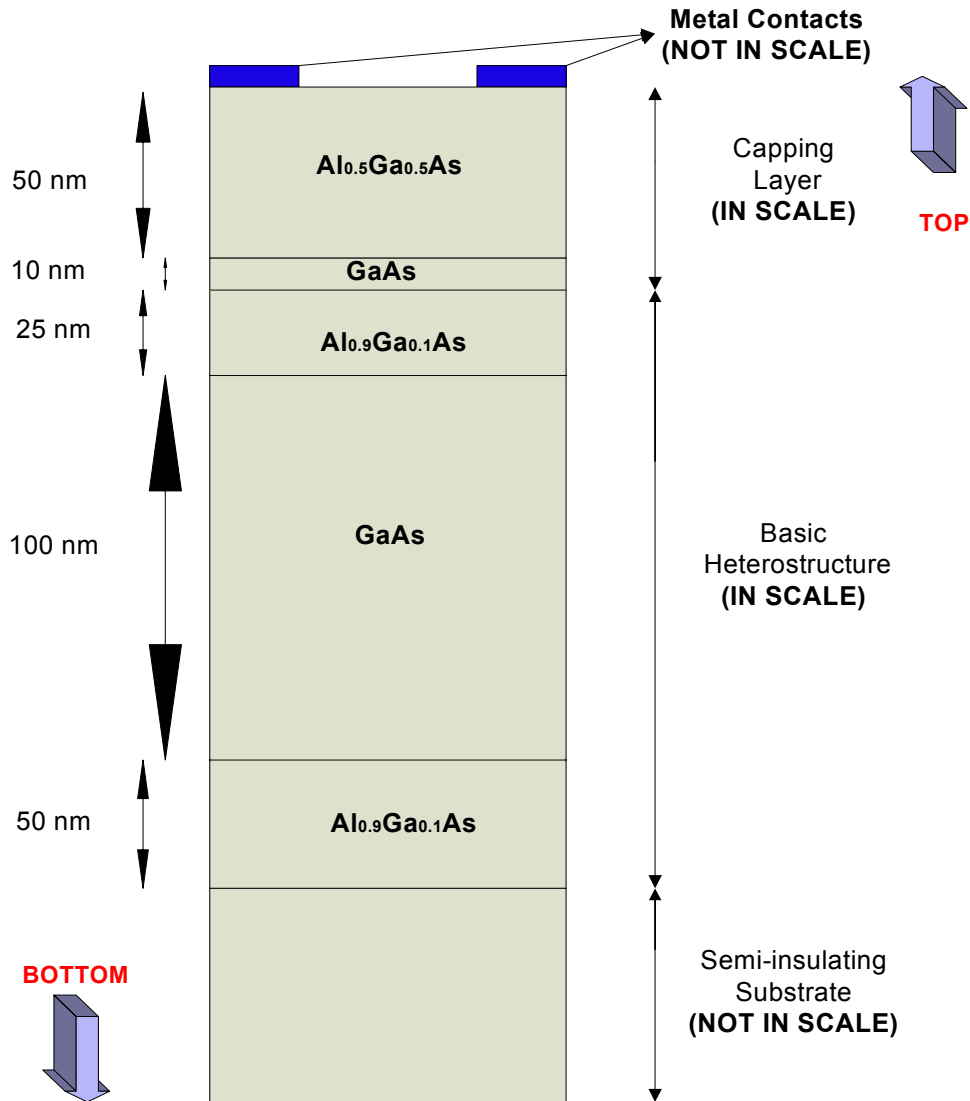


Figure 18. AlGaAs/GaAs/AlGaAs heterostructure sample.

The top and bottom barrier layers of Al_{0.90}Ga_{0.10}As were incorporated to reduce surface recombination effects and confine the photogenerated electrons within the p-type GaAs layer. The AlGaAs layers were heavily doped with Be (Beryllium) to $N_A = 2 \times 10^{19} \text{ cm}^{-3}$ (acceptors/cm³), with a resulted p-doping of the GaAs layer to the mid $1 \times 10^{18} \text{ cm}^{-3}$. This is known as a modulation doped structure, where the dopant atoms are in the AlGaAs layers while the free holes are in the GaAs, unaffected by impurity scattering. A capping layer has been incorporated on top of the structure in order to reduce surface oxidization.

Additionally, Van der Pauw mesa structures were etched into the wafer and Ti:Au nonalloyed electrical contacts were deposited and lithographically defined on top of the mesas [10].

The minority carrier lifetime of the active layer was measured with time resolved photoluminescence to be 870 ps. A technique for imaging the photoluminescent (PL) emission from the surface of the semiconductor under increasing applied voltage was used by Dr. Thomas Boone et.al [10]. The PL displacement noticed was due to electron drift prior to recombination of electron-hole pairs. This displacement should be (on average) equal to the distance that the electrons drift from their generation position in their recombination lifetime τ . Based on the above this distance is given by:

$$d = v_{de}\tau \Rightarrow d = (\mu_e E)\tau \quad (26)$$

where d is the distance traveled by electron while drifting from its generation point, v_{de} is electron drift velocity, τ is the recombination lifetime, μ_e is electron drift mobility and E is the electric field intensity. Additionally, for the above described p-type epitaxial structure, the values used in equation (26) for determining the distance of electron drift were $\tau \approx 870 * 10^{-12} s$, $\mu_e \approx 2000 \frac{cm^2}{Vs}$ and

$E_{max} = 2000 \frac{V}{cm}$ (E_{max} is the maximum value of the electric field intensity used during the technique of imaging the PL emission described above). Solving (26) with these values, the resulted distance is $d = 35 \mu m$ [10].

In Figure 19, a part of Sample #9 (top view), can be seen. The red arrows represent the places where wiring of the sample has been done.

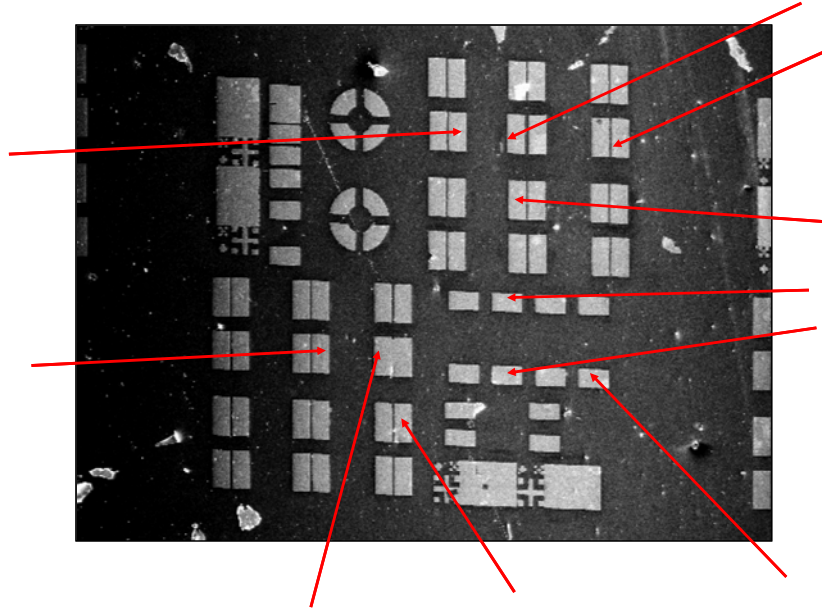


Figure 19. Part of Sample #9 Structure (3482 μm X 2611 μm).

D. SIMULATIONS

1. DC Modeling

Fundamental transport behavior can be determined by imaging the charge motion as a function of applied electric field. Transport behavior can be predicted by modeling the drift and diffusion in two dimensions with respect to generation at a point source. If an electric field E is applied in the x direction, the differential equation that represents the corresponding intensity in the x and y directions is [2]:

$$S\varpi_x - L^2\varpi_{xx} - L^2\varpi_{yy} = G\tau - \varpi \quad (27)$$

where: S = drift length, $S = \mu\tau E$,

L = diffusion length, $L = \sqrt{D\tau}$,

ϖ_x, ϖ_{xx} = the first and second derivative in x of the carrier distribution ϖ ,

ϖ_{yy} = the second derivative in y of the carrier distribution ϖ ,

G = generation rate of electron-hole pairs [$\#/(cm^3 s)$],

τ = minority carrier (electron) lifetime.

The solution to the differential equation (27), for a Gaussian distribution $e^{-n(\xi^2+\eta^2)}$ of the original beam, is:

$$Intensity = \frac{gn}{2\pi^2 L^2} \int_{-\infty}^{\infty} \int_{-\infty}^{\infty} K_0 \left[\frac{\sqrt{S^2 + 4L^2}}{2L^2} \sqrt{(x-\xi)^2 + (y-\eta)^2} \right] e^{-n(\xi^2+\eta^2)} e^{\frac{S(x-\xi)}{2L^2}} d\xi d\eta \quad (28)$$

In equation (28): K_0 = zeroth order modified Bessel function of the second kind,

n = parameter that defines the spread of the generation region.

By simulating the diffusion/ drift behavior for the values shown in Table 3 below, the corresponding graph of Figure 20 represents the 2D view through the distribution in x and y directions. The color scale in Figure 20 represents the difference in intensity values derived from equation (28). The direction of the diffusion-drift is due to the application of an electric field in the x-direction of 209.50E-4 V/ μm . Figure 20 illustrates what is expected to be seen in an SEM image due to the application of a DC bias.

g (#/cm ³ s)	L (μm)	x (range in μm)	y (range in μm)	n	kT (eV)
1	3.4	-30:0.5:30	-30:0.5:30	0.4	0.025
E (V/ μm)	$\mu\tau$ ($\mu\text{m}^2/\text{V}$)	S (μm)			
209.50E-4	$\mu\tau=eL^2/kT$	$S=\mu\tau E$			

Table 3. Parameters for the evaluation of DC model for the simulation of diffusion/ drift behavior in x and y direction.

Intensity Distribution in x, y Direction

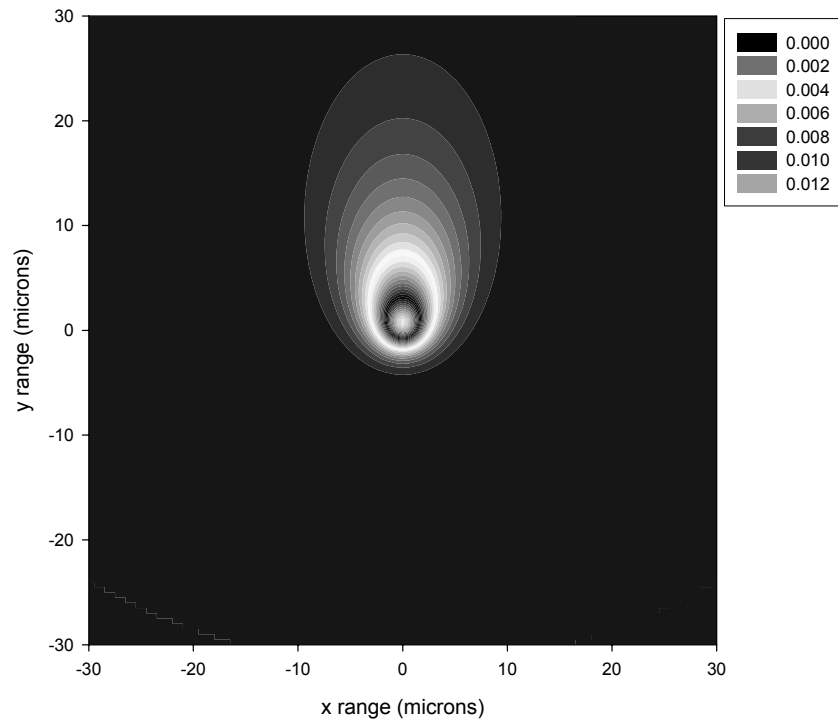


Figure 20. Intensity distribution in x, y direction based on simulation for DC applied field.

By simulating again the diffusion/ drift behavior but now for various values of applied electric field E and specifically for $E=(0, 30*10^{-4}, 44*10^{-4}, 70*10^{-4}, 100*10^{-4}, 131.50*10^{-4}, 170*10^{-4}, 209.50*10^{-4}, 250*10^{-4}, 313.50*10^{-4}, 370*10^{-4}, 412*10^{-4}, 450*10^{-4}, 521*10^{-4}, 560*10^{-4}, 600*10^{-4})$ V/ μ m, the corresponding graph is shown in Figure 21 below. Additionally, the other parameters needed for the evaluation of (29) were defined as shown in Table 4.

g (#/cm ³ s)	L (μm)	x (range in μm)	y (range in μm)	n	kT (eV)
1	3.4	-30:0.5:30	0	0.4	0.025
E (V/μm)	μτ (μm ² /V)	S (μm)			
values mentioned above	$\mu\tau=eL^2/kT$	$S=\mu\tau E$			

Table 4. Parameters for the evaluation of DC model for the simulation of diffusion/ drift behavior.

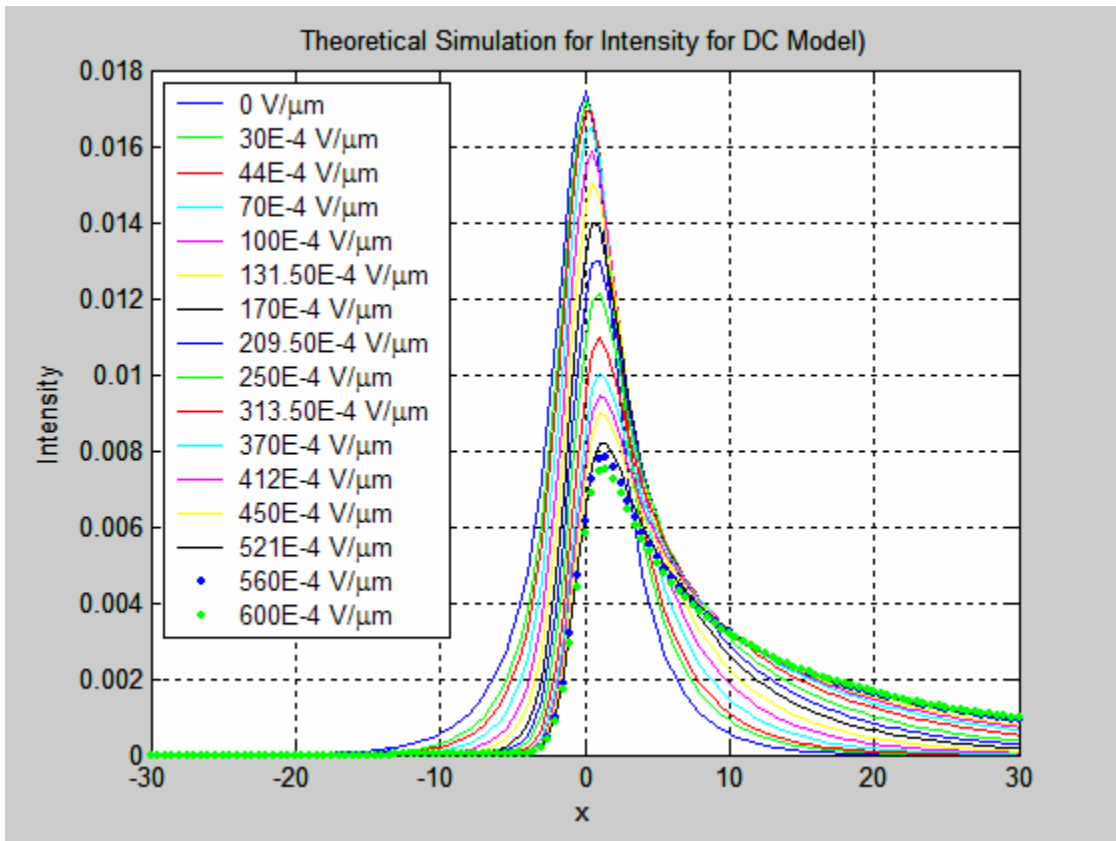


Figure 21. Simulation for varying values of DC applied field.

The results shown in Figure 21 reflect the increasing drift length and transport of charge with increasing electric field. It can be seen also that, as the applied voltage increases, the peak intensity of each curve decreases and shifts to the right (with respect to the central value $x=0$). All the areas under the curves

are equal. This can be shown by use of the trapezoid rule for evaluating the area under each curve (numerical analysis). If the above model is simulated for a much greater number of electric field values and the value of peak intensity is defined for each case (different applied voltage), a plot of normalized intensity (with respect to $E=0$ V/ μm) versus applied electric field can be created (Figure 22). In Figure 23, a regression analysis has been made, in order to define the curve fitting parameters of the line connecting the normalized peak intensity values with respect to applied electric field. It should be noted that the axes in Figure 23 have been inverted only for simplifying the fitting parameter procedure. The MATLAB code used for the generation of the current graphs can be found in Appendix A.

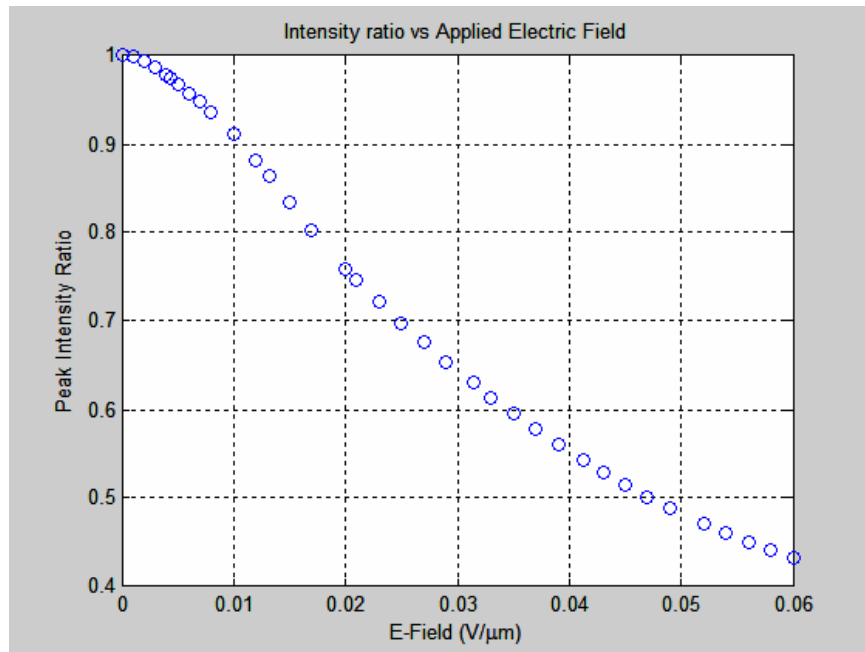


Figure 22. Intensity ratio vs. applied electric field based on simulation for DC applied field.

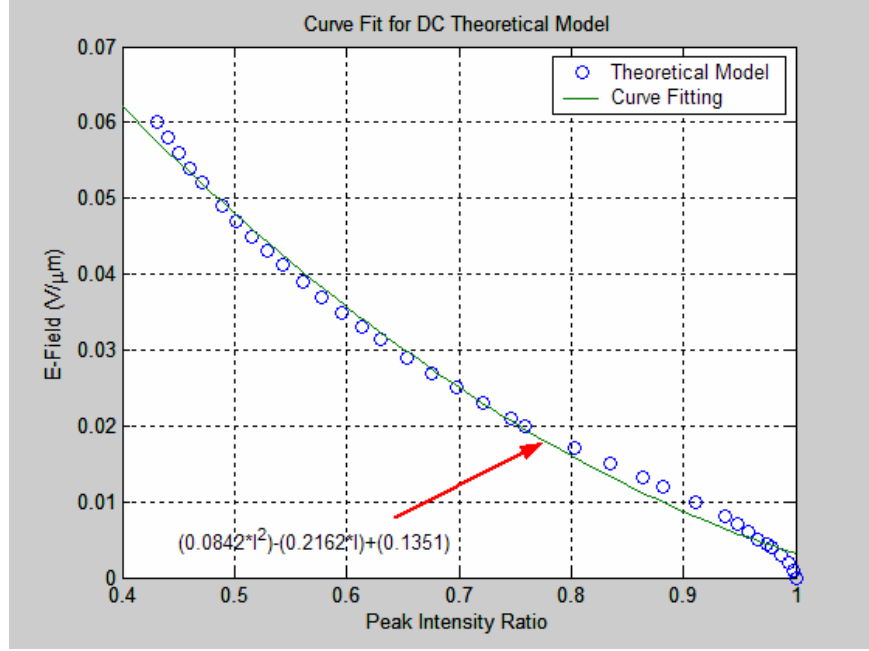


Figure 23. Curve fitting for DC field simulation.

2. AC Modeling

Similar to the previous technique of obtaining the DC field behavior, an analogous method for the AC field has been developed. The model for the AC field is the following:

$$Intensity = \int_0^5 \frac{gn}{2\pi^2 L^2} \int_{-\infty}^{\infty} \int_{-\infty}^{\infty} K_0 \left[\frac{\sqrt{S(t)^2 + 4L^2}}{2L^2} \sqrt{(x-\xi)^2 + (y-\eta)^2} \right] e^{-n(\xi^2 + \eta^2)} e^{\frac{S(t)(x-\xi)}{2L^2}} d\xi d\eta dt$$

where: S = drift length, $S(t) = \mu\tau E(t)$, (29)

L = diffusion length, $L = \sqrt{D\tau}$,

G = generation rate of electron-hole pairs [#/(cm³ s)],

τ = minority carrier (electron) lifetime,

$E(t) = A\sin(\omega t)$ = sinusoidal AC electric field,

$\omega = 2\pi f$ where f is the frequency used for the AC current. The rest of parameters are the same as for equation (28).

By simulating the diffusion/ drift behavior for the values shown in Table 5 below, the corresponding graph of Figure 24 represents the 2D view of the distribution in x and y directions for the case of AC bias (for t=2s). The color scale in Figure 24 represents the difference in intensity values derived from equation (29). The distribution is symmetric due to the application of AC bias.

g (#/cm ³ s)	L (μm)	x (range in μm)	y (range in μm)	n	kT (eV)
1	3.5	-50:1.0:50	-50:1.0:50	0.5	0.025
E(t) (V/μm)	A (V/μm)	μτ (μm ² /V)	S(t) (μm)	f (Hz)	ω (rad/s)
E(t)=Asin(ωt)	209.50E-4	μτ=eL ² /kT	S(t)=μτE	333	ω=2πf

Table 5. Parameters for the evaluation of AC model for the simulation of diffusion/ drift behavior in x and y direction.

Intensity Distribution in x,y Direction

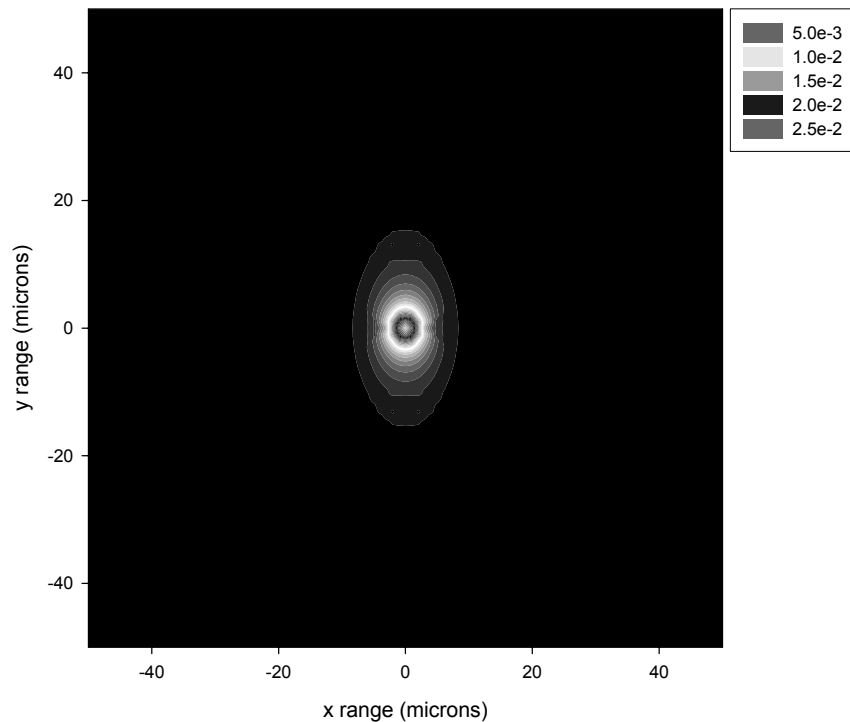


Figure 24. Intensity distribution in x, y direction based on simulation for AC applied field.

By simulating the diffusion/ drift behavior for various values of applied electric field E and specifically for amplitude of electric field (peak-to-peak), $A=(0, 44*10^{-4}, 131.50*10^{-4}, 209.50*10^{-4}, 300*10^{-4}, 412*10^{-4})$ V/ μm , the corresponding graph is shown in Figure 25. Additionally, the other parameters needed for the evaluation of (30) were defined as shown in Table 6.

g (#/cm ³ s)	L (μm)	x (range in μm)	y (range in μm)	n	kT (eV)
1	3.5	-50:1.0:50	0	0.5	0.025
E(t) (V/ μm)	A (V/ μm)	$\mu\tau$ ($\mu\text{m}^2/\text{eV}$)	S(t) (μm)	f (Hz)	ω (rad/s)
$E(t)=A\sin(\omega t)$	as above	$\mu\tau=eL^2/kT$	$S(t)=\mu\tau E$	333	$\omega=2\pi f$

Table 6. Parameters for the evaluation of AC model for the simulation of diffusion/ drift behavior.

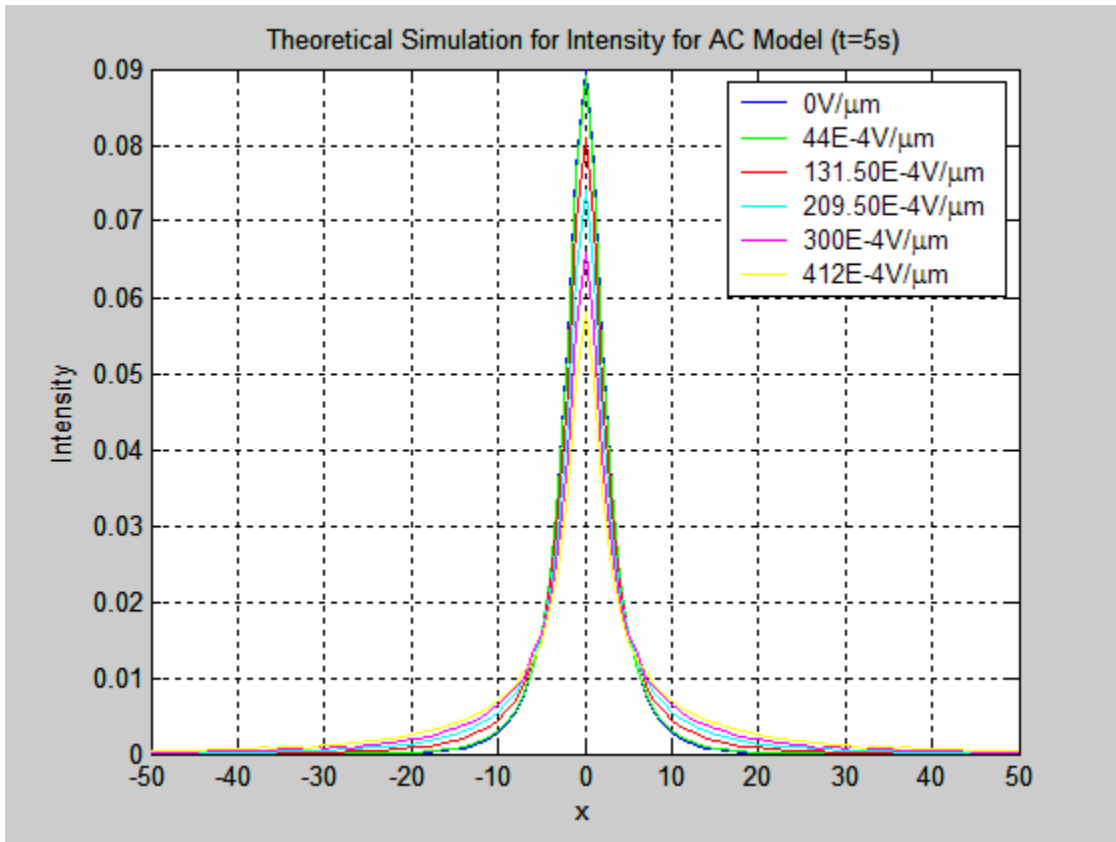


Figure 25. Simulation for varying values of AC applied field.

The results shown in Figure 25 reflect the increasing drift length and transport of charge with increasing electric field. The value of the peak intensity of each curve is directly dependent on time (by increasing the time the value of the intensity increases too) but by evaluating the ratio I/I_0 , the results (normalized intensity ratios) are independent of time. This can be seen clearly in Figure 26 where a comparison of normalized intensity ratios with respect to different times (2 sec and 5 sec) has been performed. In Figure 25, it can also be seen that, as the applied voltage increases, the peak intensity of each curve decreases but remains as expected, in the center of the graph (with respect to the central value $x=0$). All the areas under the curves are equal. This can be shown again by use of the trapezoid rule for evaluating the area under each curve (numerical analysis). If the values of peak intensity are defined for each case (different applied voltage), a plot of normalized intensity (with respect to $E=0 \text{ V}/\mu\text{m}$) versus applied electric field is shown in Figure 27 below. Also in Figure 28, a regression analysis has been made, in order to define the curve fitting parameters of the line connecting the normalized peak intensity values with respect to applied electric field. Note that the axes in Figure 28 have been inverted only for simplifying the fitting parameter procedure.

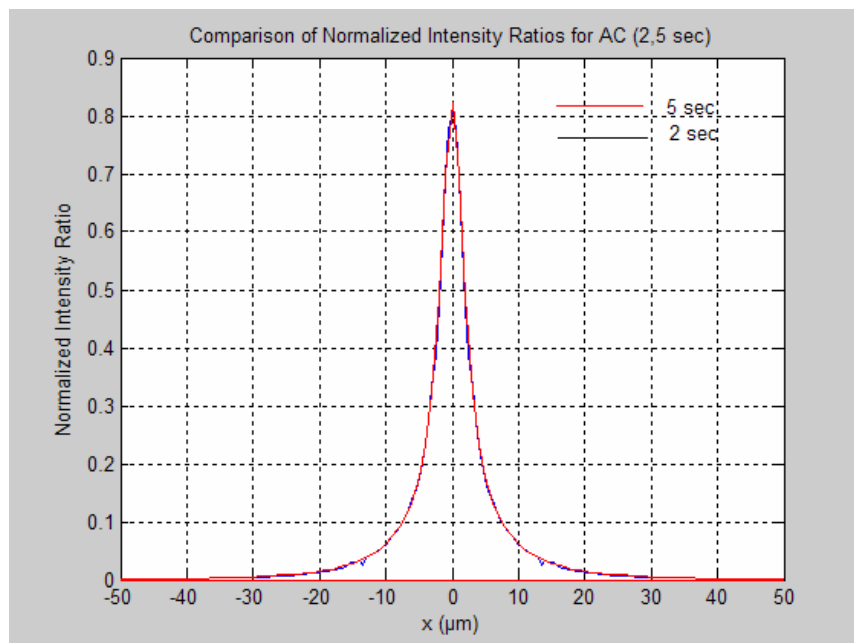


Figure 26. Comparison of normalized intensity ratios for different times.

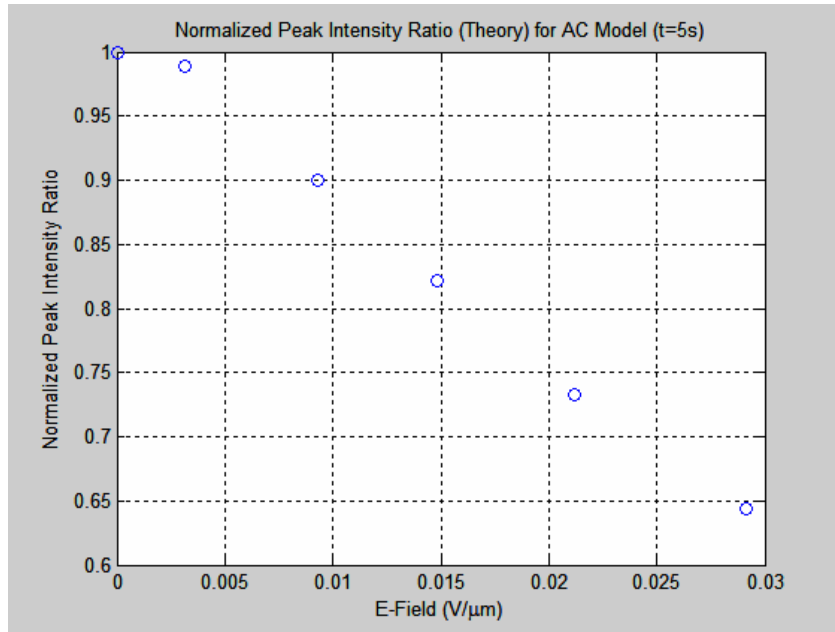


Figure 27. Intensity ratio vs. applied electric field based on simulation for AC applied field.

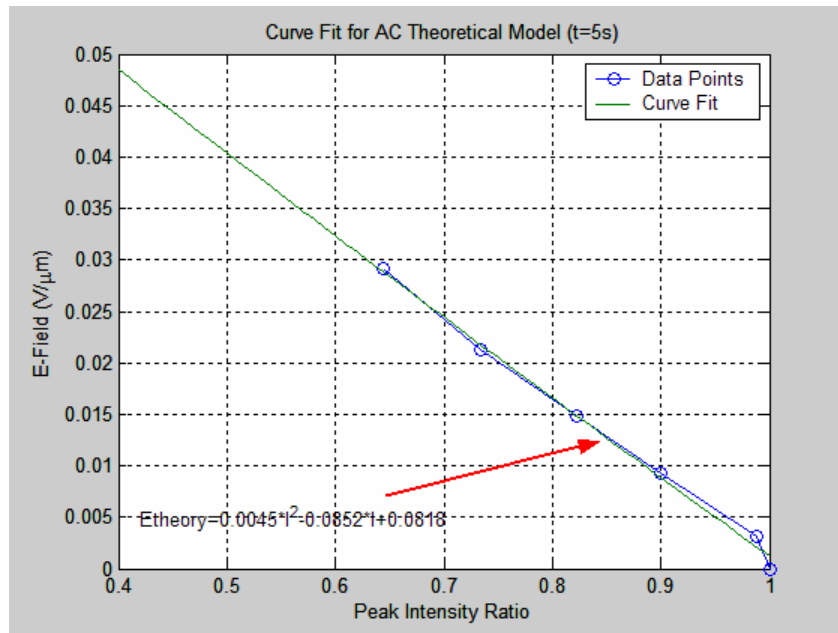


Figure 28. Curve fitting for AC field simulation.

It should be noted at this point that the values of the electric field shown in Figures 27 and 28 are the root-mean-square values (rms or effective values) that are derived by (for a pure sinusoidal waveform):

$$f(x) = \sin x$$

$$rms = f_0 A = A \sqrt{\frac{1}{T} \int_0^T f^2(x) dx} = A \sqrt{\frac{1}{2\pi} \int_0^{2\pi} \sin^2 x dx} = A \sqrt{\frac{1}{2\pi} \sqrt{\pi}} = A \frac{1}{\sqrt{2}} = 0.707 \times A$$

$$\int_0^{2\pi} \sin^2 x dx = \left[\frac{x}{2} - \frac{\sin 2x}{4} \right]_0^{2\pi} = \frac{2\pi}{2} - \frac{\sin 4\pi}{4} + \frac{\sin 0}{4} = \pi \quad (30)$$

where A is the peak-to-peak amplitude of the AC bias.

Finally in Figure 29, a comparison of the normalized intensity ratios based on the DC and AC simulations for a bias of 209.50E-4 V/μm, is illustrated. The peak intensity with AC bias is higher than the equivalent with DC bias, reflecting a slightly lower effective field.

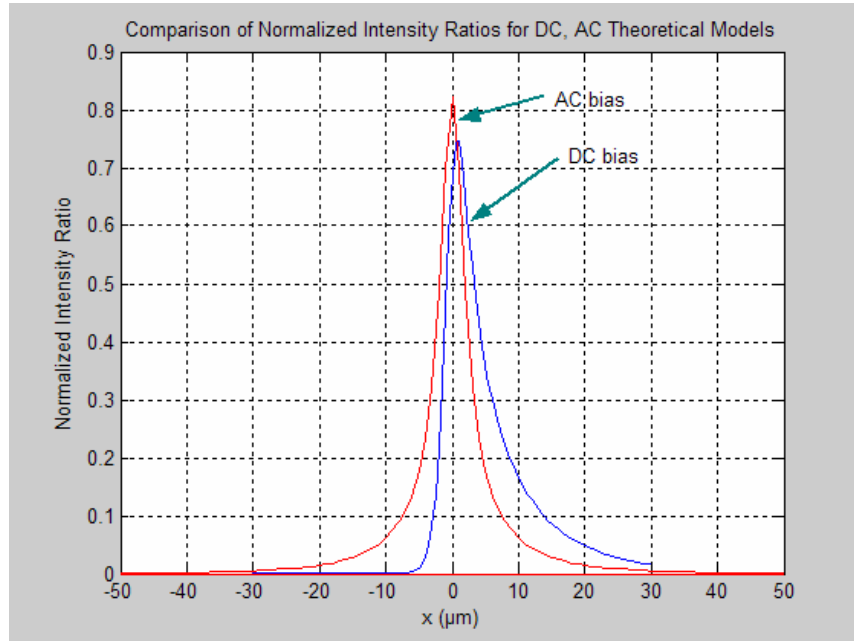


Figure 29. Comparison of DC and AC simulation models for E-field amplitude of 209.50E-4 V/μm.

THIS PAGE INTENTIONALLY LEFT BLANK

IV. ELECTRIC FIELD DISTRIBUTIONS: SIMULATION AND MEASUREMENT

A. 2-D ELECTRIC FIELD SIMULATIONS

In order to determine the extent to which the charge imaging can be used to map electric fields with high resolution, charge motion is imaged as a function of applied electric field in a variety of planar contact geometries. Transport behavior under the combined influence of both diffusion and drift can be predicted by using the simulation models described in Chapter III for diffusion and drift in 2D following generation at a point source. The overall method described in this chapter is based on a comparison of the experimental field measurements to 2D finite element field simulations for the structures of interest.

All the following cases have been evaluated experimentally on the $\text{Al}_{0.90}\text{Ga}_{0.10}\text{As}/\text{GaAs}/\text{Al}_{0.90}\text{Ga}_{0.10}\text{As}$ double heterostructure (Sample #9) described in detail in the previous chapter.

1. Case 1

In Figure 30 an overview of Sample #9 is shown to illustrate the overall procedure. In Case 1, 15 V DC has been applied across the contacts as shown in Figure 30. The SEM is operated in spot mode. The location of the electron beam with respect to the sample is represented with a red circle (for each position, P1, P2, Pn). The probe current was 3×10^{-10} A and the electron beam energy has been fixed at 30 keV. The dimensions of the study area also can be seen in Figure 30.

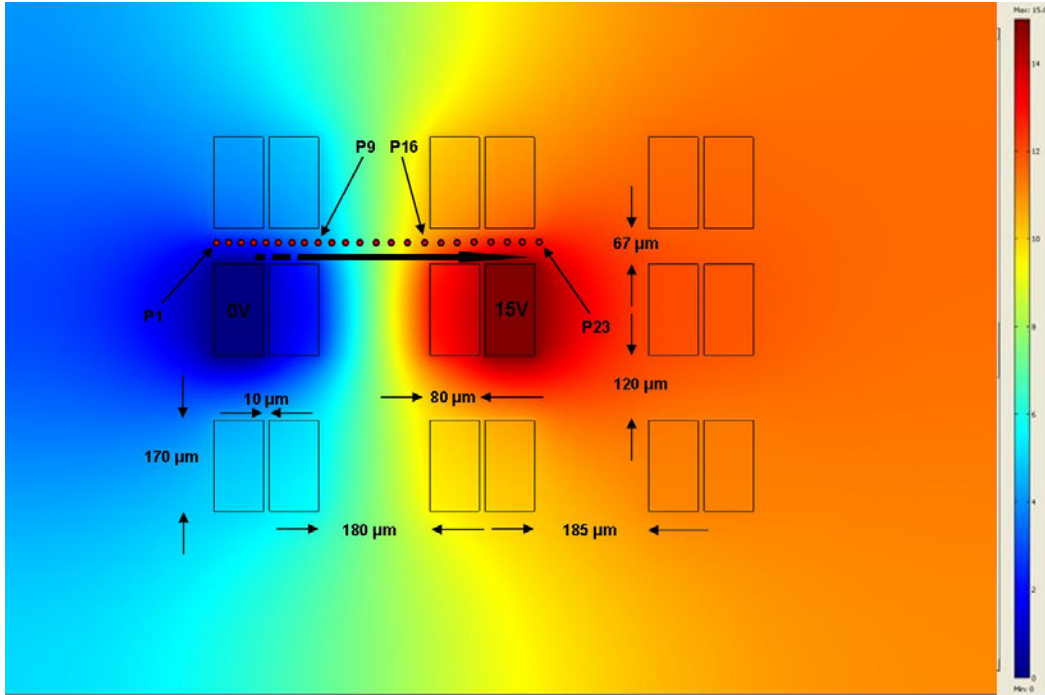


Figure 30. Sample #9 - Case 1.

In order to normalize the data from each measurement, two sets of data are obtained in each position: one with 0 V and one with the applied 15 V DC. The procedure of locally mapping the electric field based on the direct transport imaging technique includes the following:

- Image the charge recombination length in each position first with no bias and then with applied bias.
- Extract the “.tif” images created in the MicroCCD software to a MATLAB program and find the value of peak intensity in each case.
- Evaluate the normalized intensity of each case based on the measurements with and without bias.
- Create a graph of normalized intensity ratio as a function of distance, based on the experimental measurements.
- Combine the previous graph with the data obtained from the theoretical model of intensity as a function of distance for DC applied electric field as analyzed previously and apply the curve fitting equation to obtain a graph of electric field as a function of distance.

The MATLAB code created for this purpose can be seen in Appendix B.

The results of the above procedure for DC applied field can be seen in Figures 31 and 32. Figure 31 represents the normalized intensity ratio with respect to the distance, based on the SEM experimental measurements. Figure 32 represents the electric field magnitude with respect to distance, based on the procedure developed in order to map the electric field through the transport imaging technique. By comparing the two figures it can be seen that when the normalized intensity ratio increases, the magnitude of the electric field at the same point decreases and vice-versa.

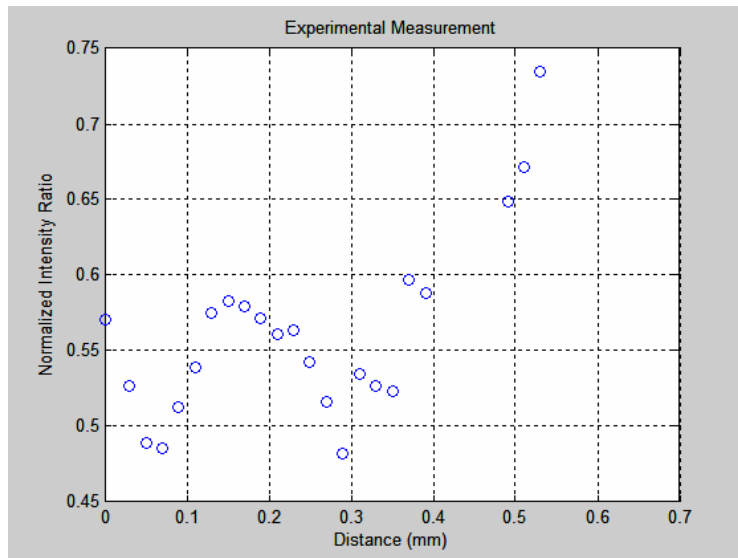


Figure 31. Normalized intensity ratio vs. Distance for Case 1 (DC applied field).

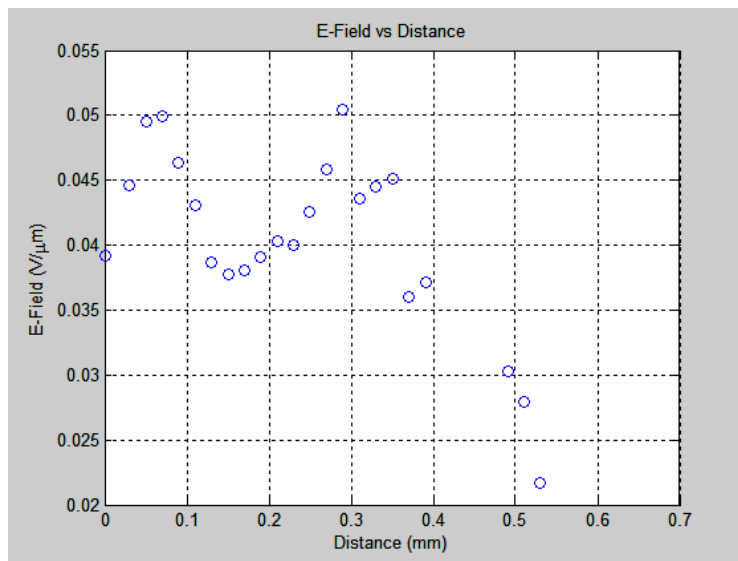


Figure 32. E-Field vs. Distance for Case 1 (DC applied field).

By repeating the above method with AC applied electric field (15 V AC) and keeping all the other parameters unchanged, the corresponding graphs can be seen in Figures 33 and 34. The reason for using AC electric field is for comparison purposes with respect to DC applied field and for increasing image information due to the fact that the drift and diffusion is simultaneously observed in both directions.

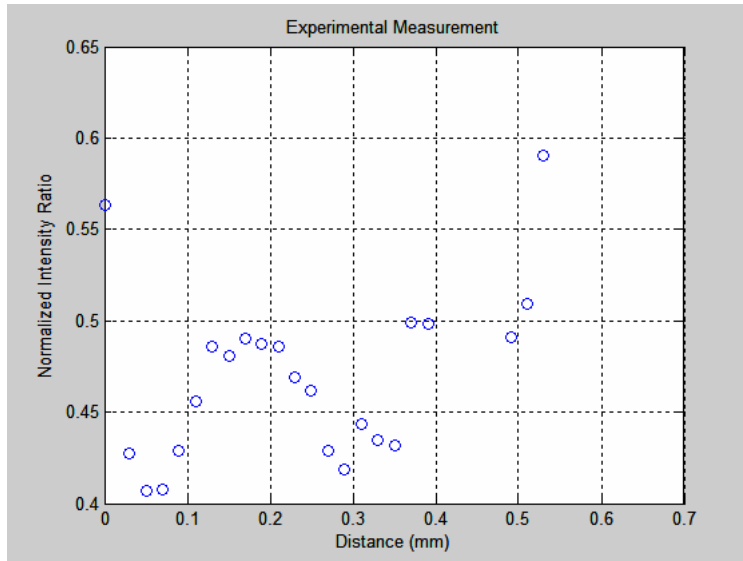


Figure 33. Normalized intensity ratio vs. Distance for Case 1 (AC applied field).

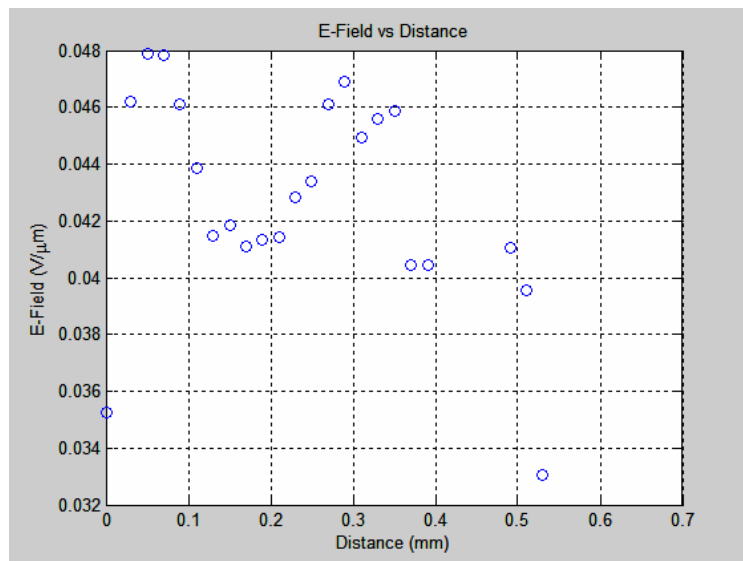


Figure 34. E-Field vs. Distance for Case 1 (AC applied field).

From Figures 33 and 34, it can be seen that the application of AC bias instead of DC bias does not alter either the shape of the graphs or significantly the magnitude of the electric field at the same points of interest. This can be seen clearly in Figure 35 where a comparison of the AC-DC applied field results has been done. In the DC case the magnitude of the electric field is higher on the regions where the field is stronger and lower than the AC values in regions where the field is lower.

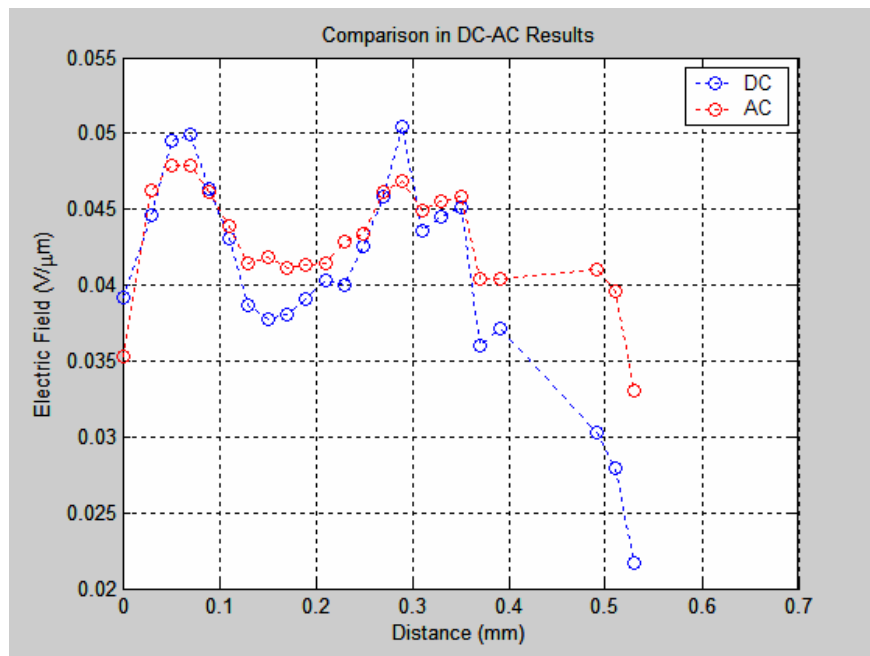


Figure 35. Comparison of the results of magnitude of electric field with DC and AC bias for Case 1.

2. Case 2

In Case 2, 15 V DC has been applied between the contacts as shown in Figure 36. The SEM is again operated in spot mode. The location of the electron beam with respect to the sample is represented with a red circle (for each position). The probe current was 3×10^{-10} A and the electron beam energy was 30 keV.

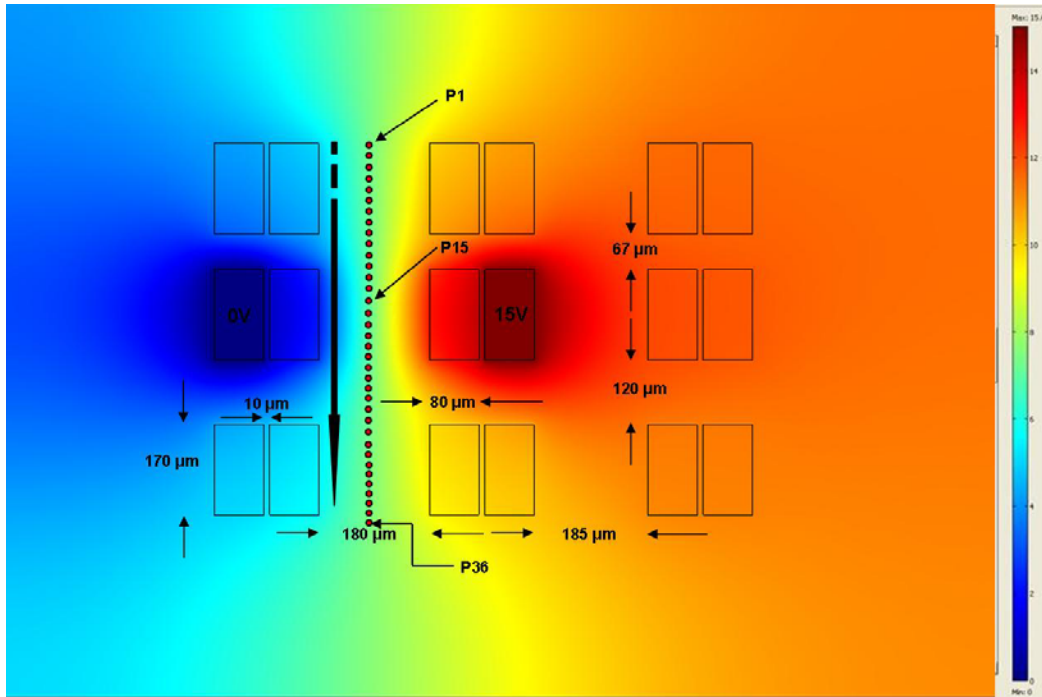


Figure 36. Sample #9 - Case 2.

Note that Figure 36 demonstrates the electric potential distribution as calculated in COMSOL MULTIPHYSICS (Version 3.3) software. The magnitude of the potential in each region is represented by different colors and the corresponding values are shown in the color scale in the right part of the graph. With application of 15 V DC, the corresponding normalized intensity ratio and electric field graphs are shown in Figures 37 and 38.

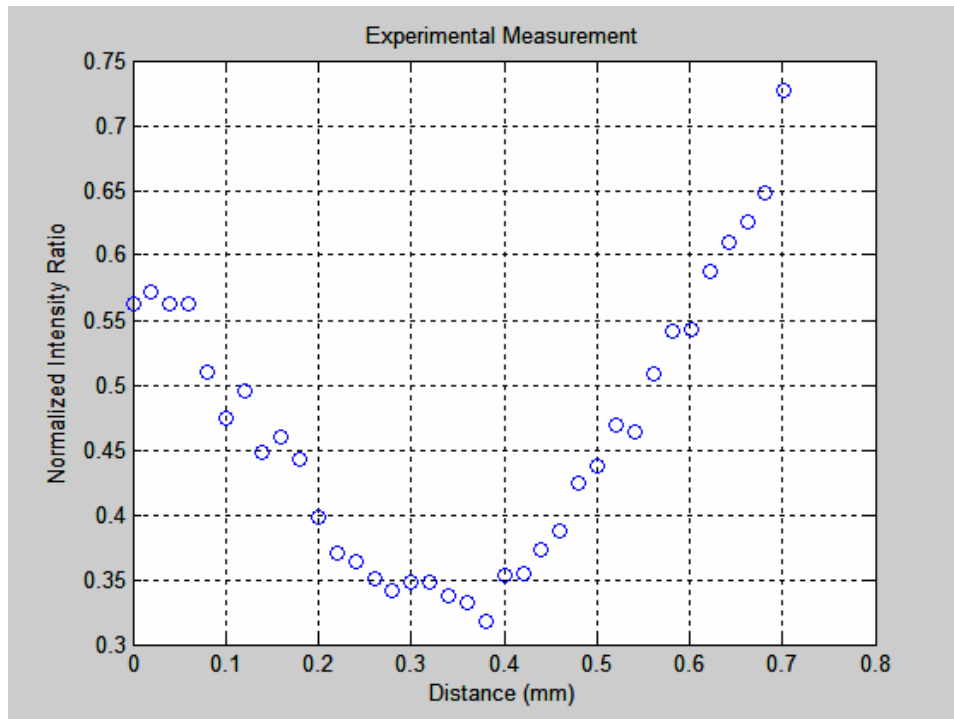


Figure 37. Normalized intensity ratio vs. Distance for Case 2 (DC applied field).

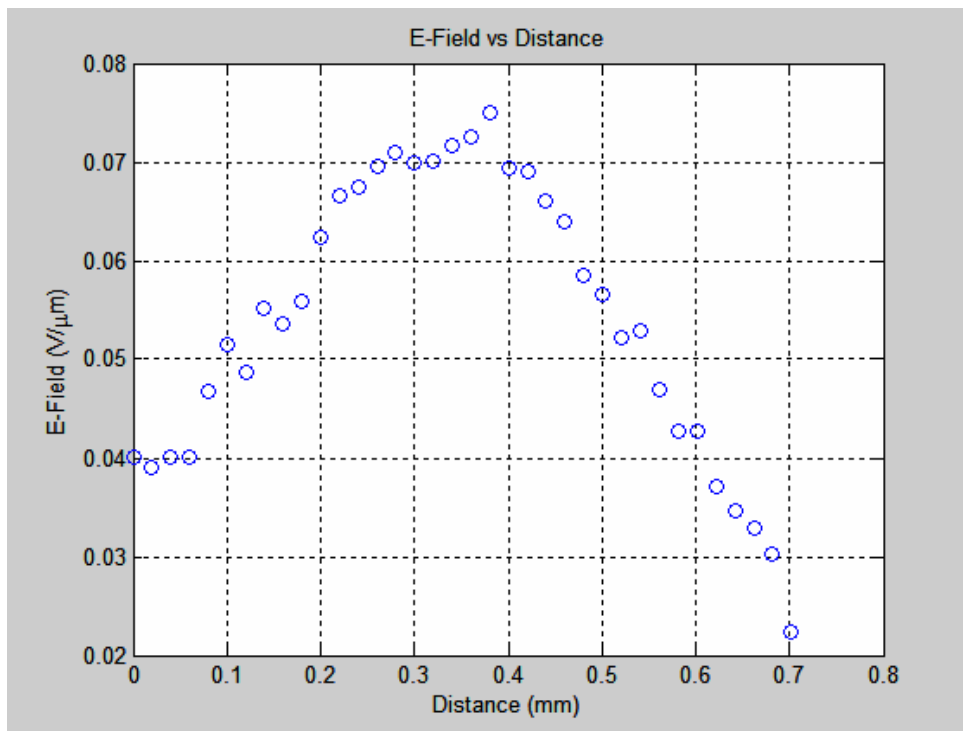


Figure 38. E-Field vs. Distance for Case 2 (DC applied field).

For the AC case, the corresponding normalized intensity ratio and electric field graphs are shown in Figures 39 and 40.

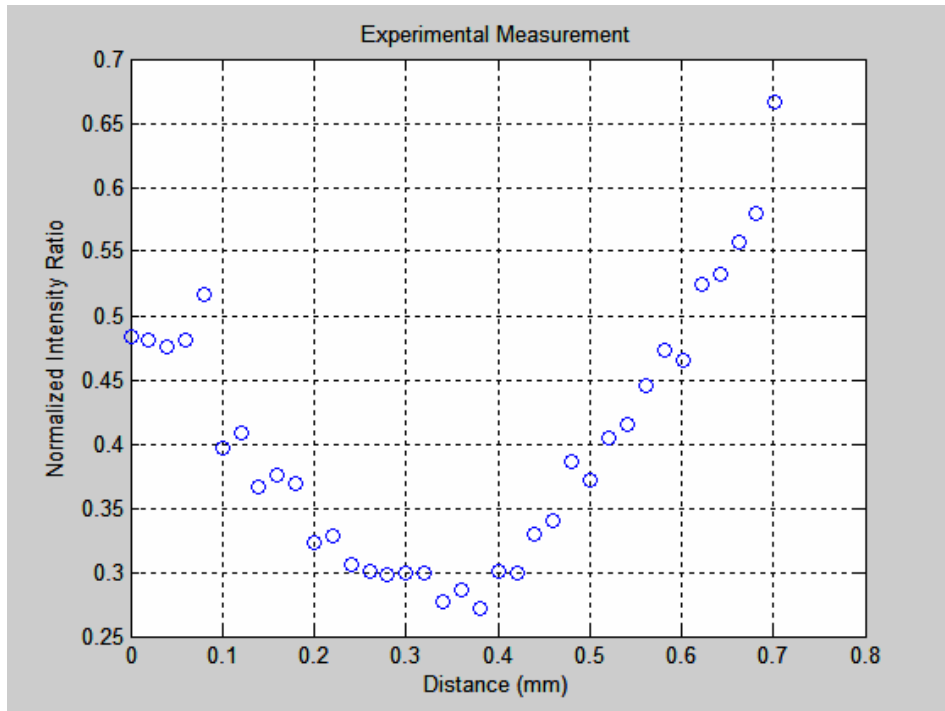


Figure 39. Normalized intensity ratio vs. Distance for Case 2 (AC applied field).

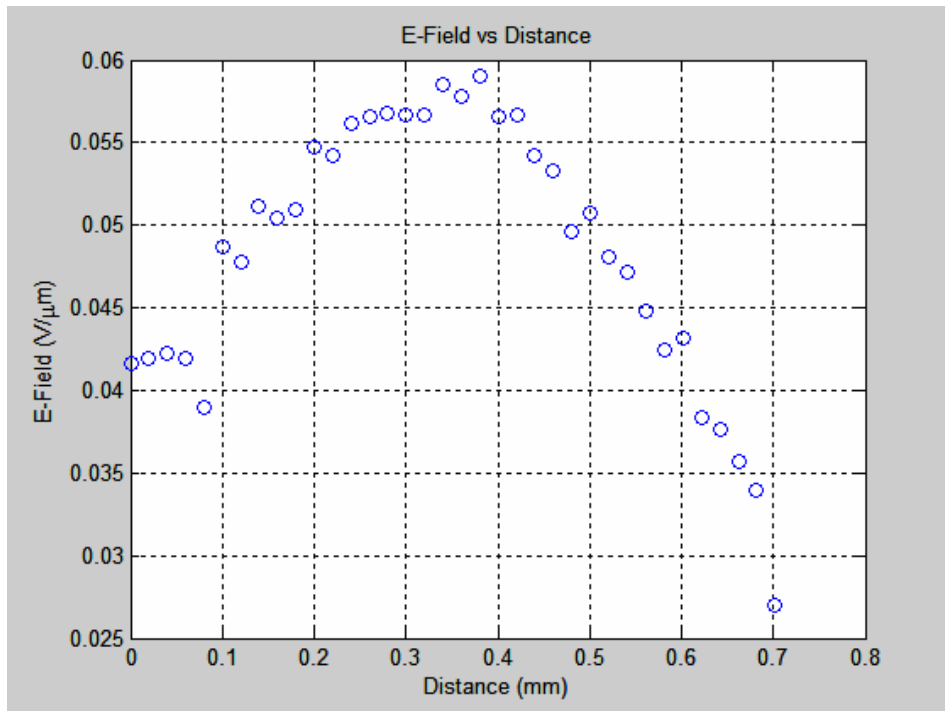


Figure 40. E-Field vs. Distance for Case 2 (AC applied field).

As in Case 1, the comparison of DC and AC applied bias results show (Figure 41) that the DC values are higher than the AC results (almost 20% in the strong field region) and a little lower than the AC in the weak electric field region (almost 3%).

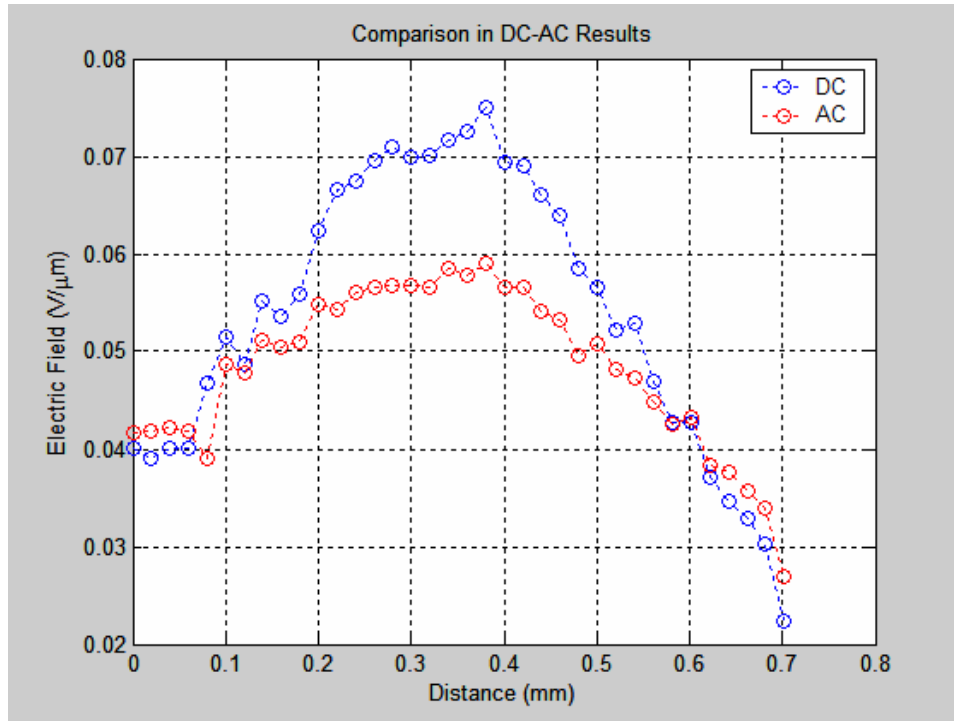


Figure 41. Comparison of the results of magnitude of electric field with DC and AC bias for Case 2.

3. Case 3

In Case 3, 15 V DC has been applied between the contacts as shown in Figure 42 with the same experimental parameters as in the previous cases. For the case of DC bias, the corresponding normalized intensity ratio and electric field graphs are shown in Figures 43 and 44.

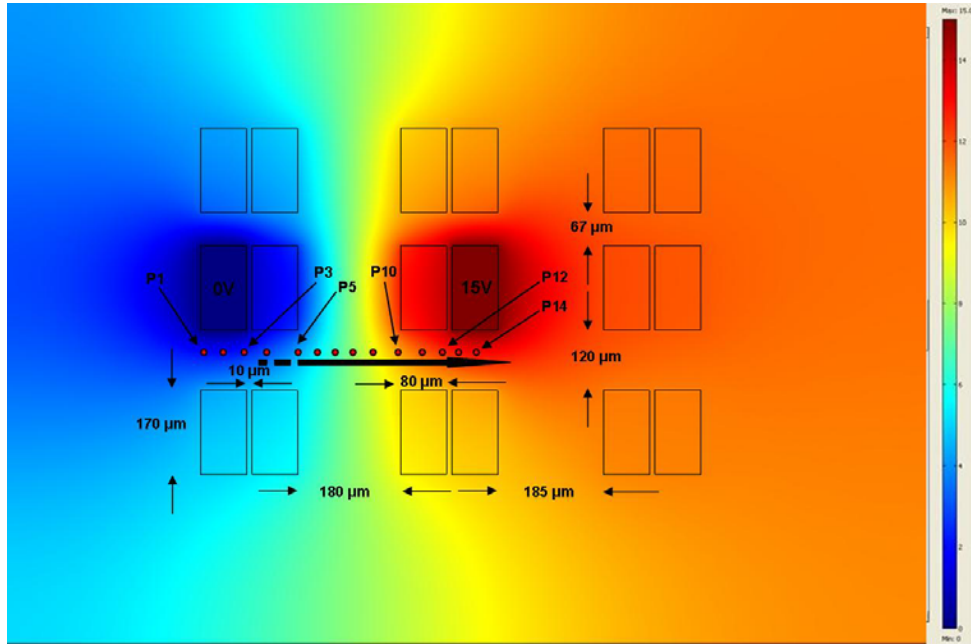


Figure 42. Sample #9 - Case 3.

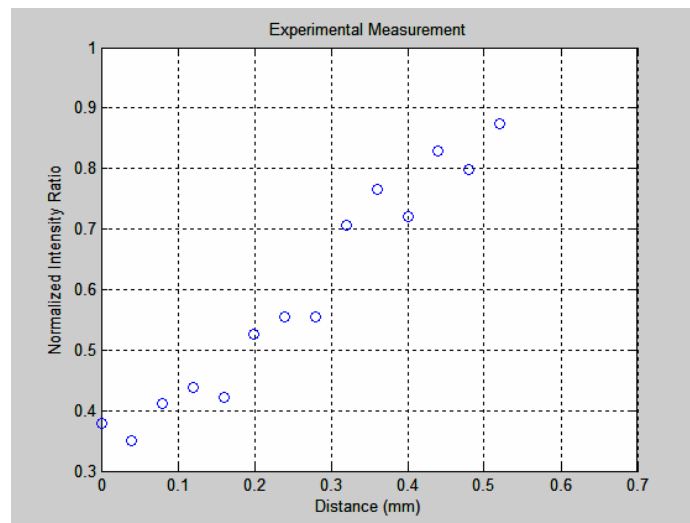


Figure 43. Normalized intensity ratio vs. Distance for Case 3 (DC applied field).

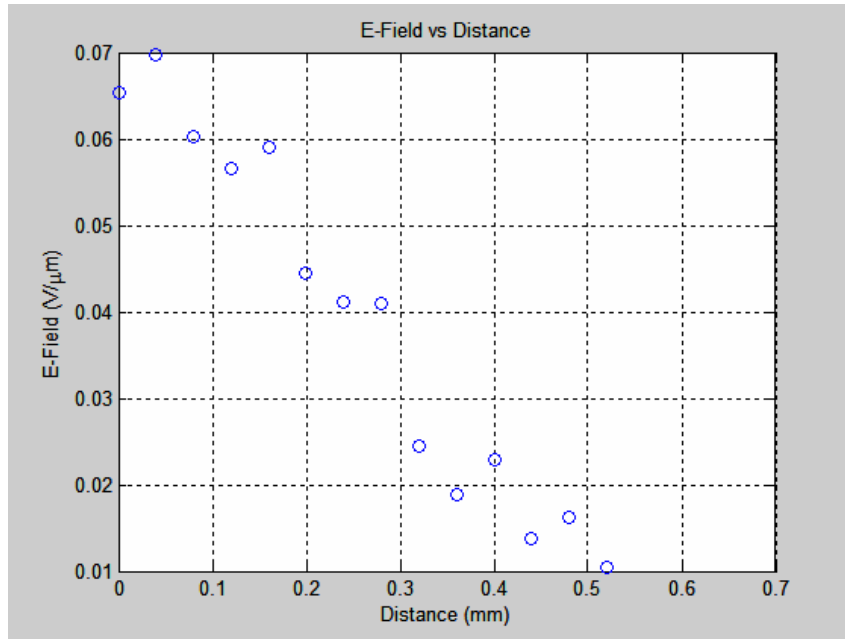


Figure 44. E-Field vs. Distance for Case 3 (DC applied field).

Additionally, a similar experimental measurement was made with the same parameters, except that the cabling and the polarity have been reversed. The result is illustrated in Figure 45 below. The corresponding normalized intensity ratio and electric field graphs are shown in Figures 46 and 47 below.

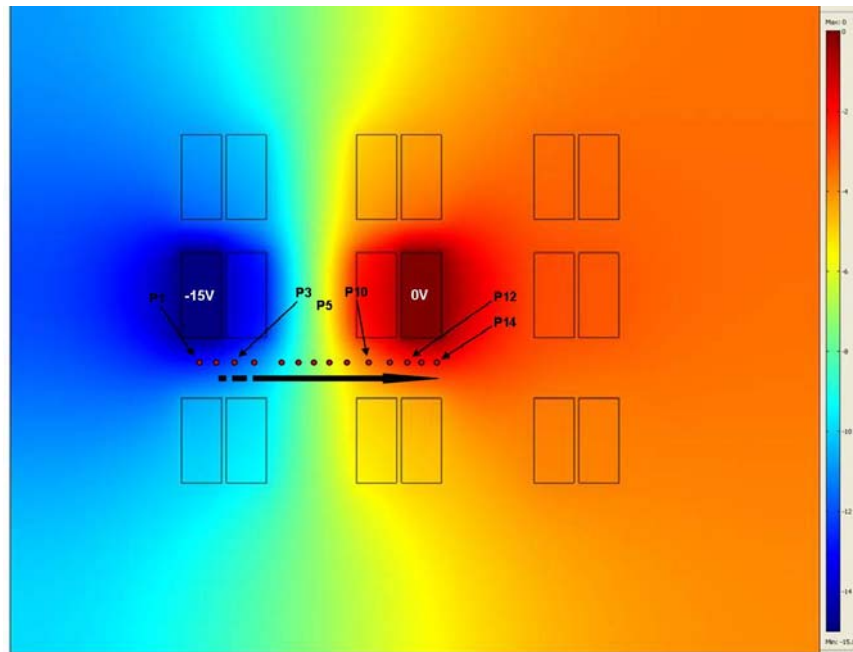


Figure 45. Sample #9 (Reversed cabling and polarity).

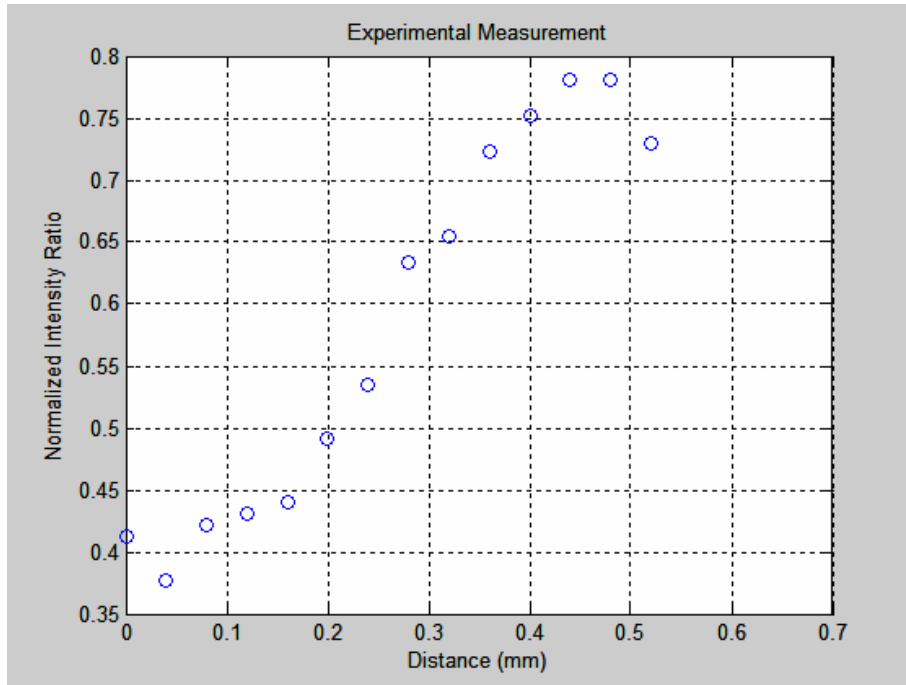


Figure 46. Normalized intensity ratio vs. Distance for Case 3 (DC applied field, reversed cabling and polarity).

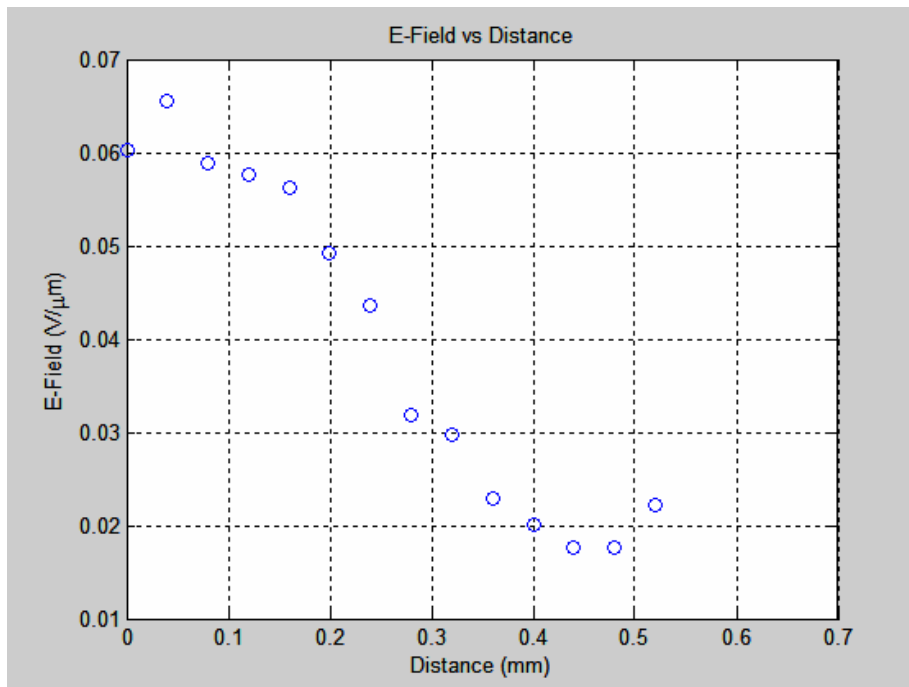


Figure 47. E-Field vs. Distance for Case 3 (DC applied field, reversed cabling and polarity).

Although the cases shown in Figures 42 and 45 might seem different, they are identical. In both cases the electric potential is the same as the polarity of the applied bias and the SEM cabling to the sample have been reversed simultaneously. By comparing Figures 44 and 47 it can be seen that due to the reversed cabling and polarity in the same structure, the magnitude of the electric field with respect to distance at each point of interest, is not identical as theoretically was anticipated. The reason for the same electric potential for both cases is due to the fact that the reversed polarity (from positive +15V to negative -15V) reverses the field but by switching the cabling of the SEM the resulting field is the initial case. This can be seen clearly in Figure 48 where a comparison of the two cases is demonstrated. The voltage drop at metal-semiconductor material interface is not always symmetric. For this reason there are some fluctuations in the magnitude of the electric field ($\approx 4\%$).

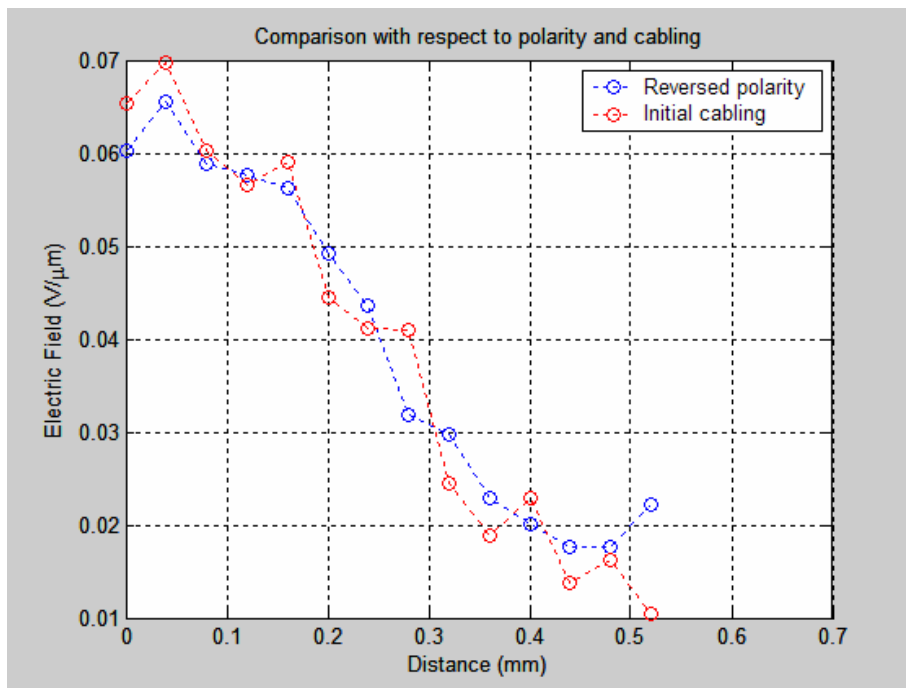


Figure 48. Comparison for Case 3 results (DC applied field, reversed cabling and polarity).

4. Case 4

In Case 4, 15 V DC has been applied between the contacts as shown in Figures 49 and 50.

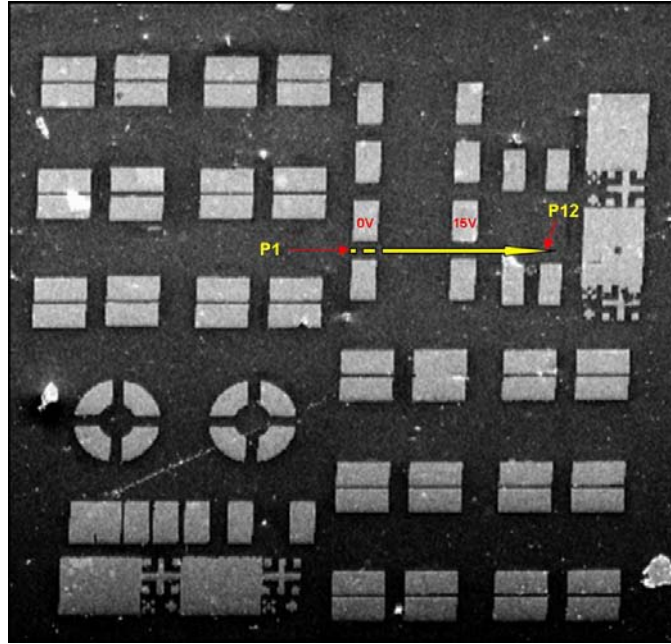


Figure 49. Sample #9 (SEM photo) – Case 4 (2031 μm X 2090 μm).

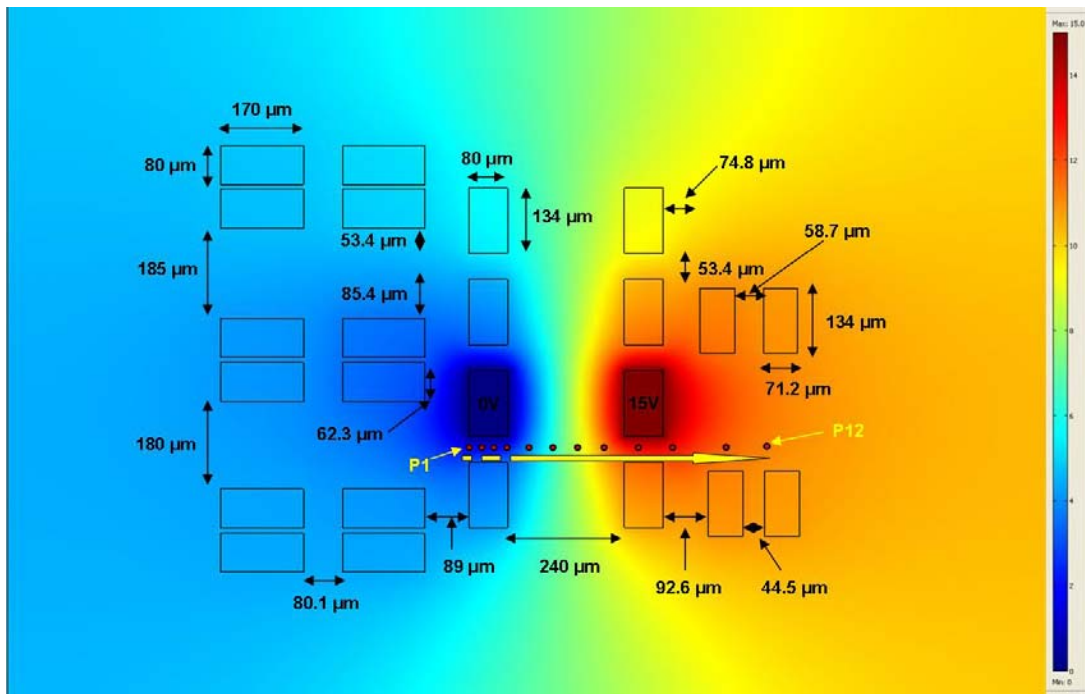


Figure 50. Sample #9 – Case 4 (Created in COMSOL MULTIPHYSICS).

The SEM is operated in spot mode. Twelve measurements of the intensity have been made across the yellow arrow. The probe current was 3×10^{-10} A and the electron beam energy was at 30 keV. The corresponding graphs of the normalized intensity ratio and electric field are shown in Figures 51 and 52.

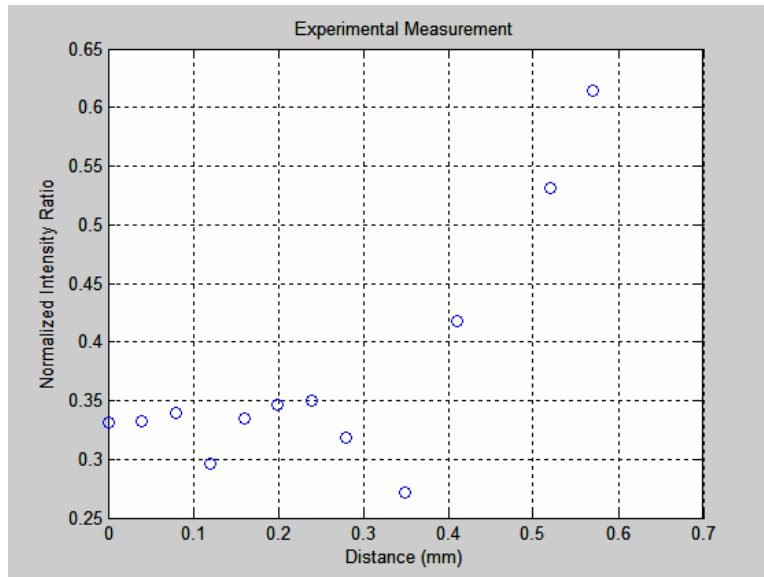


Figure 51. Normalized intensity ratio vs. Distance for Case 4 (DC applied field).

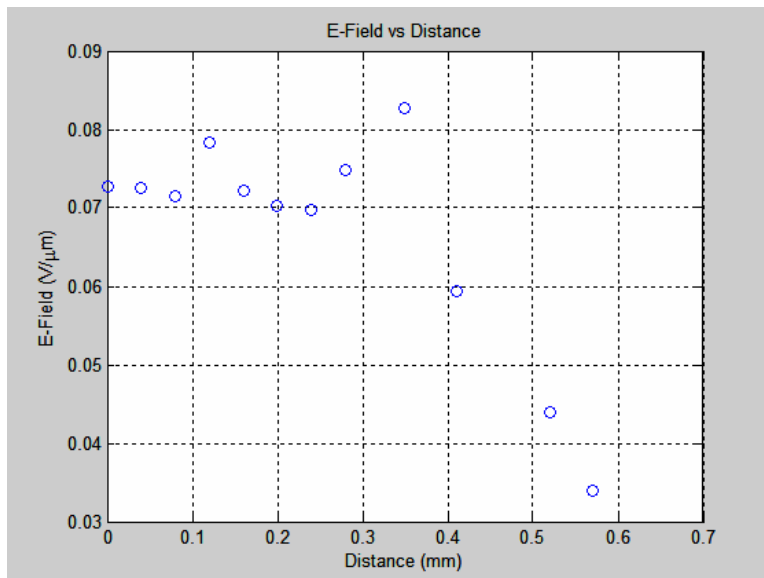


Figure 52. E-Field vs. Distance for Case 4 (DC applied field).

By applying 15 V AC in the above configuration the corresponding graphs of the normalized intensity and electric field are given in Figures 53 and 54.

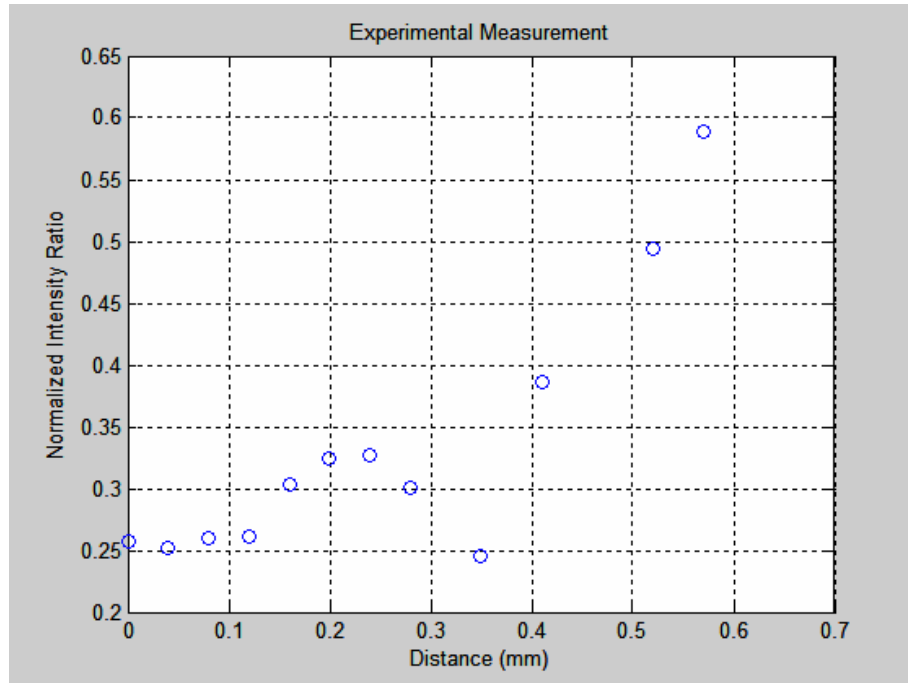


Figure 53. Normalized intensity ratio vs. Distance for Case 4 (AC applied field).

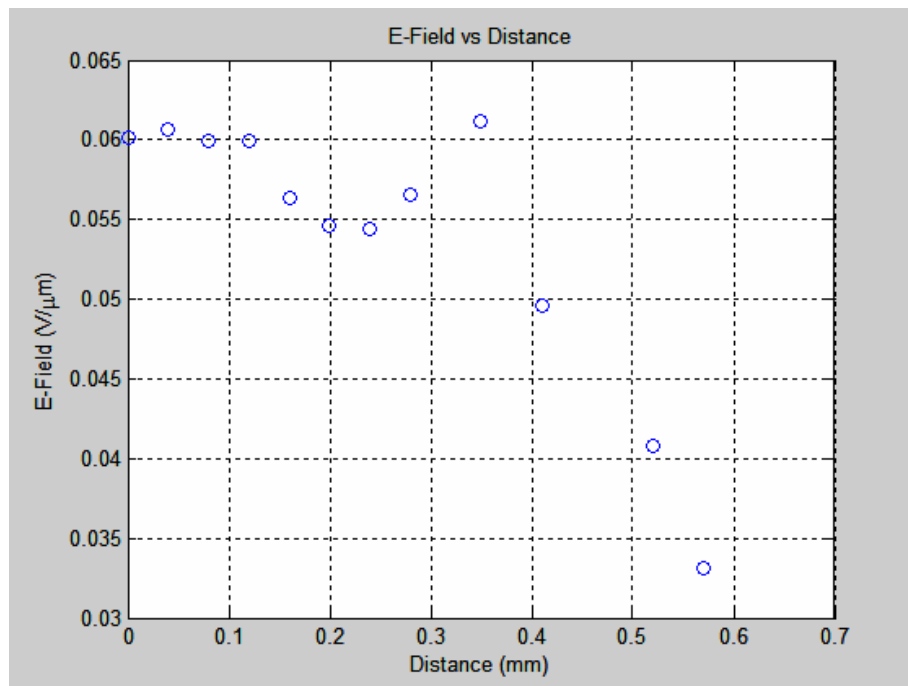


Figure 54. E-Field vs. Distance for Case 4 (AC applied field).

From Figure 55 it can be seen that the DC results for the magnitude of the electric field are higher than the equivalent of the AC results, as expected, by about 21%. Again in the region of weak electric field the AC and DC values converge.

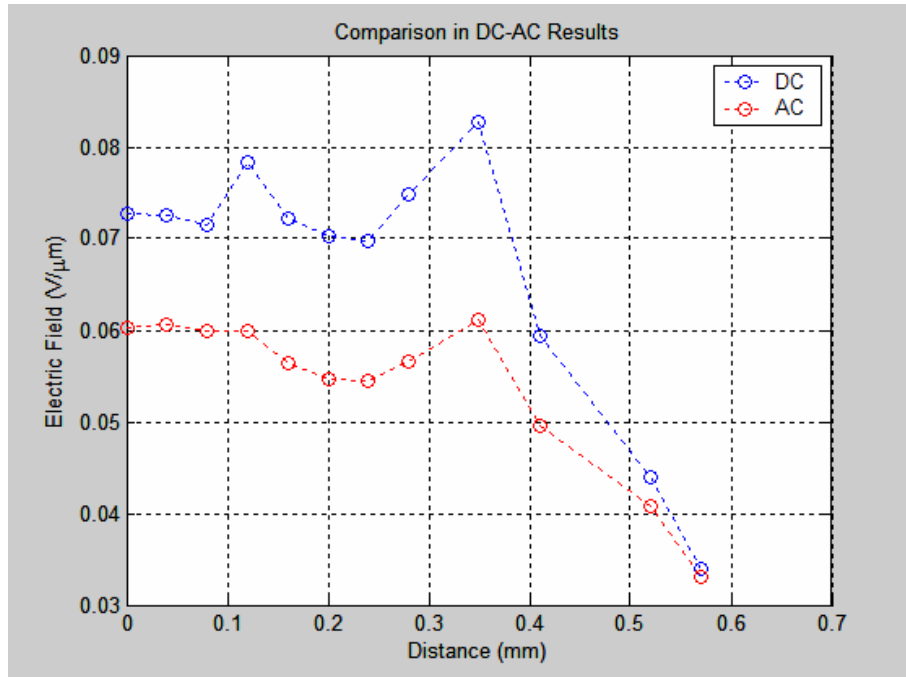


Figure 55. Comparison of the results of magnitude of electric field with DC and AC bias for Case 4.

5. Case 5

In Case 5, 15 V DC have been applied between the contacts as shown in Figures 56 and 57.

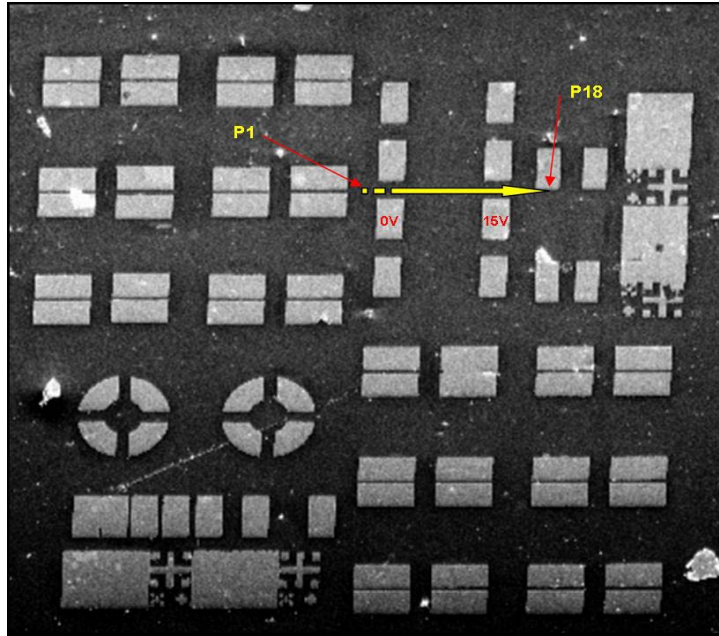


Figure 56. Sample #9 (SEM photo) – Case 5 (2031 μm X 2090 μm).

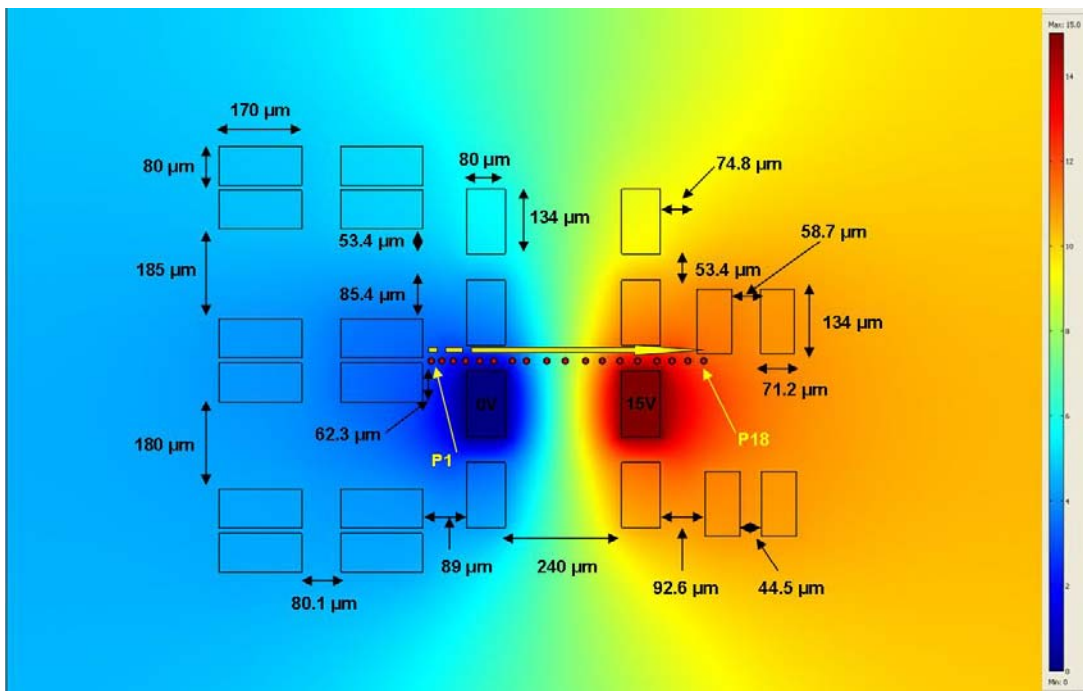


Figure 57. Sample #9 – Case 5 (Created in COMSOL MULTIPHYSICS).

The SEM is operated in spot mode. Eighteen consecutive measurements of the intensity have been made across the yellow arrow. The probe current was 3×10^{-10} A and the electron beam energy was 30 keV. The corresponding graphs of the normalized intensity ratio and the electric field are shown in Figures 58 and 59.

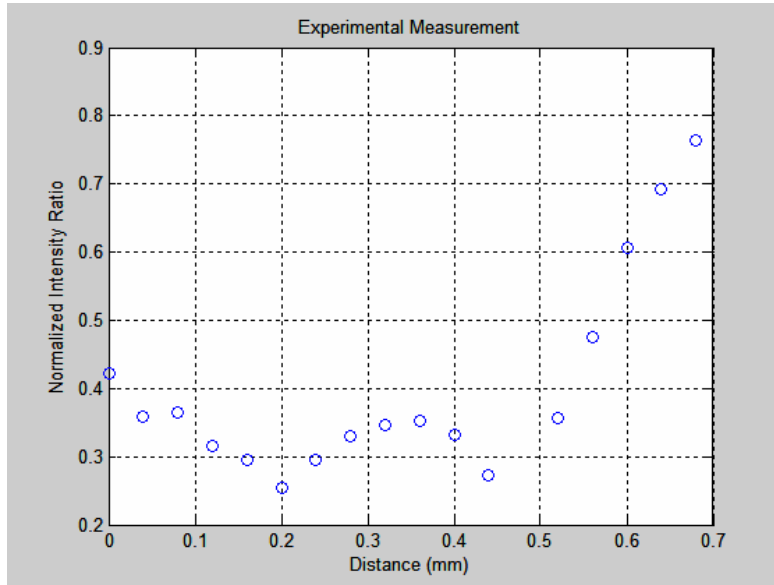


Figure 58. Normalized intensity ratio vs. Distance for Case 5 (DC applied field).

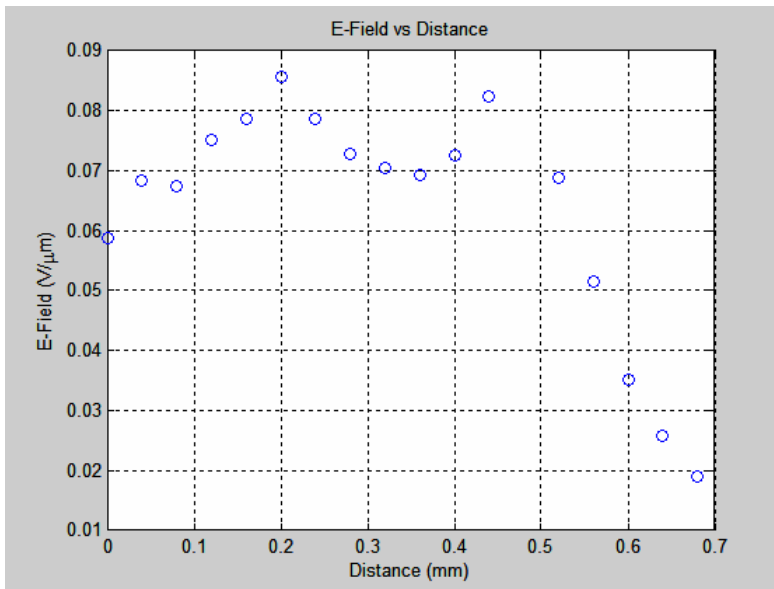


Figure 59. E-Field vs. Distance for Case 5 (DC applied field).

By applying 15 V AC in the above configuration the corresponding graphs of normalized intensity ratio and electric field are shown in Figures 60 and 61 below.

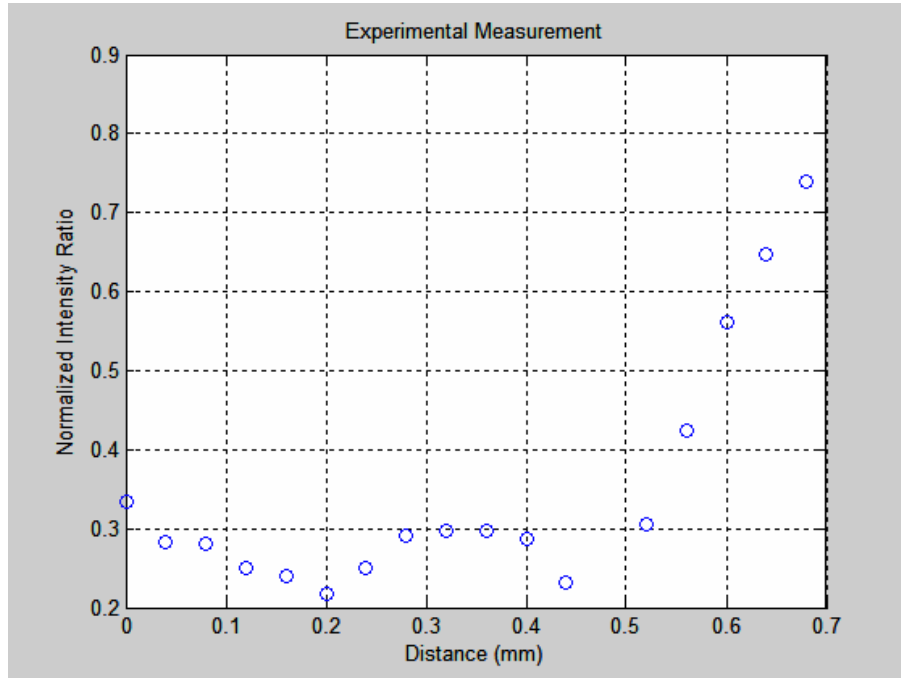


Figure 60. Normalized intensity ratio vs. Distance for Case 5 (AC applied field).

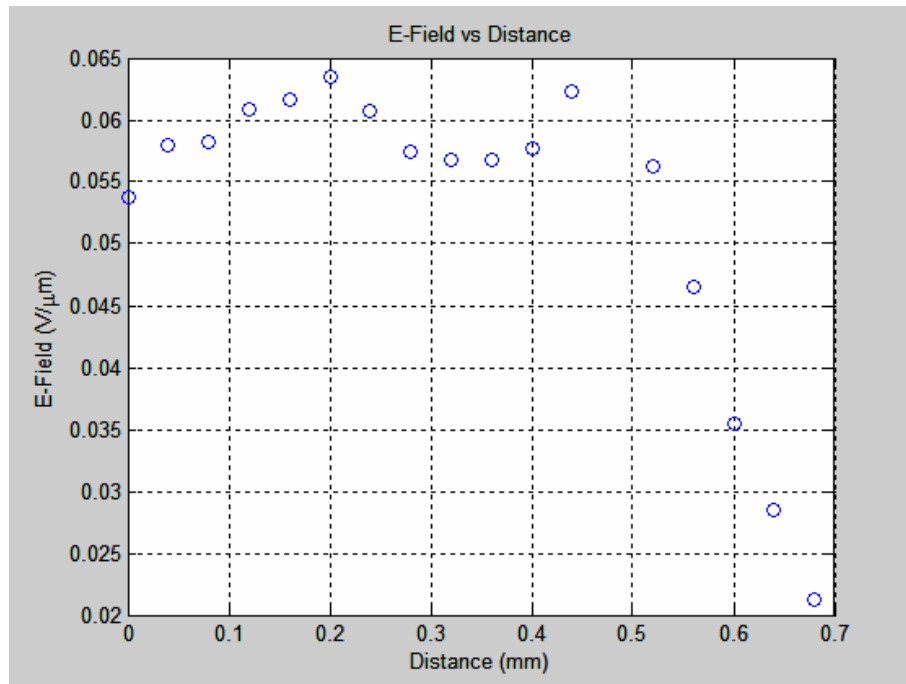


Figure 61. E-Field vs. Distance for Case 5 (AC applied field).

In Figure 62 it can be seen again that the AC results for the electric field magnitude are lower than the equivalent DC results by about 20% except in the regions of weak electric field where the AC values are almost identical with the equivalent DC values.

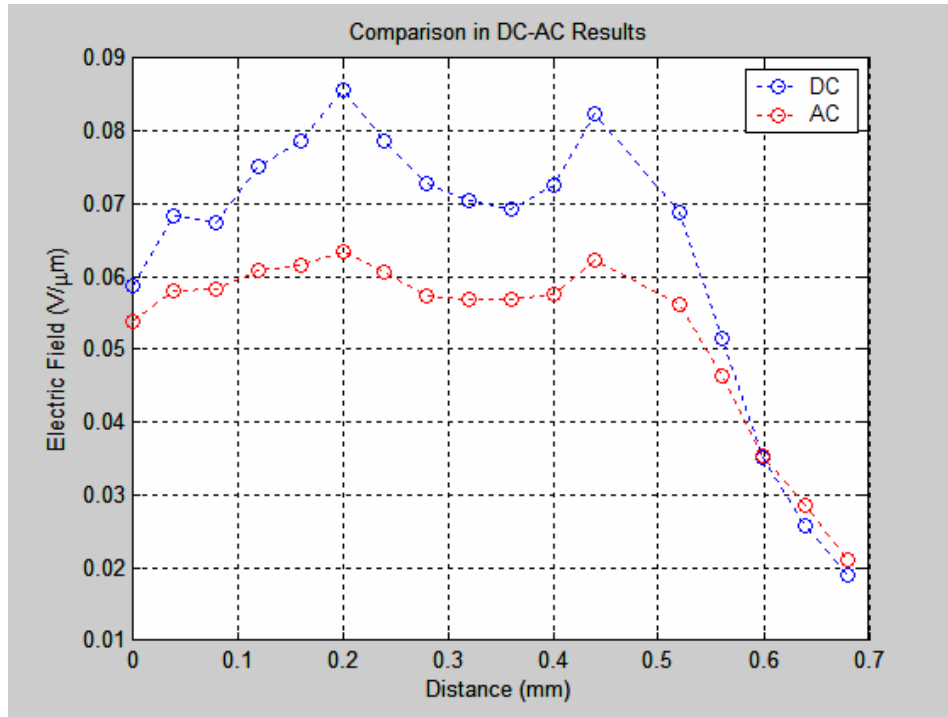


Figure 62. Comparison of the results of magnitude of electric field with DC and AC bias for Case 5.

6. Case 6

In Case 6, 15 V DC has been applied between the contacts as shown in Figures 63 and 64.

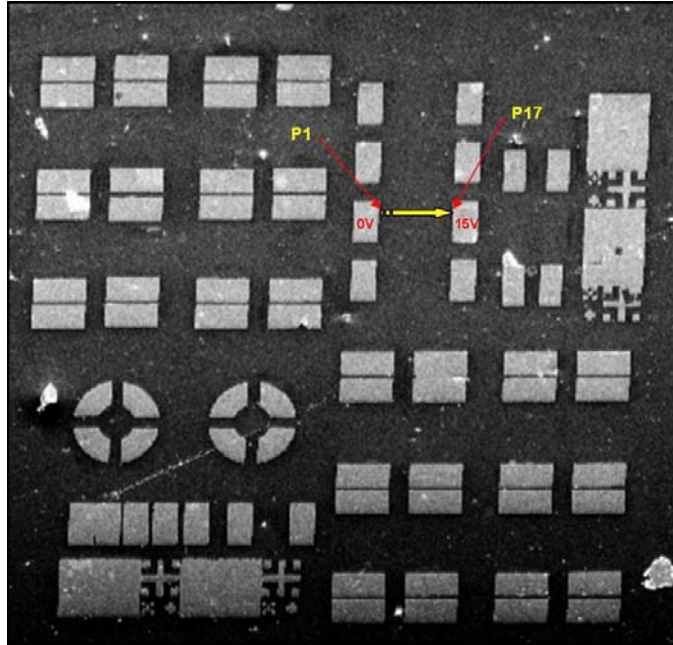


Figure 63. Sample #9 (SEM photo) – Case 6 (2031 μm X 2090 μm).

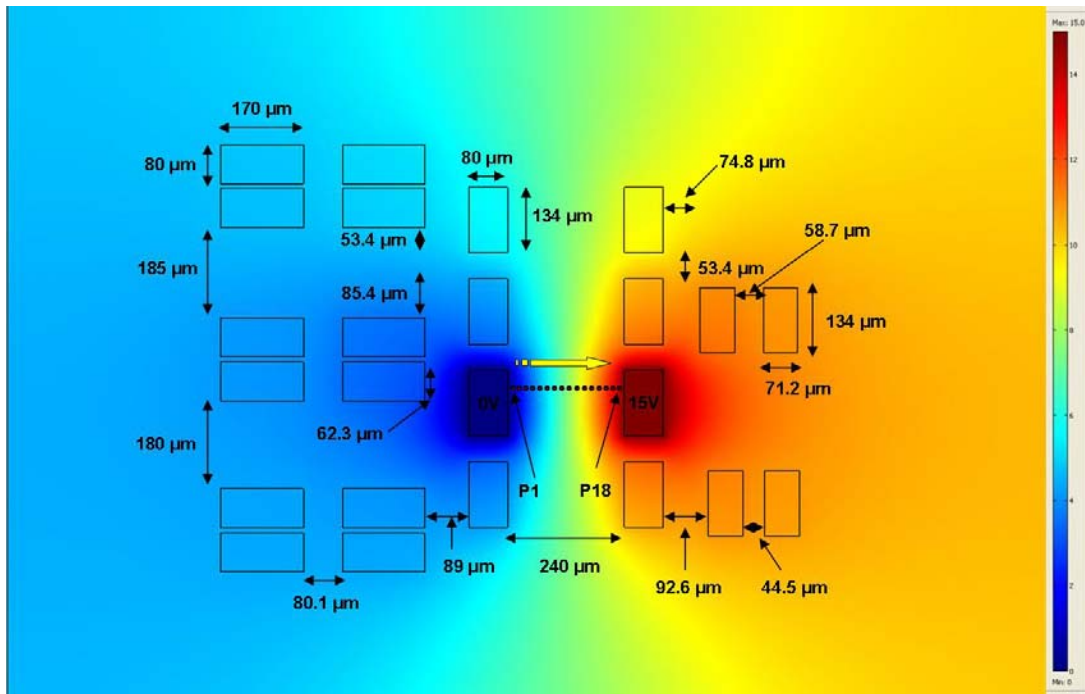


Figure 64. Sample #9 – Case 6 (Created by COMSOL MULTIPHYSICS).

The SEM is operated in spot mode. Seventeen consecutive measurements of the intensity have been made across the yellow arrow. The probe current was 3×10^{-10} A and the electron beam energy was at 30 keV. The electric field between the plates is uniform except in the region right next to the plates. The corresponding graphs can be seen below in Figures 65 and 66.

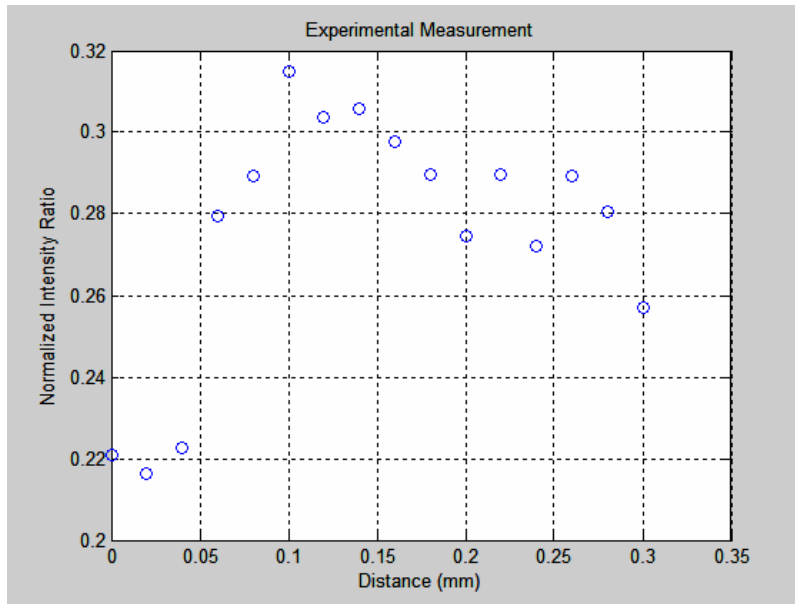


Figure 65. Normalized intensity ratio vs. Distance for Case 6 (DC applied field).

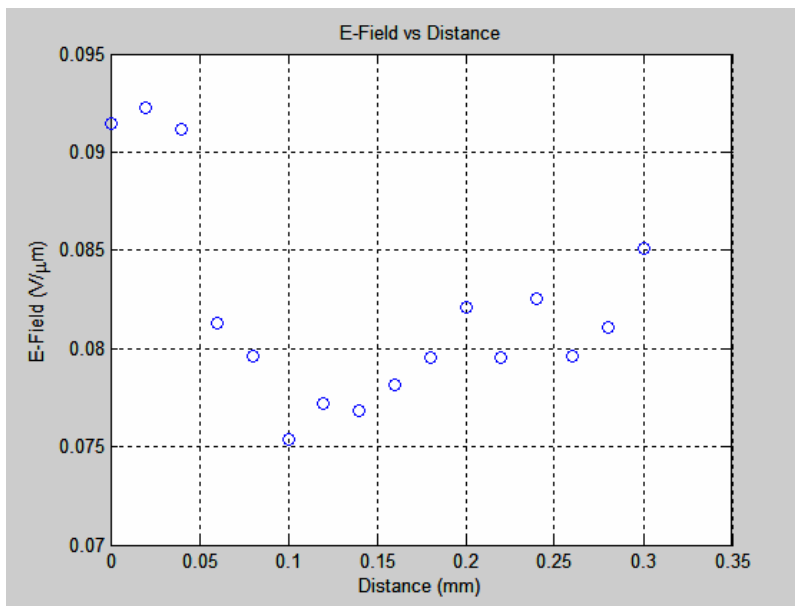


Figure 66. E-Field vs. Distance for Case 6 (DC applied field).

By applying 15 V AC in the above configuration the corresponding graphs are shown in Figures 67 and 68 below.

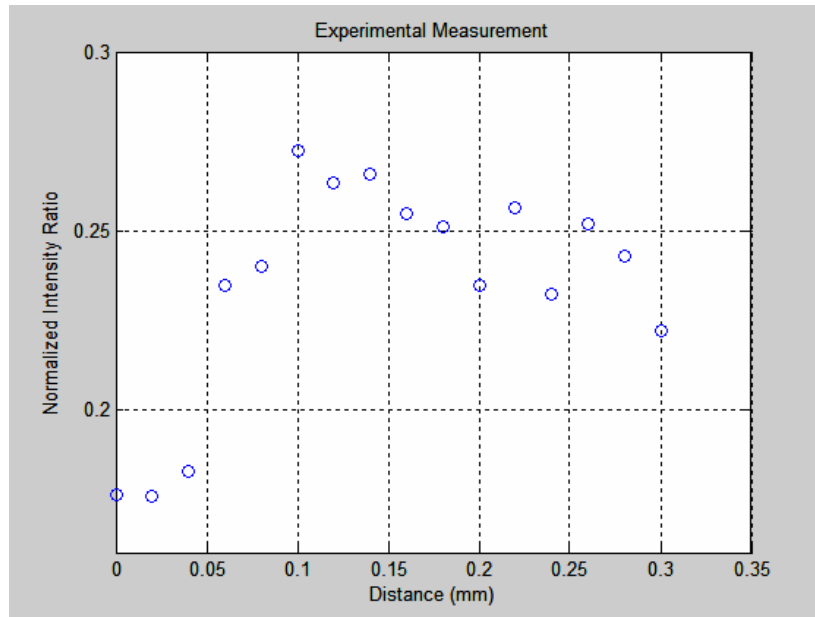


Figure 67. Normalized intensity ratio vs. Distance for Case 6 (AC bias).

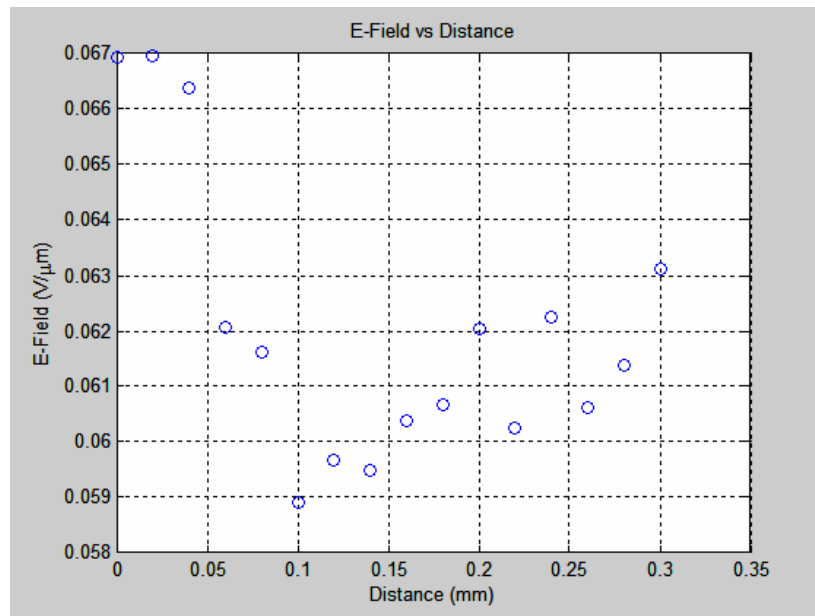


Figure 68. E-Field vs. Distance for Case 6 (AC bias).

In Figure 69 below it can be seen that the values of the electric field with the AC bias case are lower than the equivalent with DC bias in the whole region by about 25%.

The fluctuations of the magnitude of the electric field in the region between the contacts seem to be different from what was expected since the field is uniform except for a small area in proximity to the metal contacts. But these fluctuations are very small in magnitude and this can be seen clearly in Figure 70 where the y-axis has been expanded to be consistent with earlier graphs and the values of the electric field are almost all in a line as expected for a uniform electric field. However, the experimental technique is sensitive to any variations in field associated with material non-uniformity.

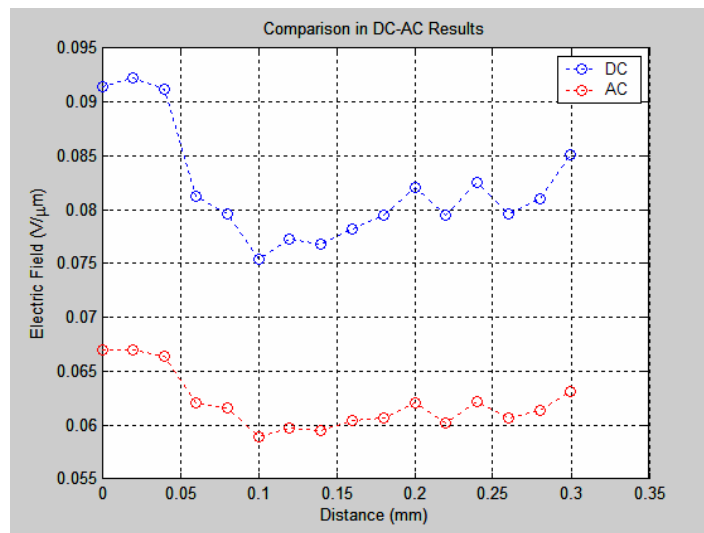


Figure 69. Comparison of the results of magnitude of electric field with DC and AC bias for Case 6.

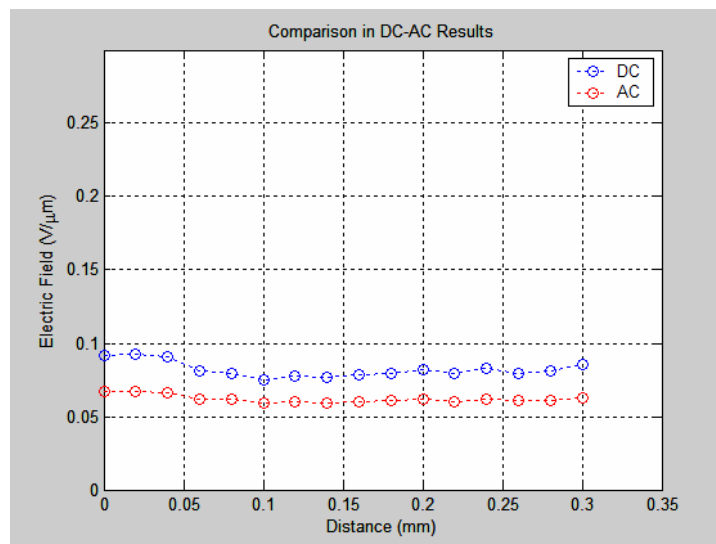


Figure 70. DC and AC bias comparison (different scaling).

By comparing all the previous cases, the consistent variation between the DC and AC applied field cases suggests either:

- Some additional correction is needed to the AC modeling, or
- There is an increased contact resistance when AC bias is applied.

The fact that the difference depends on the magnitude of the E-field suggests a possible contact effect, even at this relatively low frequency.

B. VISUALIZATION OF THE ELECTRIC FIELD

One very important aspect of the method described in this thesis is the capability of visualizing the direction of the electric field locally. In order to demonstrate this, the case shown in Figure 71 will be used. The SEM is operated in line mode (scanning direction is represented with the yellow arrow). The results are illustrated in Figure 72.

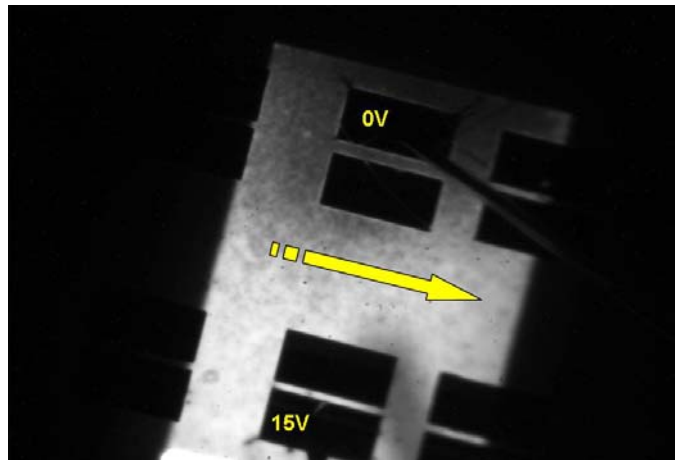


Figure 71. Direction of the electric field with SEM in line mode (874 μm X 589 μm).

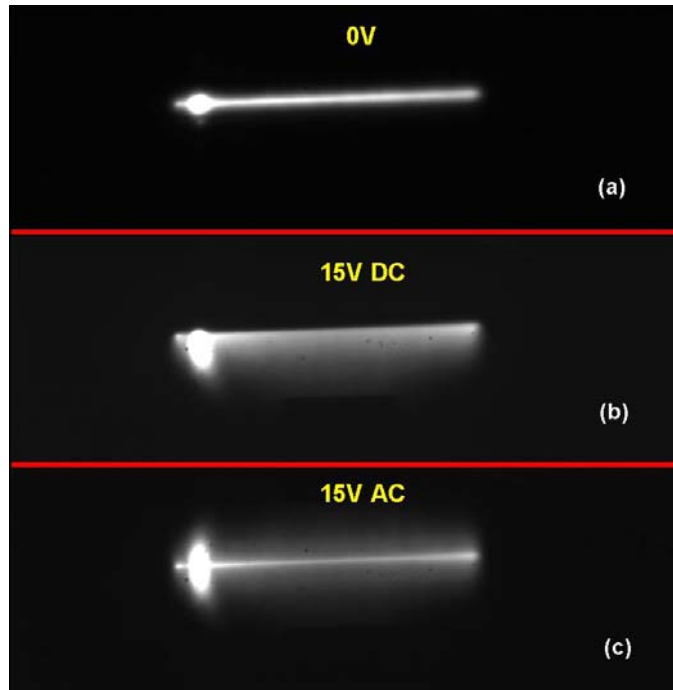


Figure 72. Line mode in defining the direction of the electric field (each image is 872 μm X 293 μm).

In Figure 72 the direction of the electric field can be directly observed. In part (a) of Figure 72, no voltage is applied. In part (b) 15 V DC have been applied between the contacts. The drift of the minority carriers (electrons) is towards the positively charged plate. In part (c) 15 V AC have been applied to the above configuration. This results in a symmetrical shape of the line mode as the voltage polarity oscillates. Again, it should be noted that the bright spot shown in the left of each line is an artifact of the SEM imaging process due to the synchronization of the electron beam (SEM always scans the beam longer along one edge of the scanning area).

Additionally, by operating the SEM in picture mode, generation over the whole region is illustrated in Figure 73.

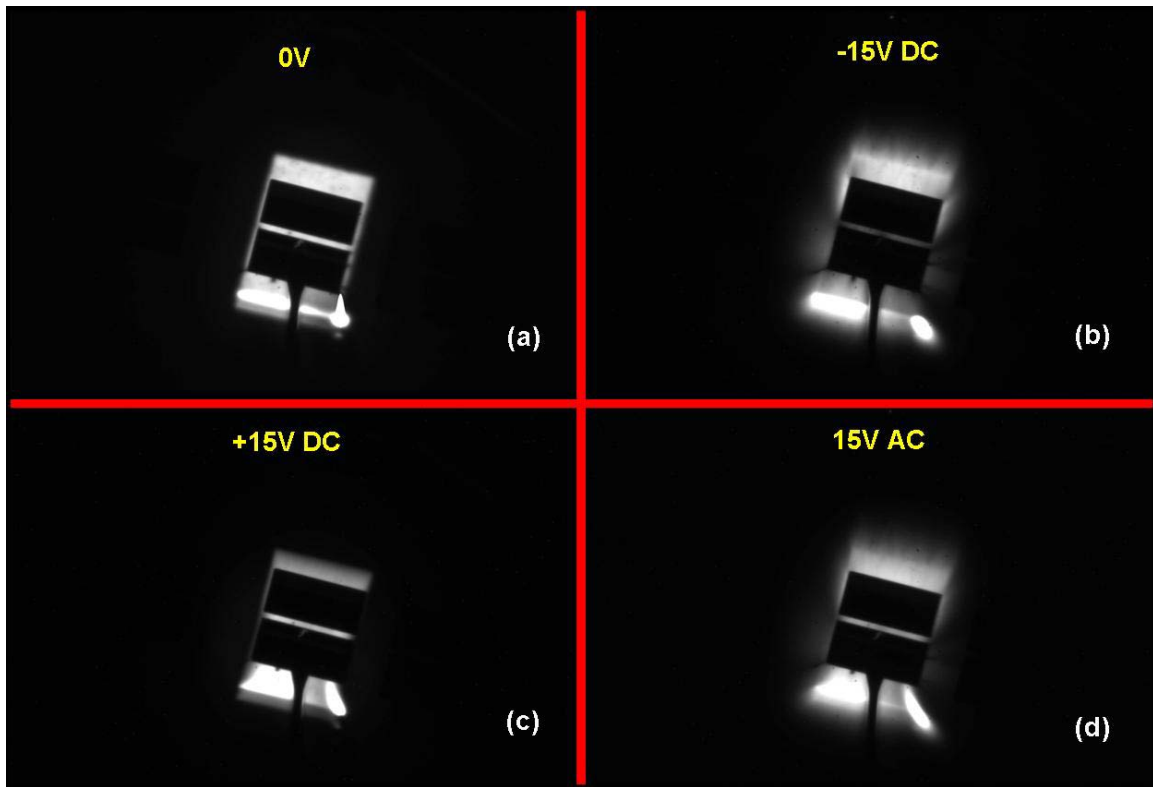


Figure 73. Various cases of direction of diffusion length according to the applied voltage (each image is $874 \mu\text{m} \times 589 \mu\text{m}$).

In part (a) of the figure no voltage is applied. In part (b) -15 V DC bias has been applied to the contact. Minority carriers drift opposite to the negatively charged contact. In part (c) +15 V DC has been applied. In this case, minority carriers drift towards the positively charged plate. Finally, in part (d) of the figure, 15 V AC has been applied. This causes minority carriers to drift towards and away from the plate according to the sign (+ or -) of the instantaneous voltage.

Finally, by operating SEM in spot mode, case 5 (paragraph A-5), is used to visualize the E-field vector and to illustrate the differences between the DC and AC imaging process.

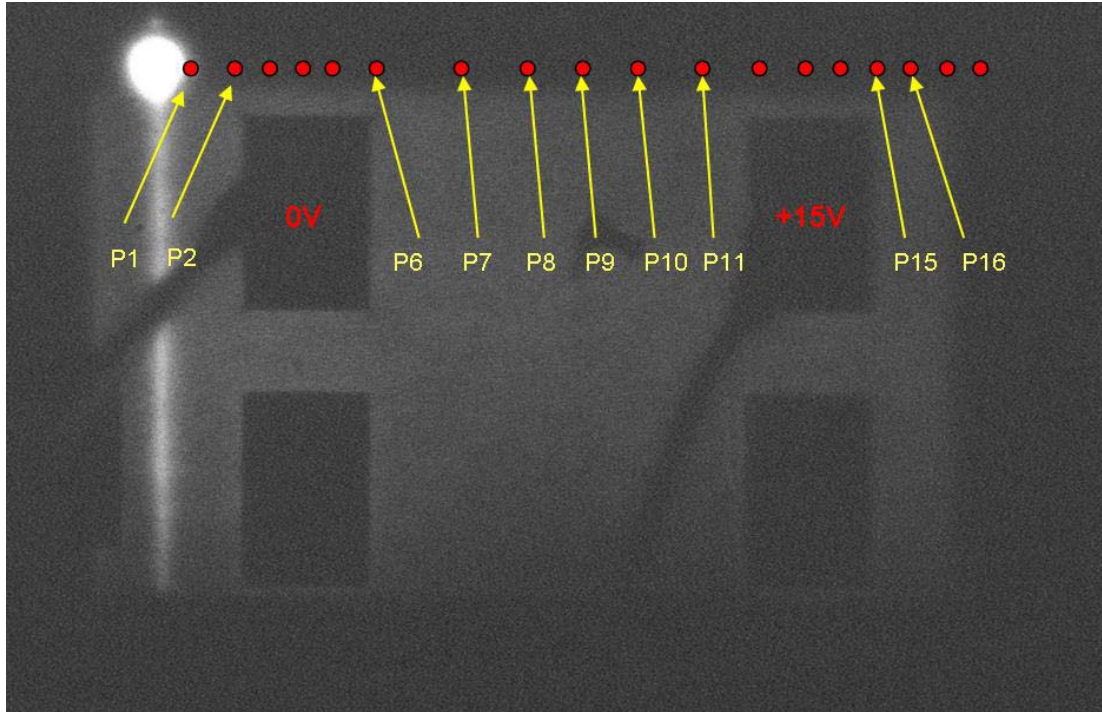


Figure 74. Various positions of electron beam (spot mode) in Sample #9 (874 μm X 589 μm).

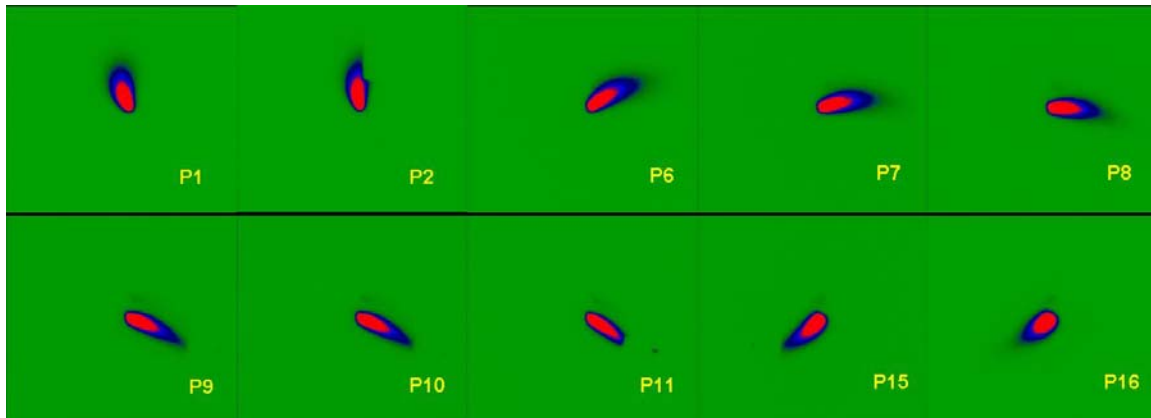


Figure 75. Direction of the electric field in case 5 based on the positions specified in Figure 74 for DC bias (each image is 266 μm X 239 μm).

In Figure 75, images of the charge motion for varying directions of the electric field are shown based on the generation spots of the electron beam as specified in Figure 74. Sample #9 is a p-type semiconductor, so the minority

carriers are electrons. The consecutive images in Figure 75 represent the drift motion of minority carriers (electrons) and this can be seen clearly from the direction of the electric field based on the contacts; electrons follow the electric field lines created from the potential difference between the two contacts.

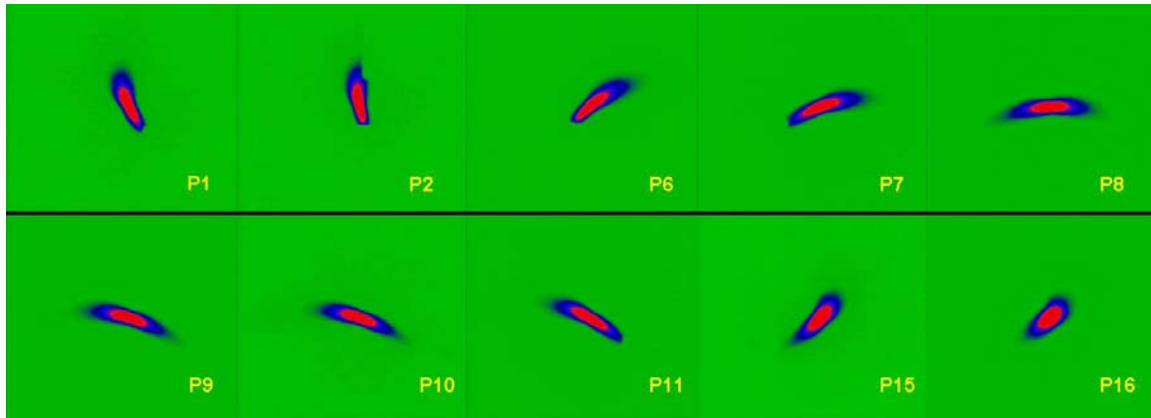


Figure 76. Direction of the electric field in case 5 based on the positions specified in Figure 74 for AC bias (each image is 266 μm X 239 μm).

In Figure 76, the same imaging technique has been adopted with the difference that AC bias has been applied as in the second part of case 5. The AC bias creates a symmetry in the drift behavior but again the drift is towards the positive contact as the polarity oscillates.

Based on the analysis that has been done in the current chapter it can be seen that the charge imaging technique is a powerful “tool” to map electric fields with high resolution. By imaging the motion of the minority carriers (electrons) as a function of applied electric field in a variety of planar contact geometries, both the magnitude and the direction of the electric field vector can be defined with high accuracy.

C. COMSOL MULTIPHYSICS

COMSOL MULTIPHYSICS is a finite element analysis and solver software package for various physics and engineering applications, especially coupled phenomena or multiphysics. COMSOL MULTIPHYSICS also offers an extensive and well-managed interface to MATLAB and its toolboxes for a large variety of

programming, preprocessing and postprocessing possibilities. A similar interface is offered to COMSOL Script. The packages can be used with every operating system (MS Windows, Mac, Linux, Unix). In addition to conventional physics-based user-interfaces, COMSOL MULTIPHYSICS also allows for entering coupled systems of partial differential equations [11].

For the purposes of the current thesis, the Electromagnetics Module of Version 3.2b and the AC/DC Module of Version 3.3 have been used. All the semiconductor planar structures (portions of Sample #9) used have been designed with the CAD capability of the software. This particular module solves problems in the general areas of electrostatic fields, magnetostatic fields, and quasi-static fields. The equations for electromagnetics are automatically available in all of the application modes, making simultaneously the nonstandard modeling easily accessible. The electrostatics (generalized) part of the AC/DC Module used simulates electric fields and currents in dielectric and conductive materials [11].

Finally, all the simulations of the electric fields in COMSOL have been done in 2D. The modeling in 2D usually represents some 3D geometry under the assumption that nothing changes in the third dimension. In order to use the 2D cross-section view of a problem, there are two approaches: the first is when it is assumed that there is no variation of the solution in one particular dimension. The second is when the influence of the finite extension in the third dimension can be neglected. For this reason, in the simulations demonstrated in the next chapter, even though the 2D geometry is used, there are calculations of the z-component of the electric field [11].

THIS PAGE INTENTIONALLY LEFT BLANK

V. APPLICATIONS OF THE TRANSPORT IMAGING TECHNIQUE

A. CONTACT RESISTANCE MEASUREMENTS

When a voltage is applied via contacts to a semiconductor structure, there is some voltage drop associated with the semiconductor-metal interface. The magnitude of this voltage reduction depends on the quality and nature of the contact's material. A standard approach for determining the contact resistance is a 4-point measurement. The disadvantage of the method is the necessity to use two current carrying probes and two voltage measuring probes.

Transport imaging offers a direct way to evaluate the voltage drop at the contacts with a 2-point measurement. The advantage of the method is that no additional processing is required. Since the structure of Sample #9 is based on Schottky diode contact formation, deviations from the ohmic behavior are expected. For this reason, diode I-V characteristics are going to be explored in the current chapter.

1. Case 1

For this case the configuration is shown in Figure 77.

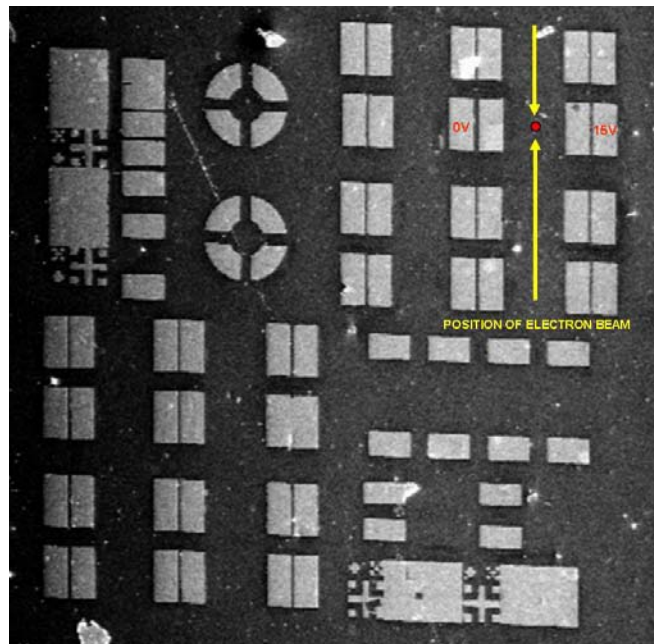


Figure 77. Configuration of Sample #9 for defining the contact resistance with 2-point measurement (2090 μm X 2031 μm).

In Figure 77, 15 V DC has been applied to the outer plates and the distance between the inner plates (edge to edge) is 185 μm . The electron beam is represented with the red circle (not to scale). More specifically, the area of interest is illustrated in Figure 78 by using the COMSOL software.

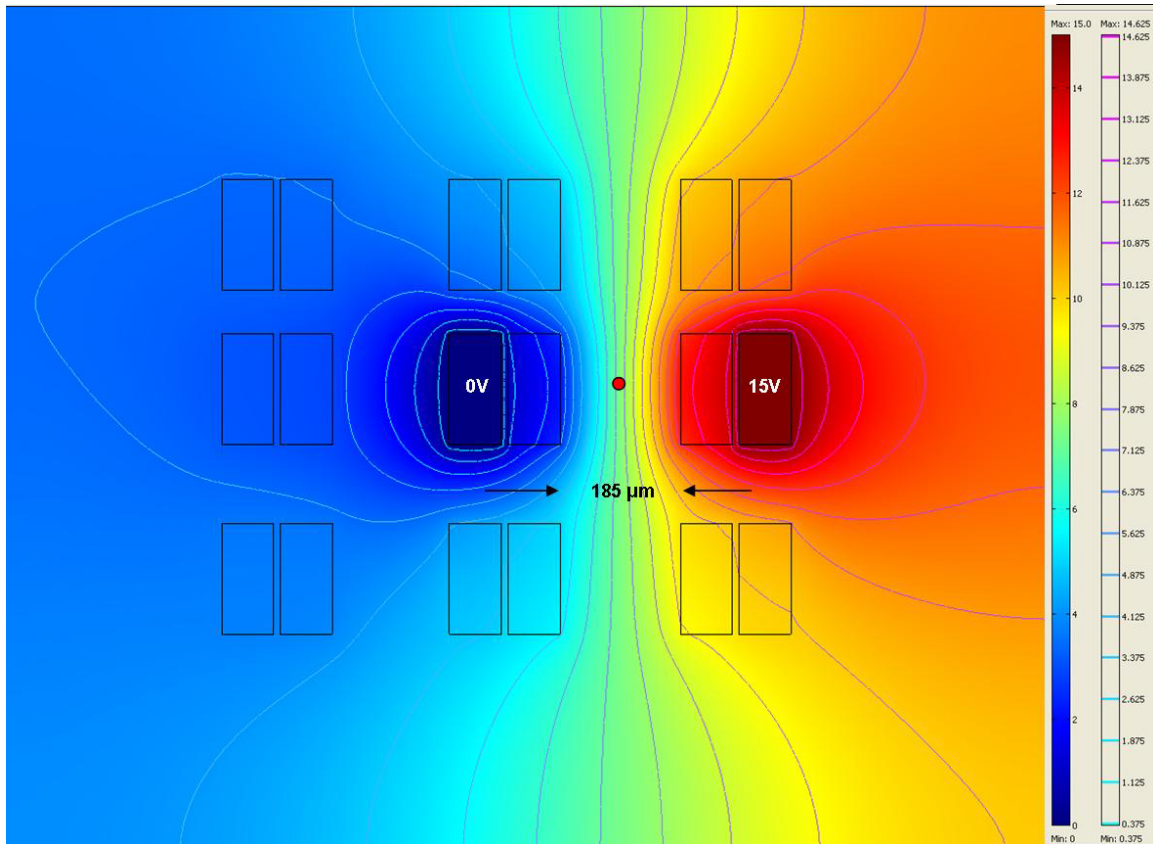


Figure 78. COMSOL simulation of the electric field potential for Case 1.

In Figure 78, the electric potential is represented with color variations defined in the corresponding scale in the right part of the figure above. The contour lines represent equipotential lines. The red circle shows the position of the electron beam (not to scale). The x, y and z components of the generated electric field between the metal contacts which are superjacent to the semiconductor material (Schottky junction), can be seen in the following Figures 79, 80 and 81.

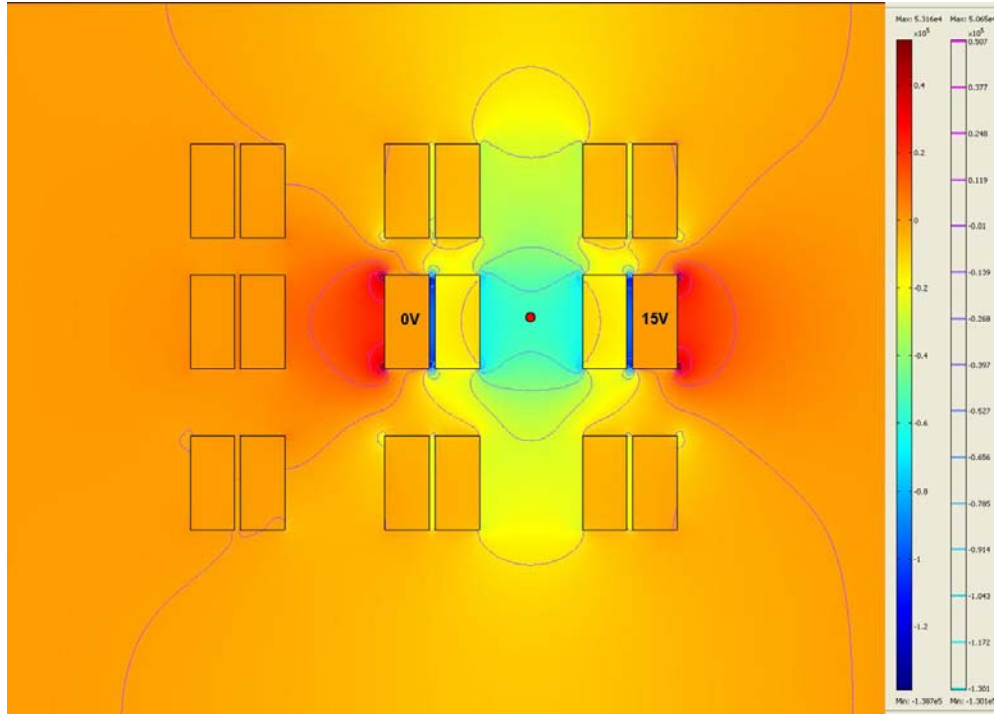


Figure 79. COMSOL simulation of the electric field (x-component) for Case 1.

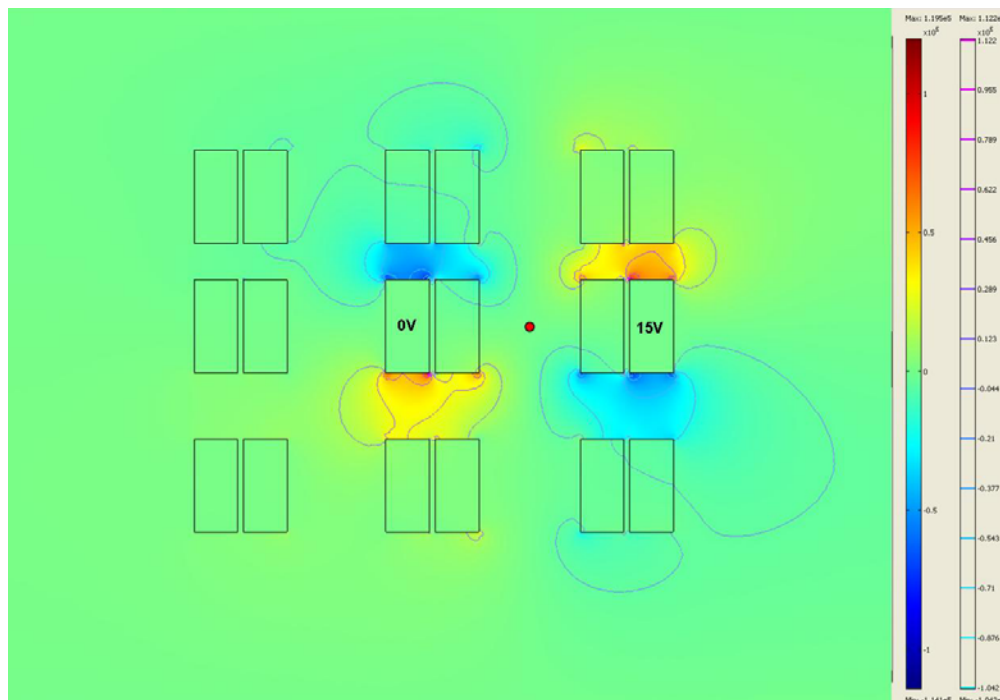


Figure 80. COMSOL simulation of the electric field (y-component) for Case 1.

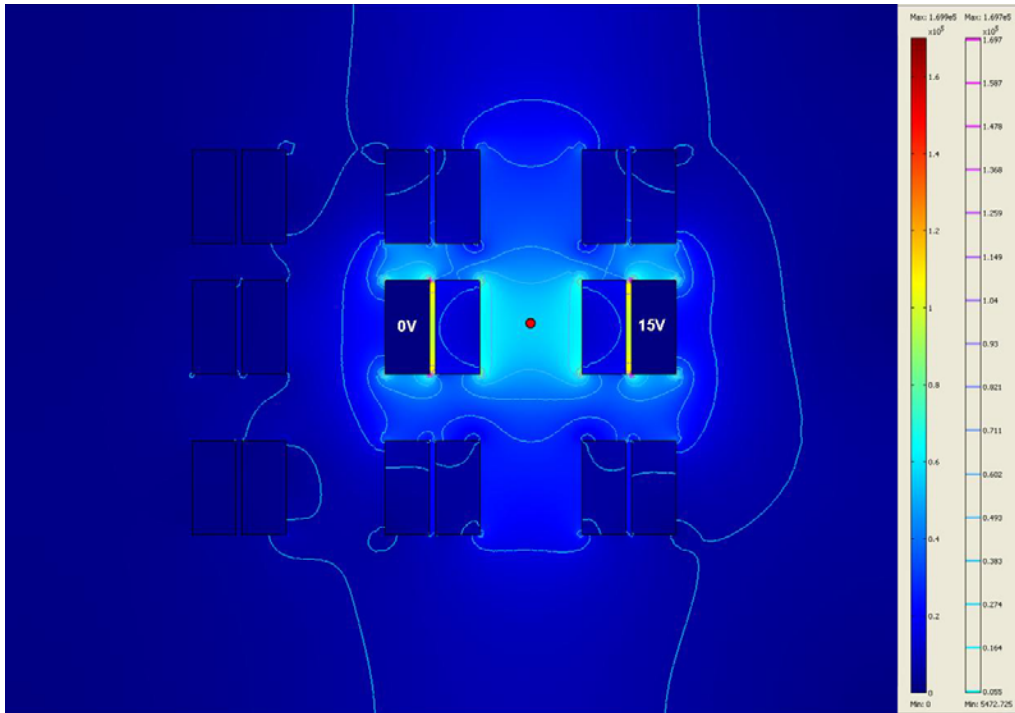


Figure 81. COMSOL simulation of the electric field (z-component) for Case 1.

It should be noted again that even though the model used in COMSOL was based on a 2D geometry, the z component has the physical meaning that the magnitude of the electric field in the z-direction is constant so the direction of the field is tangent to the x-y plane. The generated graphs for the electric field, along the center line between the inner plates, in each direction can be seen in Figures 82, 83 and 84 below. The procedure used in order to generate the following graphs is:

- In COMSOL, a perpendicular line is plotted between the inner plates, passing through the position of the electron beam.
- COMSOL automatically generates a graph.
- Extract the data in a “.txt” file.
- Import the data into a MATLAB code (Appendix C) and generate the corresponding plots.

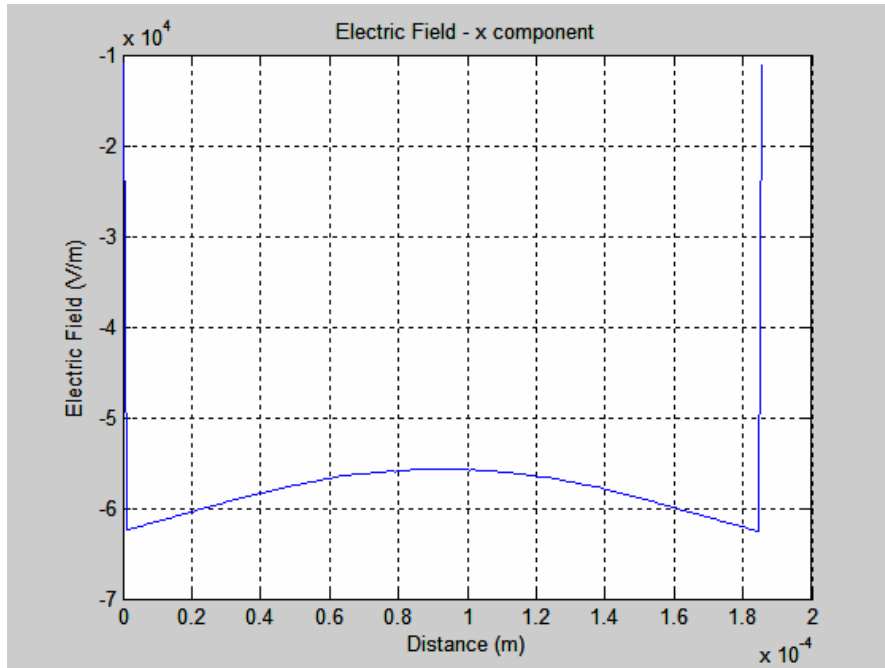


Figure 82. Electric field (x-component) for Case 1.

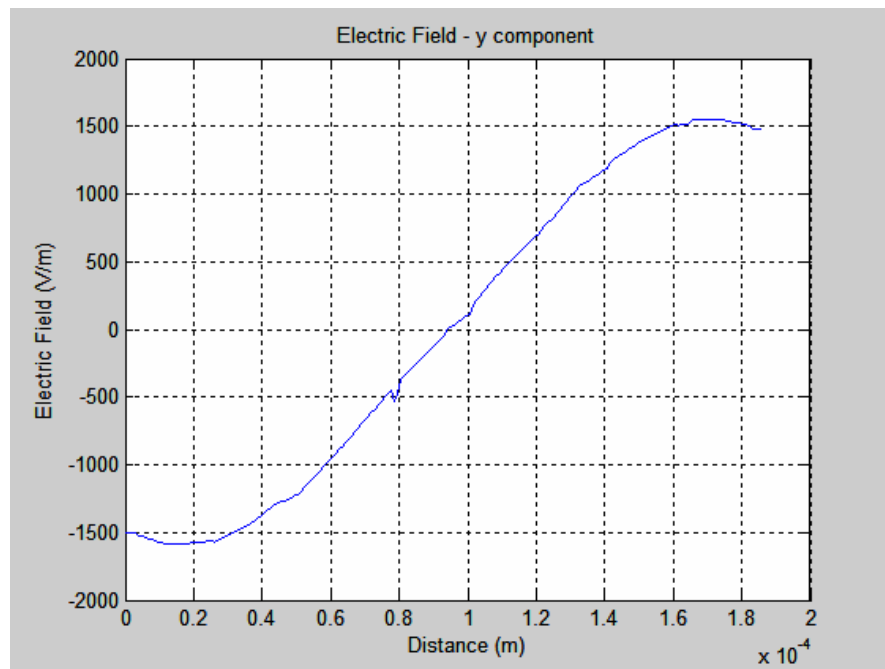


Figure 83. Electric field (y-component) for Case 1.

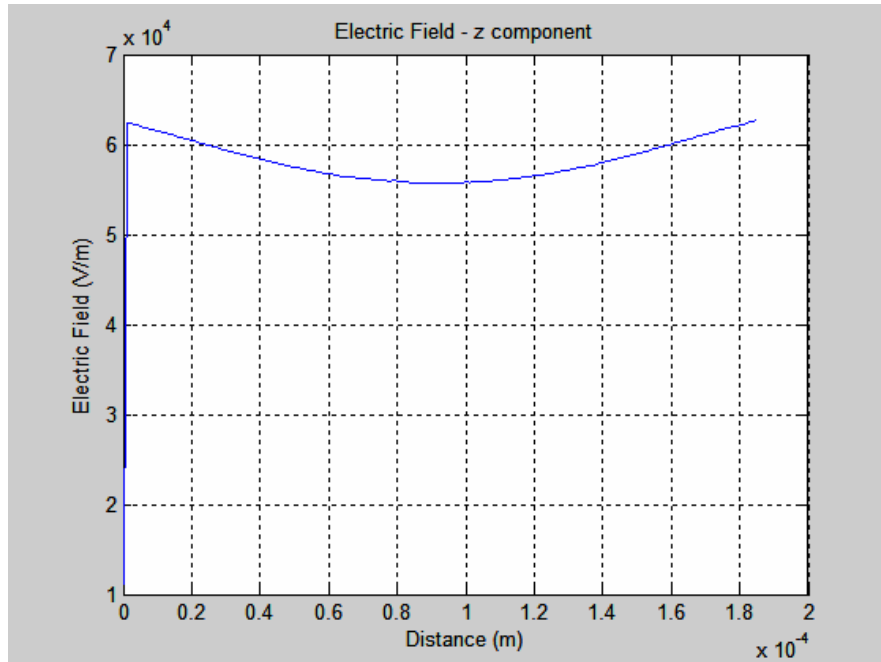


Figure 84. Electric field (z-component) for Case 1.

In Figure 85, the total electric field from the simulation is presented. It can be seen that there is a perfect symmetry in the graph and this is exactly as expected since the model assumes completely uniform material and contact parameters.

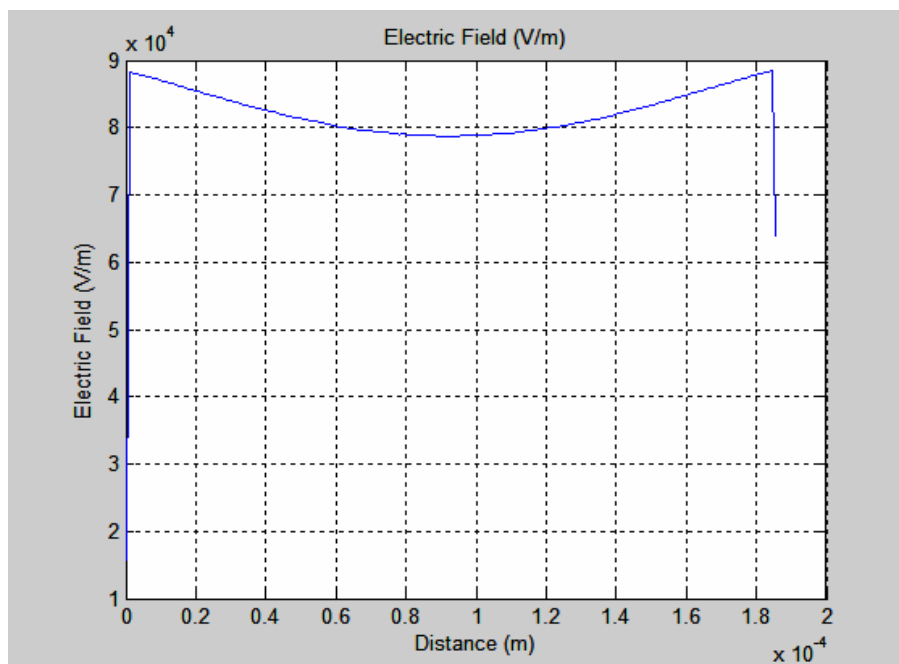


Figure 85. Total electric field for Case 1.

By determining the value of the electric field in the middle of the distance between the plates (i.e., $185/2=92.5 \mu\text{m}$), in each direction, the resultant value is:

$$E_x = -5.57 \times 10^4 \frac{V}{m}, \quad E_y = -64.8 \frac{V}{m}, \quad E_z = 5.56 \times 10^4 \frac{V}{m} \quad \text{and}$$

$$E = \sqrt{E_x^2 + E_y^2 + E_z^2} = 78.7 \times 10^3 \frac{V}{m} \quad (\text{exactly as seen in Figure 85}).$$

In order to define the effective distance between the plates:

$$d = \frac{\text{applied voltage}}{\text{electric field}} = \frac{15V}{78.7 \times 10^3 \frac{V}{m}} = 191 \mu\text{m}$$

It is important to note that the effective distance is smaller in magnitude from the real distance between the plates where the voltage is applied.

Then, using Sample #9, in the configuration of Figure 77, the electron beam is applied to a specific point on the surface of the semiconductor material. A series of images of the intensity are taken (one with zero and one with applied voltage), incrementing the applied voltage each time in 0.5 V step. By evaluating the intensity ratio of the peak values as described in previous sections to determine the local magnitude of the electric field at the point of charge generation, the resultant values are obtained (Figures 86 and 87).

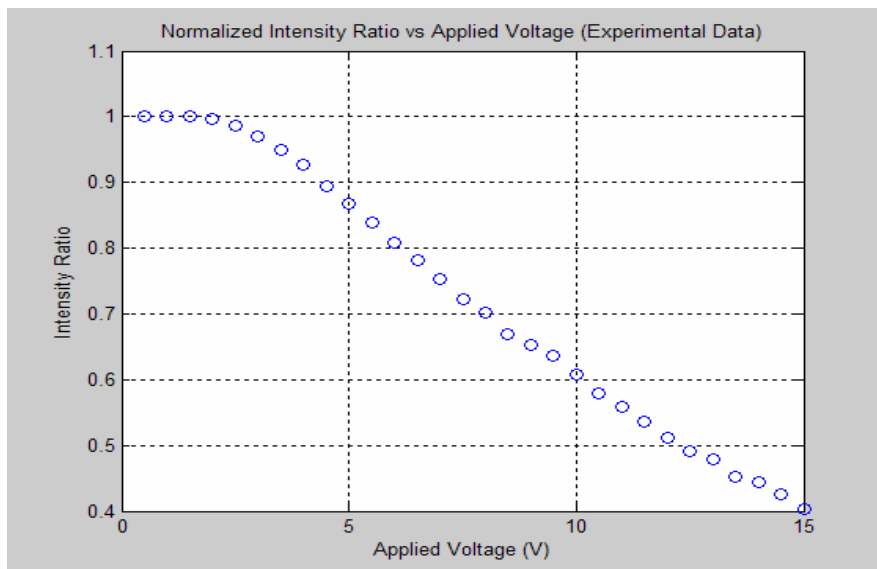


Figure 86. Intensity ratio vs. applied voltage for Case 1.

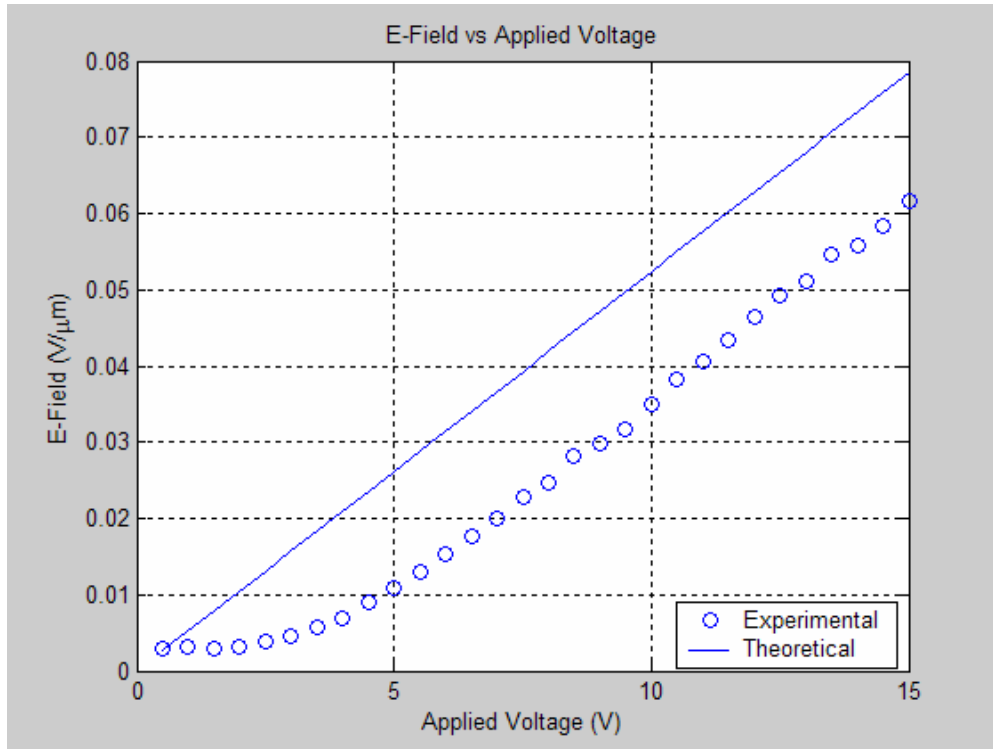


Figure 87. Electric field vs. applied voltage for Case 1.

From Figure 87 it can be seen clearly that, as expected, the actual-experimental values of the electric field (circles) in the semiconductor material are smaller than the theoretical values (solid line) which are derived from the division of the applied voltage over the effective distance between the plates. The difference can be taken as a measure of the voltage drop at the contacts. From Figure 87 it can be seen that the “turn on” voltage of the forward biased Schottky contact is at $\approx 2\text{-}3$ V DC bias. Below that voltage, very little applied field exists in the center region of the device.

2. Case 2

For this case the configuration is shown in Figure 88. 15 V DC has been applied between the inner plates whose distance is $185\ \mu\text{m}$. The area of interest is illustrated in Figure 89 where a plot of electric potential has been created by the use of COMSOL software. The color interpretation is given in the color scale shown at the right of Figure 89. The contour lines represent the equipotential areas. The red circle shows the position of the electron beam (not to scale).

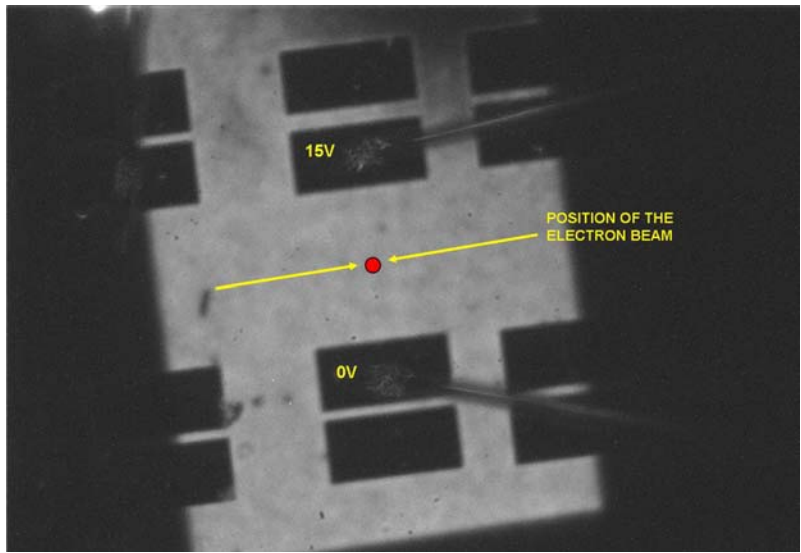


Figure 88. Configuration of Sample #9 for defining the drop of voltage between the contacts with 2-point measurement.

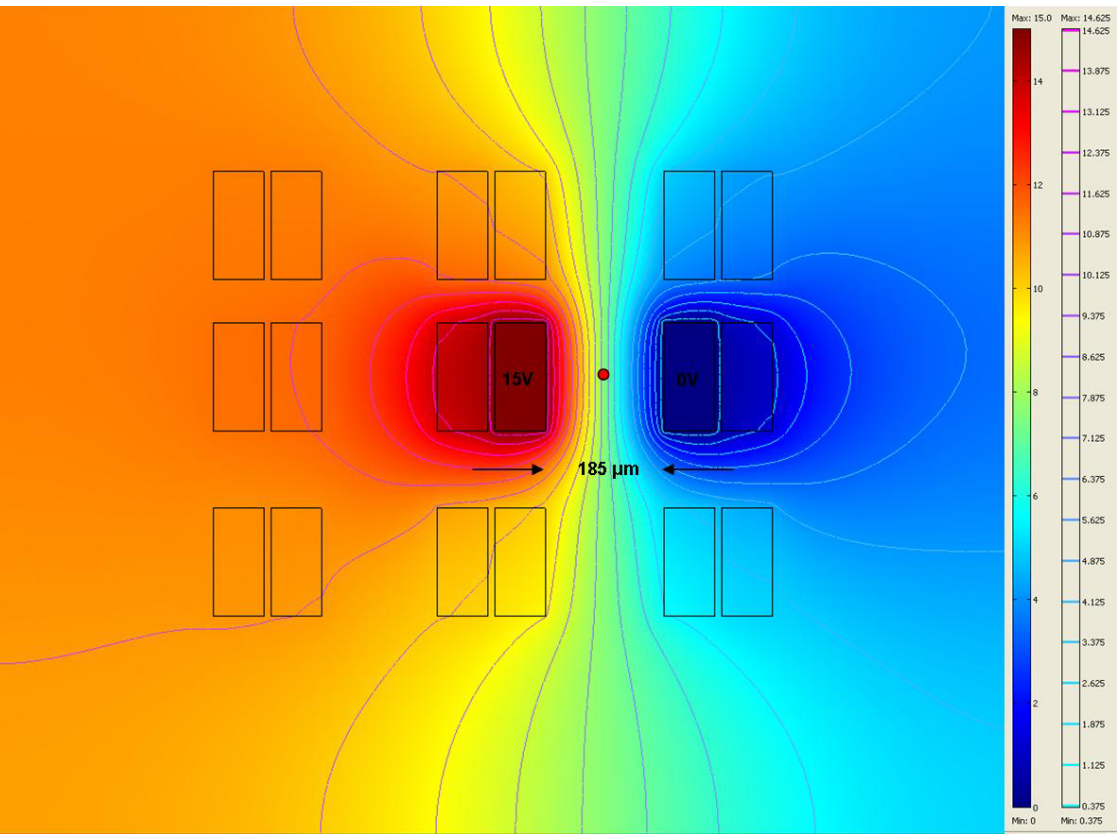


Figure 89. COMSOL simulation of the electric field potential for Case 2.

The x, y and z components of the generated electric field between the metal contacts which are superjacent to the semiconductor material, can be seen in Figures 90, 91 and 92.

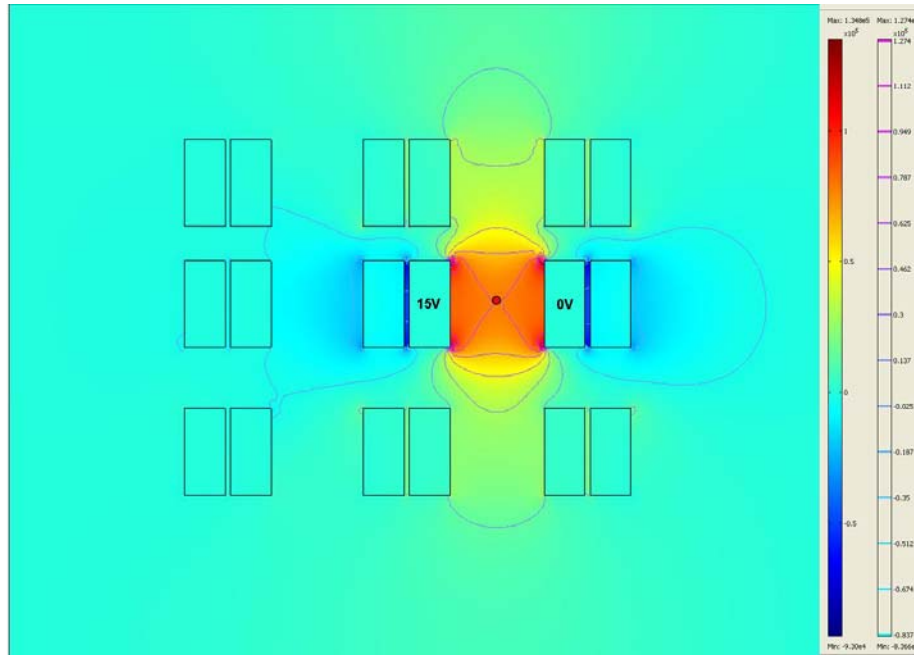


Figure 90. COMSOL simulation of the electric field (x-component) for Case 2.

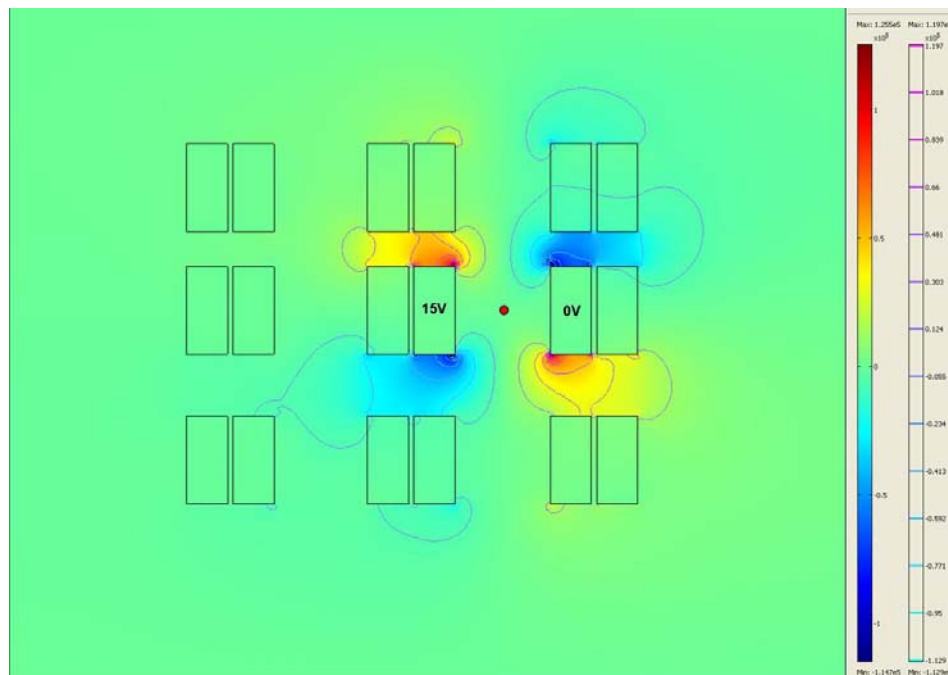


Figure 91. COMSOL simulation of the electric field (y-component) for Case 2.

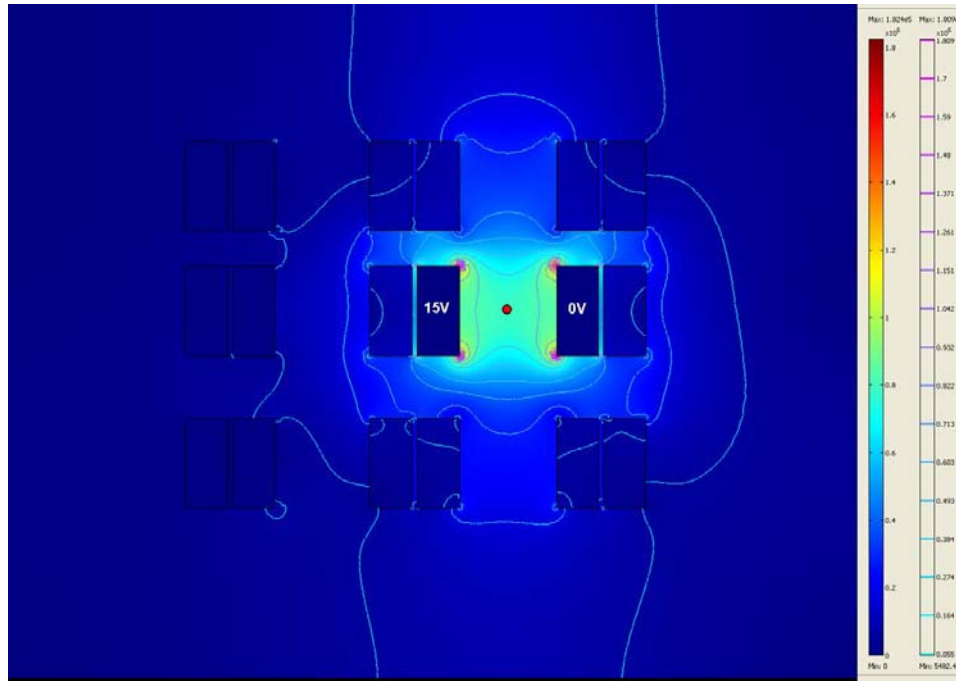


Figure 92. COMSOL simulation of the electric field (z-component) for Case 2.

By extracting the data of Figures 90 through 92 in the MATLAB code of Appendix C, graphs of the electric field across a line perpendicular to the inner plates that passes through the position of the electron beam (red circle) can be seen in Figures 93, 94 and 95.

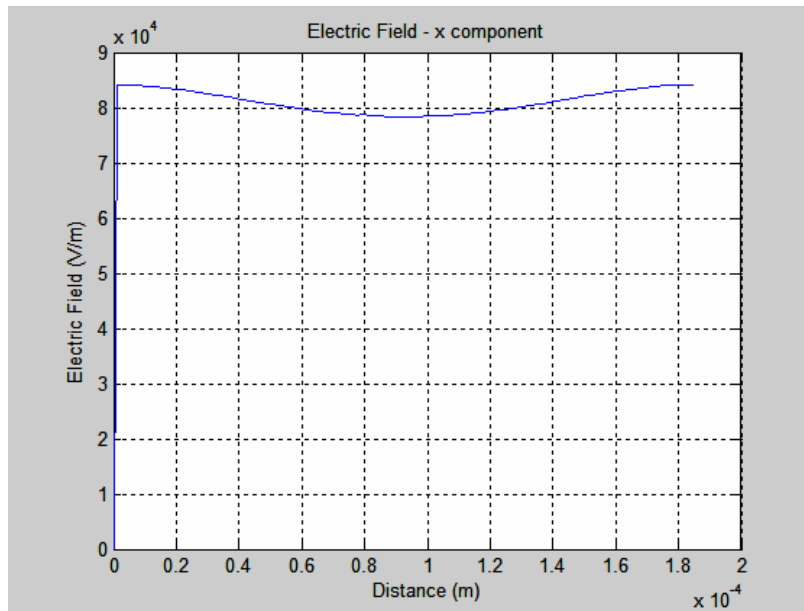


Figure 93. Electric field (x-component) for Case 2.

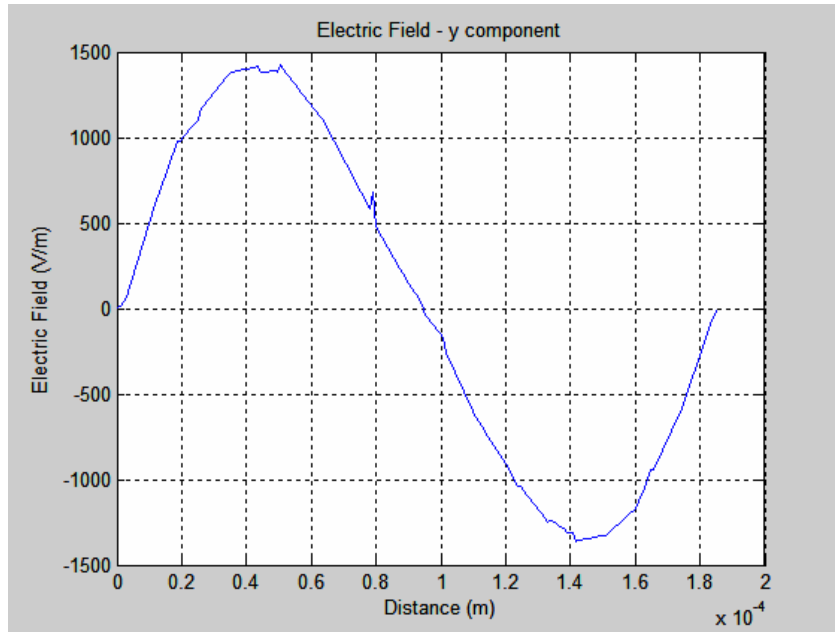


Figure 94. Electric field (y-component) for Case 2.

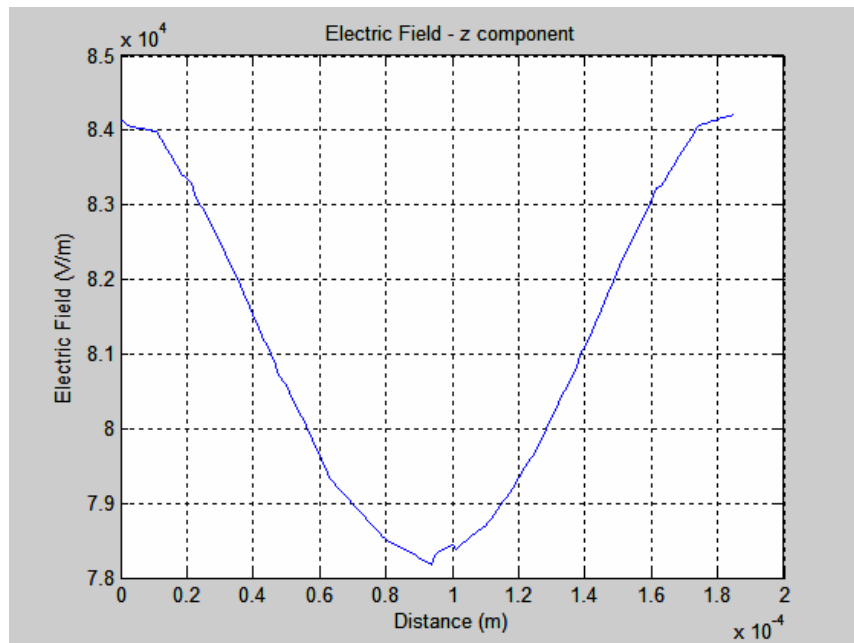


Figure 95. Electric field (z-component) for Case 2.

The total electric field can be seen in Figure 96.

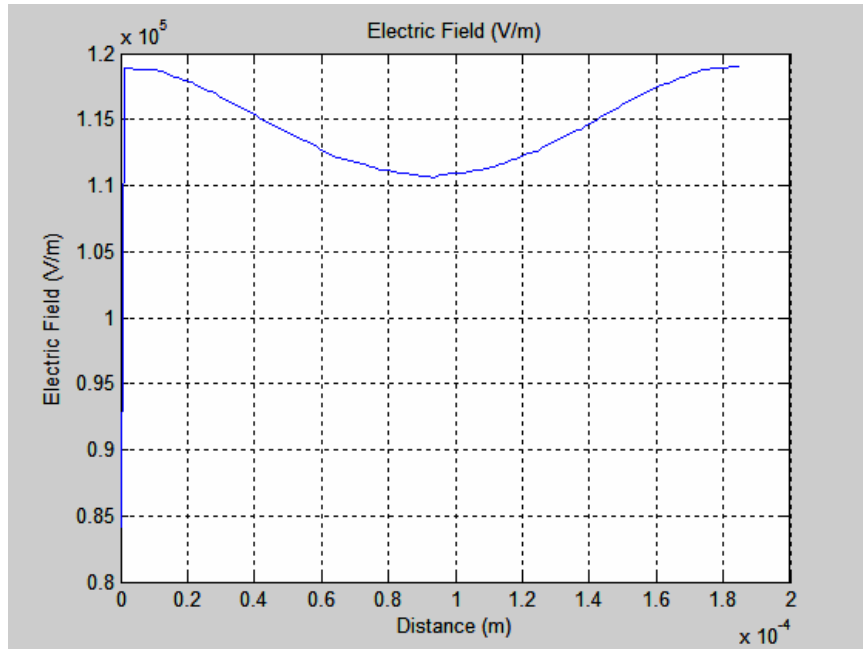


Figure 96. Total electric field for Case 2.

By determining the value of the electric field in the middle of the distance between the plates (i.e., $185/2=92.5 \mu\text{m}$), in each direction, the resultant value is:

$$E_x = 7.827 \times 10^4 \frac{V}{m}, \quad E_y = 74 \frac{V}{m}, \quad E_z = 7.821 \times 10^4 \frac{V}{m} \quad \text{and}$$

$$E = \sqrt{E_x^2 + E_y^2 + E_z^2} = 111 \times 10^3 \frac{V}{m} \quad (\text{exactly as seen in Figure 85}).$$

In order to define the effective distance between the plates:

$$d = \frac{\text{applied voltage}}{\text{electric field}} = \frac{15V}{111 \times 10^3 \frac{V}{m}} = 136 \mu\text{m}$$

Again it should be noted that the effective distance is smaller in magnitude from the real distance between the plates where the voltage is applied.

Next, by using the specimen (Sample #9), in the configuration of Figure 88, the electron beam is applied to a specific point on the surface of the semiconductor material. A series of images of the intensity are taken (one with zero and one with applied voltage), incrementing the applied voltage each time in

0.5 V step. By evaluating the intensity ratio of the peak values as described in previous sections to determine the local magnitude of the electric field at the point of charge generation, the resultant values are obtained (Figures 97, 98 and 99).

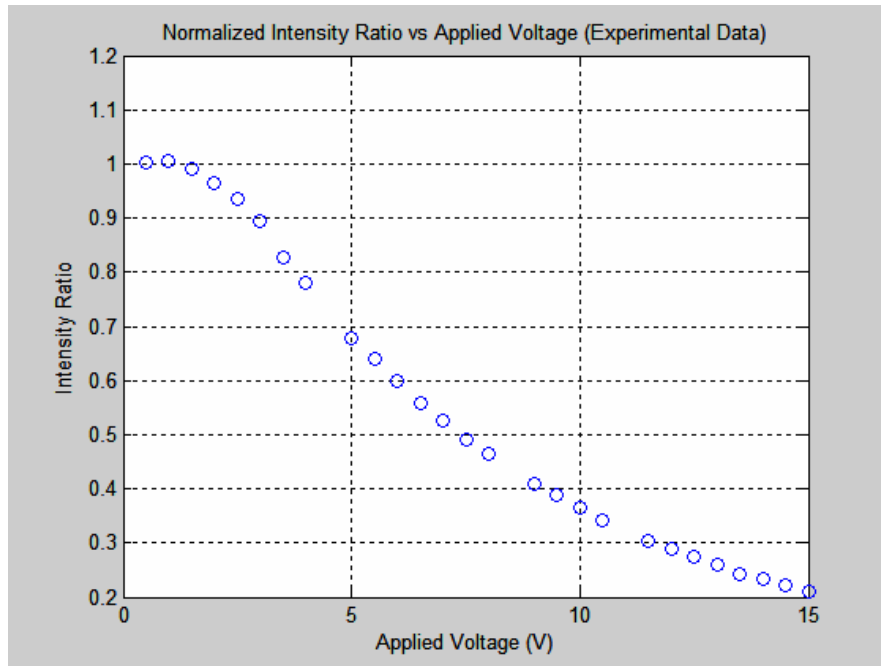


Figure 97. Intensity ratio vs. applied voltage for Case 2.

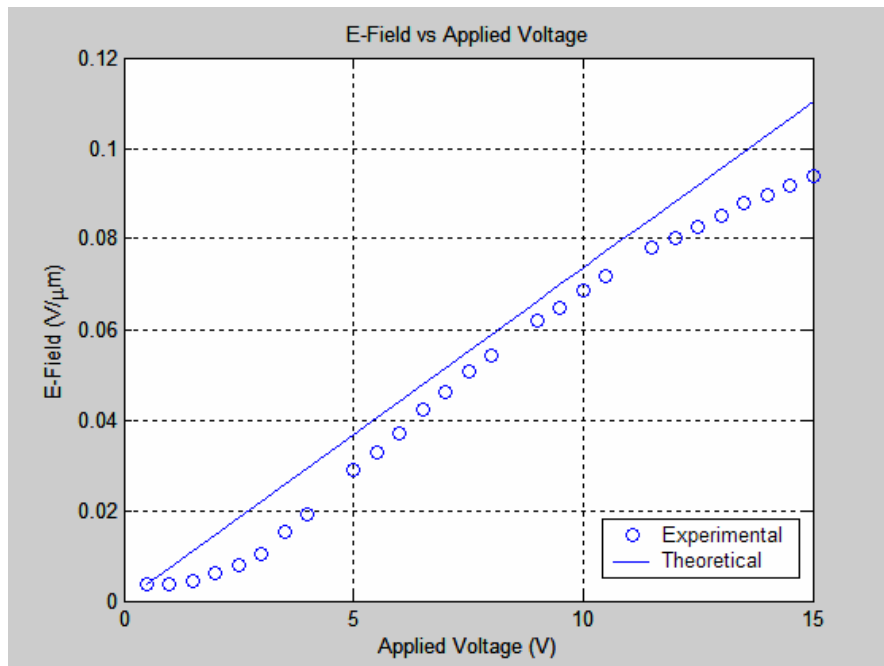


Figure 98. Electric field vs. applied voltage for Case 2.

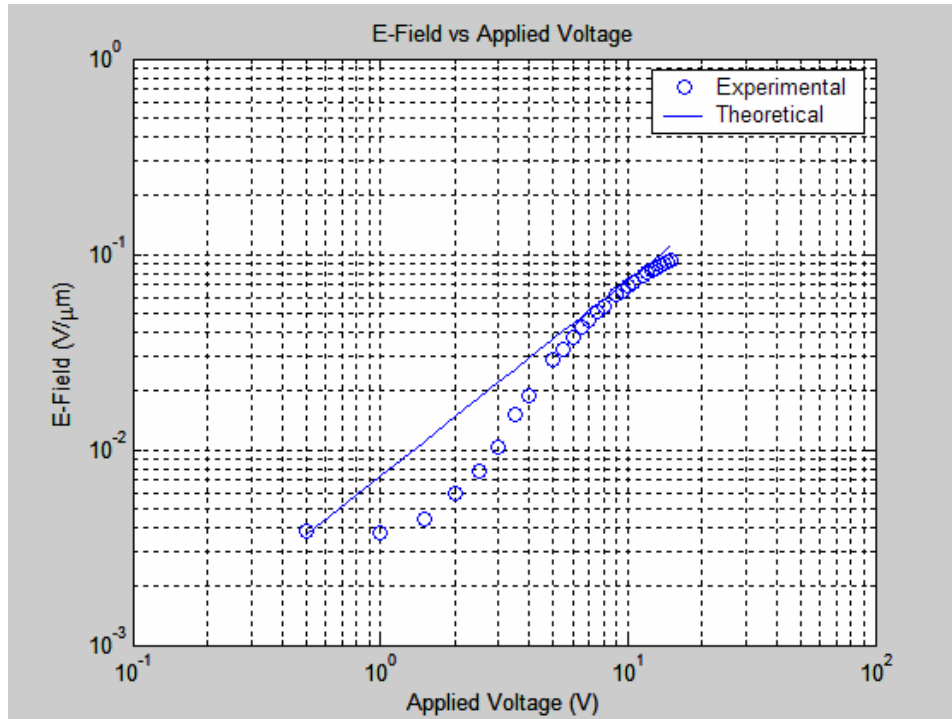


Figure 99. Electric field vs. applied voltage for Case 2 (log-log scale).

Similarly to Case 1 of the current chapter, the experimental values are lower in magnitude than the theoretical values and the “turn on” voltage for the forward biased Schottky diode is at about 2 V DC bias.

B. COMPARISON OF ELECTRIC FIELD MAGNITUDE DETERMINED EXPERIMENTALLY TO COMSOL MODELING

In this part of the thesis it is important to evaluate the accuracy of the experimental approach of determining locally the magnitude of the electric field in a planar semiconductor structure, as explained in Chapter IV. One way to do so is by comparing the results with a simulation of an idealized structure. The latter can be efficiently simulated by the use of COMSOL software.

The case study is illustrated in Figure 100 below (this case has been analyzed in Chapter IV, paragraph A-2). 15 V DC has been applied between the contacts and 36 images taken at positions determined with the red circles. In addition, by using COMSOL, the electric field across a line starting from position 1 (P1) and ending at position 36 (P36) has been evaluated. The resultant comparison is shown in Figure 101.

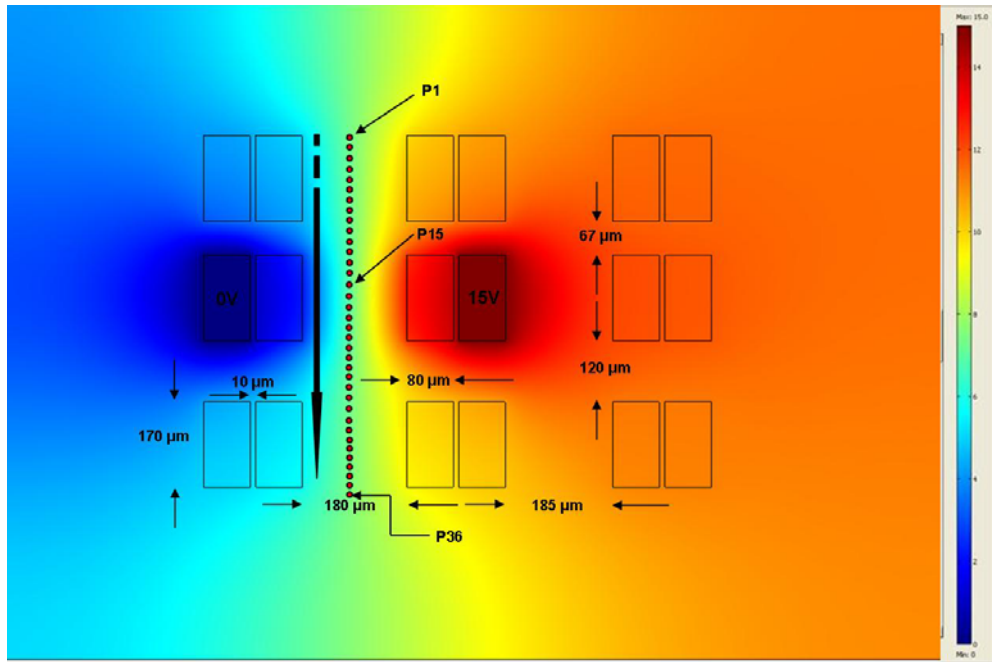


Figure 100. Part of Sample #9 for comparison of the COMSOL simulation with the experimental method.

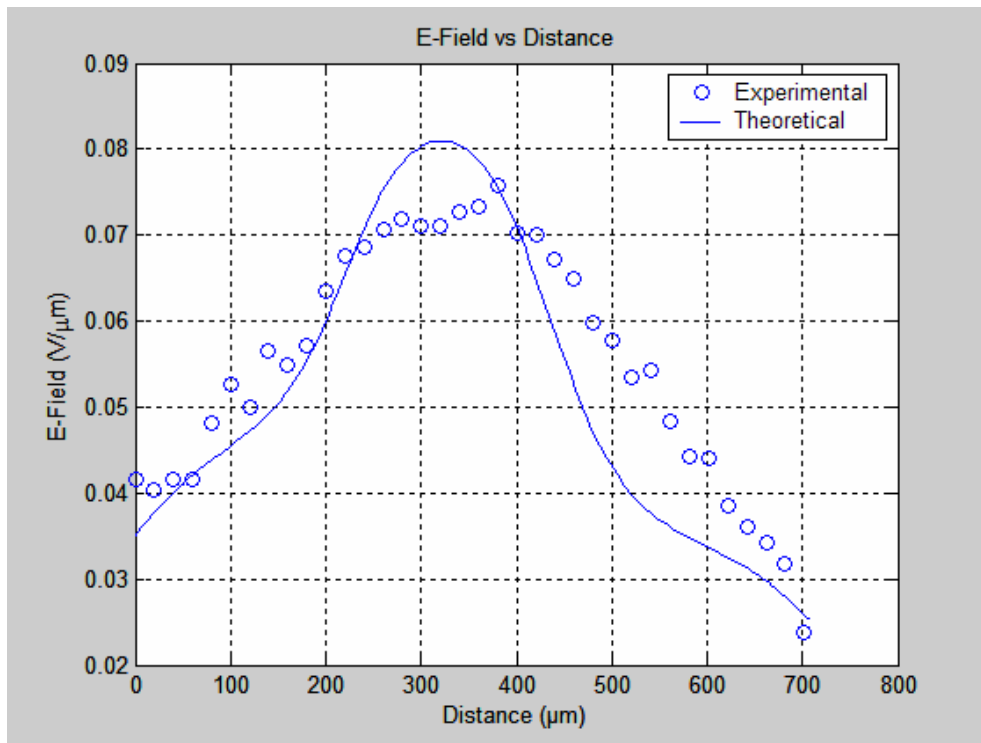


Figure 101. Comparison of the electric field as a function of position for 15 V DC applied bias.

From Figure 101 it can be seen that the experimental method used in the current work is in good conditions with the simulations (about 10%) and it gives reasonable values of the magnitude of the electric field locally based on the real characteristics of the material used. Local defects can also play a significant role in decreasing the field at any given spot and this is something that cannot be simulated in COMSOL. Also it should be noted that the simulation in COMSOL was based on a structure that has contacts made of Copper superjacent to Silicon semiconductor material. The fluctuations that can be observed may be also due to a small difference in the position of the line used for COMSOL calculations and the position of the electron beam during the experimental approach.

C. EVALUATION OF THE ELECTRIC FIELD MAGNITUDE IN SEMICONDUCTOR PLANAR STRUCTURES OF CONSTRICTED GEOMETRY

In order to better demonstrate the potential capabilities of the experimental method for determining the electric field magnitude as described in this thesis, the case illustrated in Figure 102 is explored. The motion of charge from a region of 1 dimensional (1D) confinement to a 2D region is of high interest in preparation for the future study of contacted nanowires.

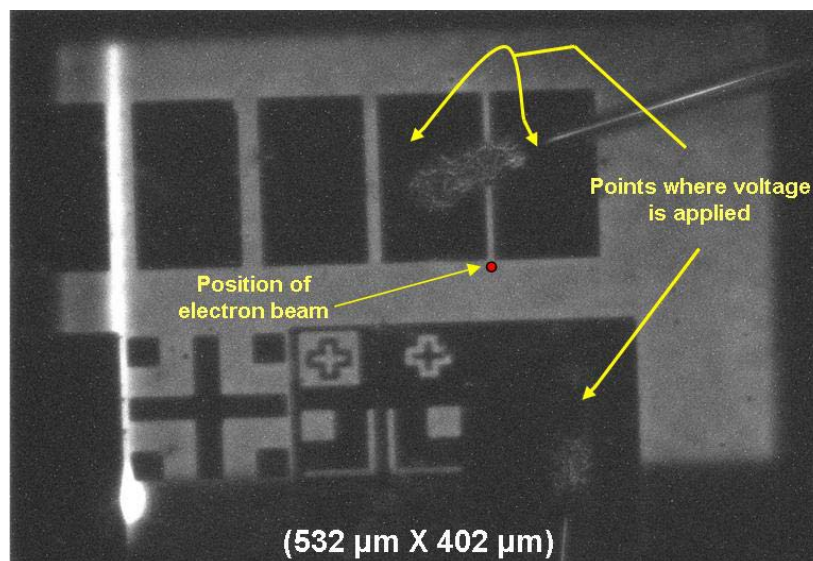


Figure 102. Part of Sample #9 with special geometry characteristics.

In Figure 102 the two upper-right plates have been bridged together and the potential difference is applied at points illustrated with the yellow lines. The electron beam is applied at the point specified with the red circle and three images (Figure 103) are acquired with different applied voltages (zero bias, +7 V DC and -7 V DC). The electron beam energy was 30 keV, the probe current was 6E-10 A and the SEM was operated in spot mode.

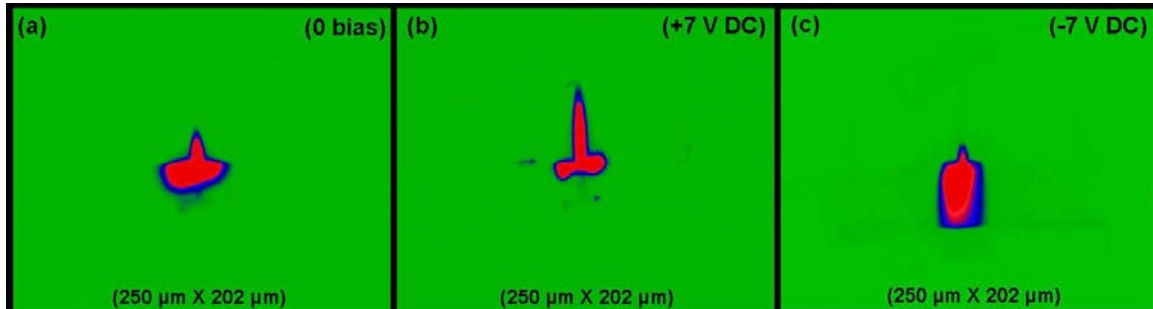


Figure 103. Spot mode images at point of charge generation with zero bias (a), +7 V DC bias (b) and -7 V DC bias (c).

By using the SEM in line mode (Figure 104) a series of images have been acquired as demonstrated in Figures 105 and 106. Figure 105 corresponds to the vertical red line in Figure 104 and Figure 106 to the green horizontal line. The reason for using the line mode is that it gives more general spatial information for the behavior of the electric field in the area of interest.

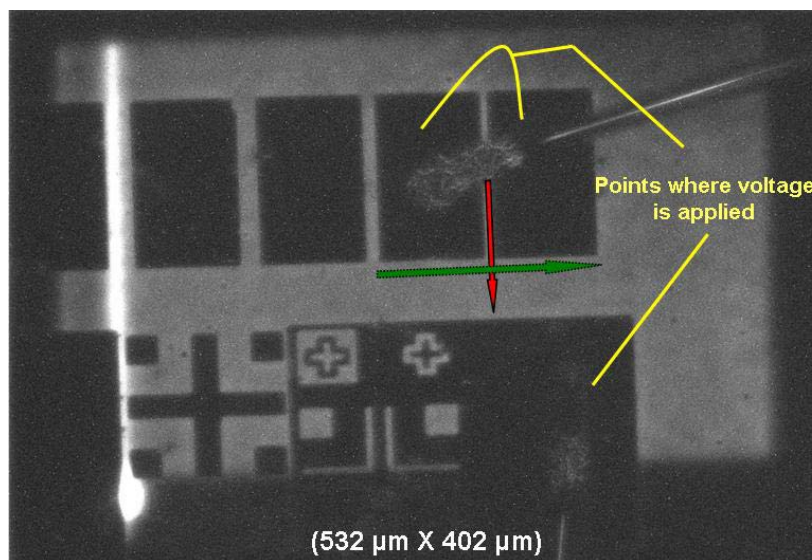


Figure 104. SEM operation in line mode for Sample #9 for the case study.

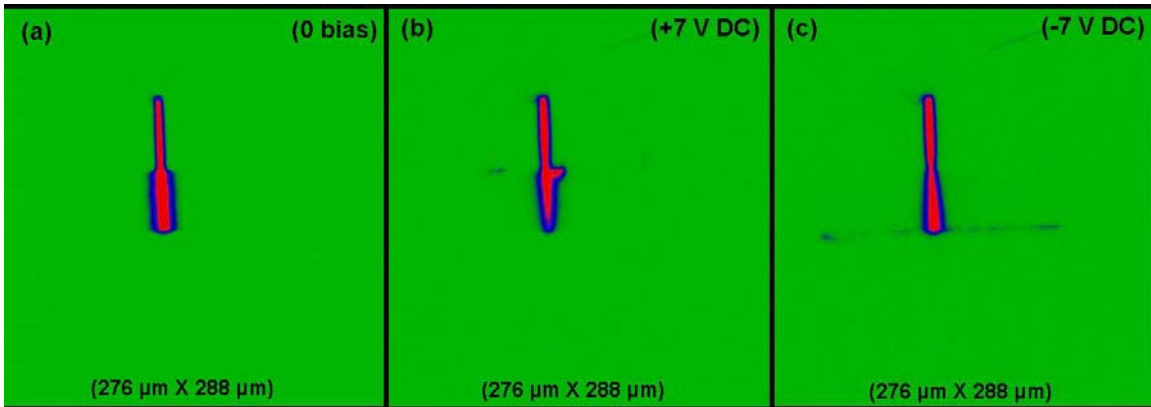


Figure 105. Line mode images (vertical red line) with zero bias (a), +7 V DC bias (b) and -7 V DC bias (c).

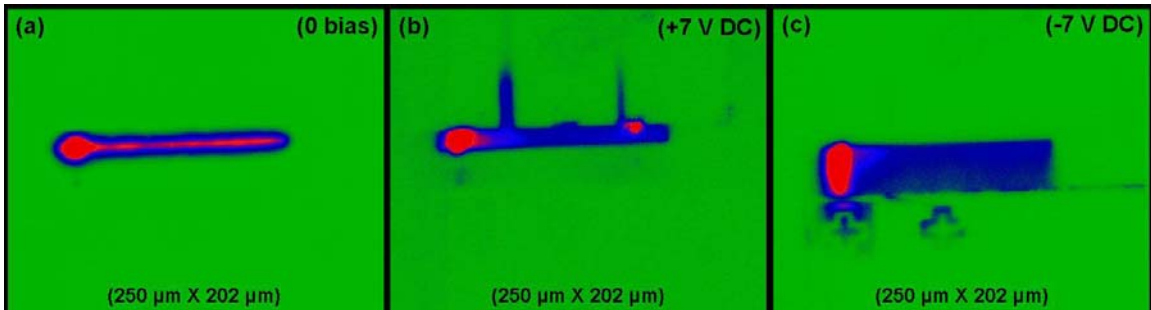


Figure 106. Line mode images (horizontal green line) with zero bias (a), +7 V DC bias (b) and -7 V DC bias (c).

By the above qualitative analysis it has been demonstrated how important a role the geometry plays on the electric field behavior. Based on the polarity of the applied voltage, the field is either forced to “tunnel” through the space between the contacts or diverges in the opposite direction. It is important to note that the distance between the “bridged” contacts is about $4\ \mu\text{m}$ which is almost equal to the diffusion length of the minority carriers.

In order to quantitatively determine the electric field magnitude at specific points, the experimental method described in previous sections is used. The results can be seen in Figures 107 and 108. In addition, in Figure 108 a comparison between the experimental data and a corresponding simulation in COMSOL has been done.

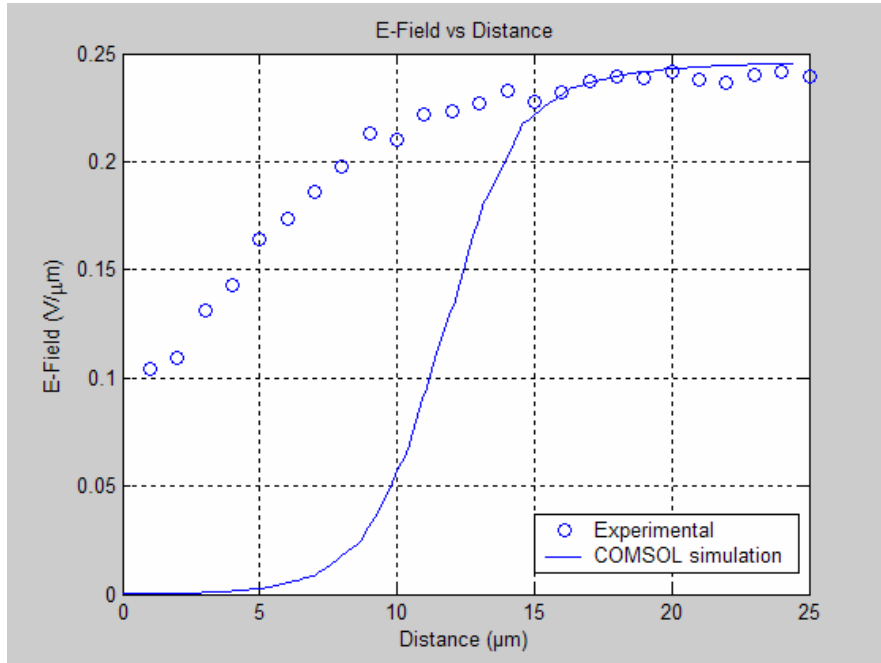


Figure 107. E-Field vs. distance for points along (in the direction shown) of the red vertical line of Figure 104 with -7 V DC applied bias.

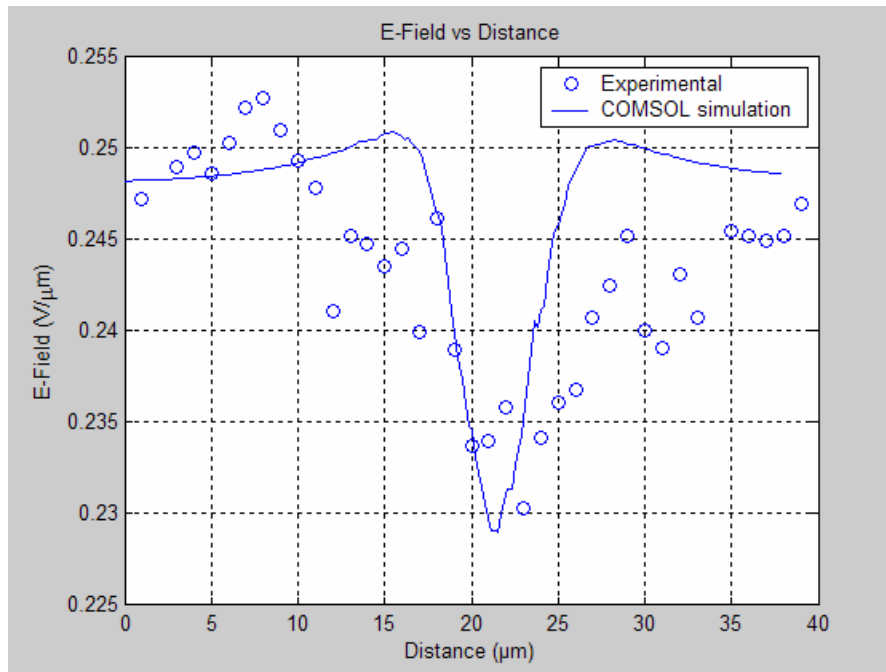


Figure 108. E-Field vs. distance for points along (in the direction shown) of the green horizontal line of Figure 104 with -7 V DC applied bias.

By combining the data of Figure 107 with the qualitative approach demonstrated in Figure 105-(c), it can be seen that the electric field magnitude at points constrained between the two “bridged” contacts is much lower than the values of the field in the “open” area between the points where the bias is applied. In Figure 107 the first 10 field values correspond to points inside the constrained area between the “bridged” contacts and the remaining 15 values correspond to points in the 2D area. The experimental approach shows existence of E-field in places where COMSOL MULTIPHYSICS did not.

For the data of Figure 108, combined with that of Figure 106-(c) it can be seen that the lowest value of the electric field is exactly at the point where the constrained area between the “bridged” contacts is connected with the “open” area. All the above areas are illustrated in Figure 109. The experimental data have also been compared with the results of a simulation made by COMSOL MULTIPHYSICS in a similar semiconductor structure. The trend of the experimental data is consistent with the simulation but the magnitude has been scaled in order to include the effects of fluctuations in contact resistance, an effect that cannot be simulated.

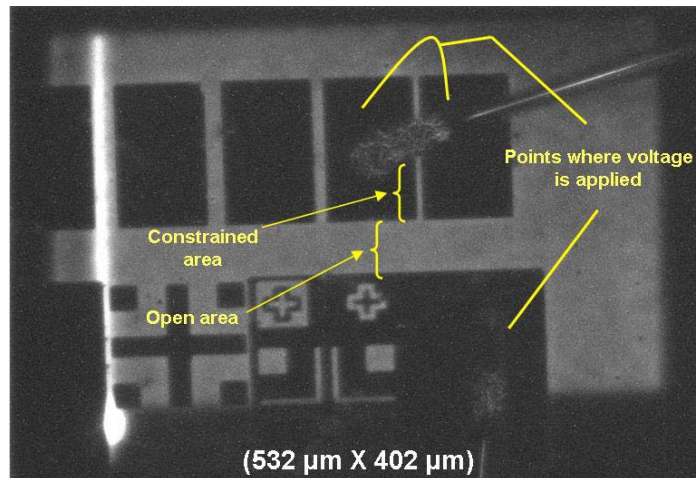


Figure 109. Areas of interest for determination of the electric field behavior.

This last experiment reveals useful details associated with charge injection in confined regions, details that cannot be otherwise measured electrically.

THIS PAGE INTENTIONALLY LEFT BLANK

VI. CONCLUSIONS AND SUGGESTIONS FOR FURTHER RESEARCH

A. SUMMARY AND CONCLUSION

Photonic devices can be divided in the following categories with respect to their principles of operation: Light-emitting diodes (LEDs) and lasers (light amplification by stimulated emission of radiation) convert electrical energy to optical energy. Photodetectors detect optical signals and solar cells convert optical energy into electrical energy. Specifically the operation of photodetectors, which are used extensively in various kinds of optical sensors, is based on carrier generation by incident light, carrier transport and interaction of current with the external circuit to provide the output signal [12]. A wide range of devices depend upon the fabrication of contacts that can uniformly inject and remove charge. The understanding of local transport behavior is essential for the development of new devices in all these areas.

The work described in this thesis is based on cathodoluminescence scanning electron microscopy. A technique for imaging the transport of free charge in planar semiconductor structures has been developed in our laboratory. This technique has been used to image the motion of minority carriers in a heavily doped p-type AlGaAs/GaAs/AlGaAs heterostructure, under a range of applied electric fields. By generating charge at a fixed point, it is possible to monitor the subsequent drift and diffusion by imaging the distribution of the free carrier recombination path as illustrated in Figure 110 below. In this figure, the SEM is operated in spot mode and three images have been acquired, with zero, DC and AC bias in Figures (a), (b) and (c) respectively. In the following 3D graphs, the intensity of light at the point of generation is acquired for each case mentioned above. Additionally, the direction of the drift length due to the applied bias is efficiently illustrated.

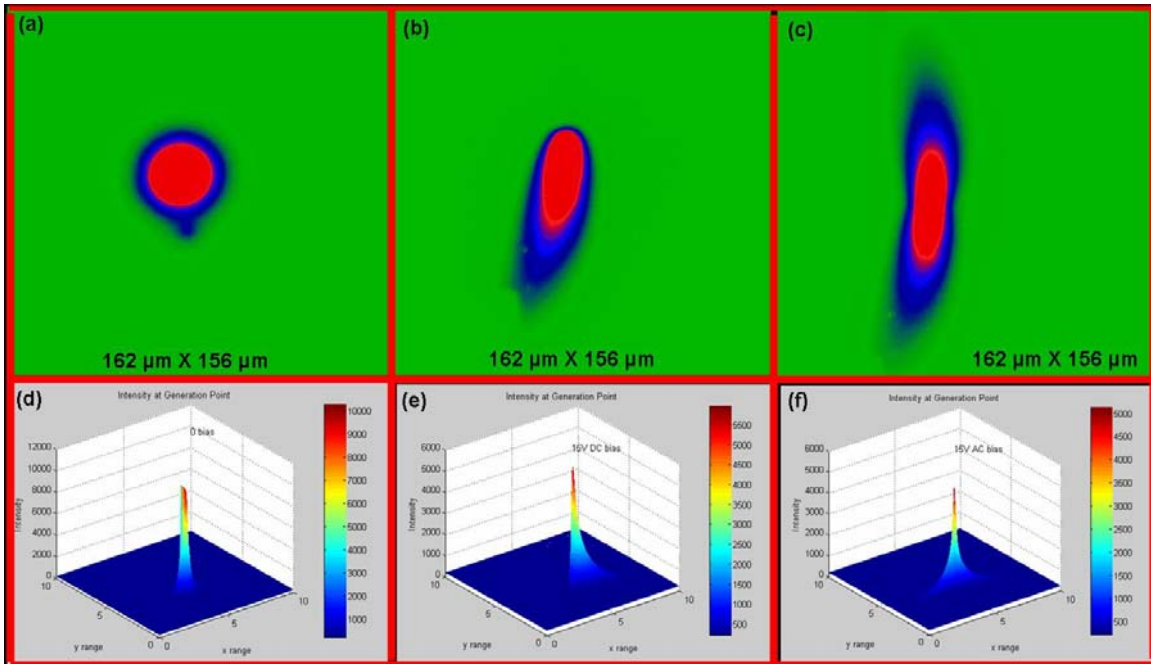


Figure 110. SEM images in spot mode operation for point charge generation.

The technique described in this thesis allows the mapping of local electric fields with high resolution by analyzing the transport behavior under the combined influence of both diffusion and drift predicted by modeling the drift and diffusion in 2D following generation at a point source. Subsequent measurements of electric field profiles have been performed in both uniform and non-uniform regions. The acquired results agree (to within about 10%) with simulations made in COMSOL MULTIPHYSICS software for similar geometry semiconductor planar structures. Fluctuations between the experimental and simulated method are due to material variations, defects and actual characteristics of the material used (e.g., type and quantity of doping), conditions that cannot be easily simulated.

Additionally, the experimental method described in the thesis allows the accurate measurement of the contact resistance with only a two-point contact. The technique illustrates the device's characteristics by determining the exact activation point of the forward biased Schottky diode and further deviations from an ideal linear I-V behavior.

Finally, the method was demonstrated for a geometry where the non-uniformity of the electric field emphasizes the necessity of having an experimental method in order to determine fields with high resolution. The technique described in this thesis is a powerful “tool” for testing the reliability of electronic devices in a radiative environment or in conditions that may alter their electrical behavior.

B. SUGGESTIONS FOR FURTHER RESEARCH

1. Reliability of Semiconductor Devices

After the industrial processing of a wafer containing a large number of integrated circuits, the term “yield” refers to the fraction of successful products that survive final screening and meet specifications relative to the total number that started out to be processed or manufactured. The fact that yielded products have passed the last screen does not mean they do not contain potential or latent defects [13]. The reliability of these devices is directly based on the existence of defects that influence their electrical behavior.

The experimental technique that is described in this thesis allows for detecting these defects not only optically (by using the corresponding CCD camera) but also quantitatively by determining the magnitude of the electric field with high resolution. Since defects influence the electrical behavior of semiconductor devices, the capability of mapping the electric field locally will detect the potential existence of defects.

Additional to the existence of defects, a phenomenon that has a significant effect on the reliability of semiconductor devices is electromigration. Electromigration is characterized by the migration of metal atoms in a conductor through which large direct-current densities pass. Passage of high current densities through interconnects causes time-dependent mass-transport effects that are manifested as surface morphological changes.

2. Electromigration Issues

At a fundamental level, electromigration involves the interaction between current carriers and migrating atoms. Since any metal that leaves the semiconductor interface cannot be replenished [13], electromigration at contacts is of great importance. During the experimental work done for this thesis, it has been noticed that after a period, there was a significant drop in the resistance of the specimen used (Sample #9) resulting in the degradation of its performance. In order to understand the reasons for this material degradation, a series of experiments has been done in order to force electromigration to happen in Sample #9. A characteristic example of the experimental setup for this purpose is illustrated in Figure 111.

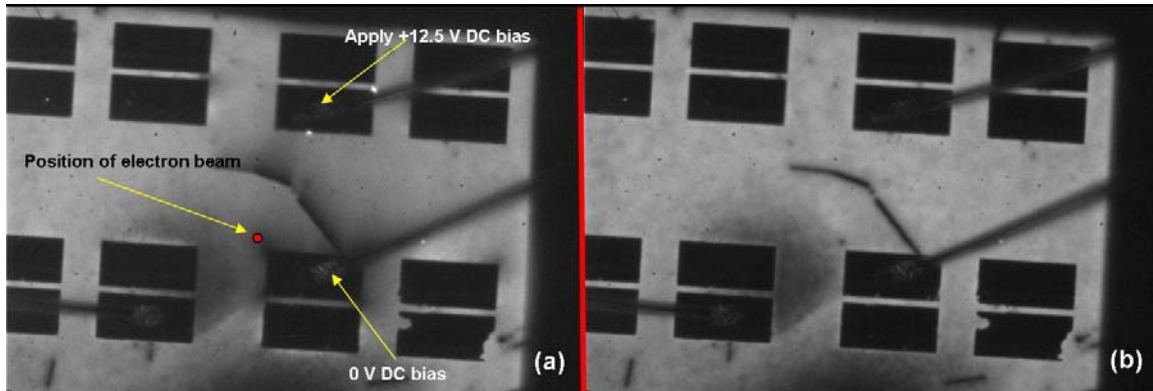


Figure 111. Sample #9 for electromigration study (each image is 874 μm X 589 μm).

The electron beam is positioned as shown in Figure 111 (a) in the non-uniform region of the electric field created by the application of 12.5 V DC bias between the contacts. Electron beam energy was 30 keV and the probe current was 3×10^{-10} A. The specimen remained under the radiation of the electron beam for 2h 30min without changing the position of either the beam or the sample. A series of images have been taken in periodic intervals in order to detect possible deformations of the contacts. Part (b) of Figure 111 represents the final image of the specimen after 2h 30min of radiation (taken without applying bias). By analyzing the images in high resolution, the only difference between parts (a) and (b) is the surface field distribution which disappears when there is no bias.

Naturally, after 2h 30min of radiation there was a significant increase in the temperature of the specimen (from room temperature to almost 77°C). It is very interesting at this point to notice the difference of the electric field magnitude due to temperature increase with respect to time (Figure 112).

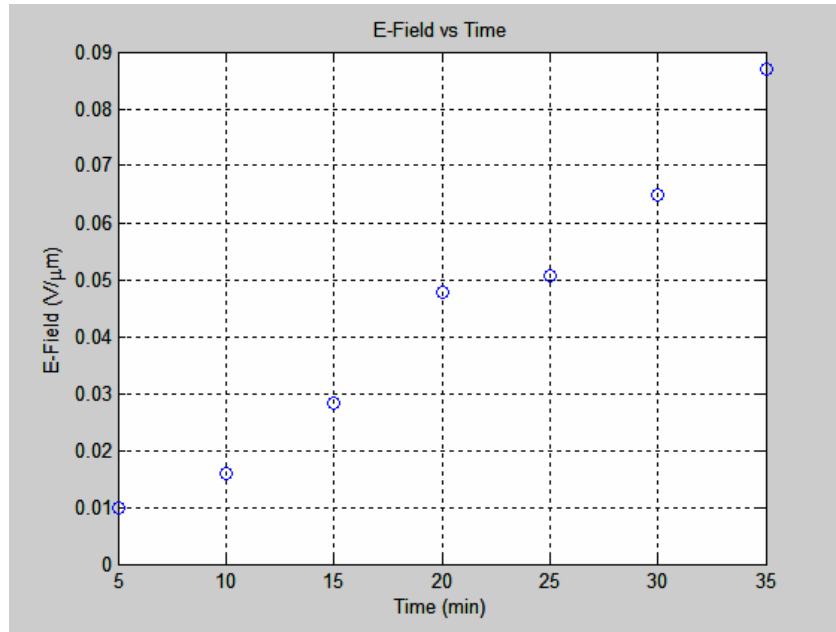


Figure 112. E-Field values with respect to time due to temperature increase.

In Figure 112 it can be seen that the electric field within the semiconductor material (at the point of the incident electron beam) increases as time passes due to the increase in temperature. That means that the contact resistance decreases due to heating. Another point of interest is the existence of some white spots in the perimeter of the contact where the bias was applied [Figure 111 (a)]. These white spots are points where injected charge density is extremely high and represent potential points where electromigration can be accelerated. This can be seen clearly in Figure 113 below where with the application of bias, high charge density is noticed in the corner of the plate (demonstrated with the yellow arrow).

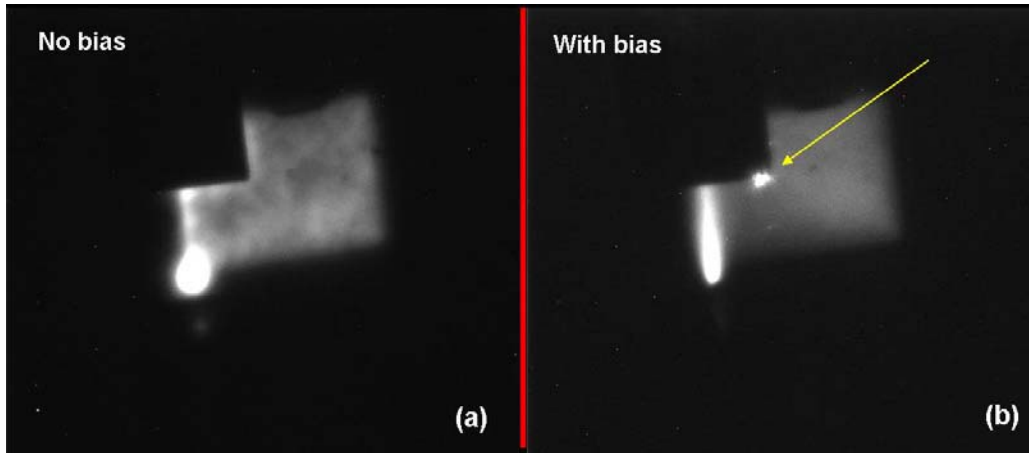


Figure 113. Points with high injected charge density (each image is 247 μm X 215 μm).

The reasons that led to the degradation of Sample #9 may not be related only with the electromigration mechanisms. Possible degradation of the Schottky contacts used in the specimen (Au/Ti/Al_{0.5}Ga_{0.5}As/GaAs capping layer) may change the electrical behavior of the material due to changes to the metal-semiconductor interface. Additionally, the three kind of tests described in [13] concerning the electromigration:

- the temperature-ramp resistance analysis to characterize electromigration (TRACE),
- the breakdown energy of metal (BEM) and
- the standard wafer – level electromigration acceleration test (SWEAT), all are techniques referred especially to the wafer level, requiring simultaneously specific laboratory conditions and capabilities.

Since in electromigration, metal atoms are forced to migrate by a large current density and such areas with high charge density can be identified by the SEM imaging capabilities as shown in Figures 111 and 113 above, an effective method of studying the electromigration issues can be developed. It is also essential to study the effects of the electromigration first in small cross-sectional interconnects where high current densities are expected. The collision between fast moving electrons having high drift velocity with the metal ions can result in material depletion (voids), material accumulation (hillocks) or in an interconnect failure [3].

Finally, another case has been studied in order to explore the effect of “cycling” the applied bias. The term “cycle” means that bias is applied, then switched off and then re-applied. The structure used is illustrated in Figure 114 below. Thermal excitations of the lattice structure due to abrupt voltage differences are anticipated to influence the electrical behavior of the material.

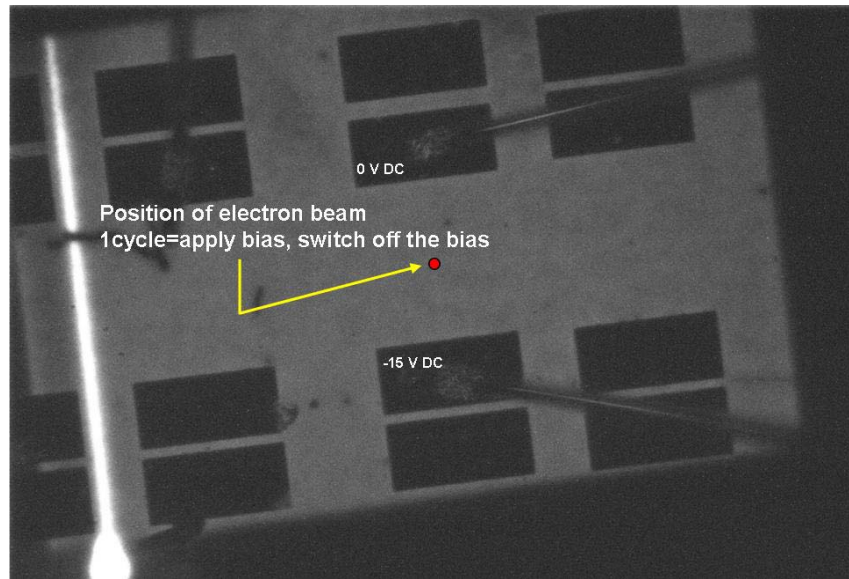


Figure 114. Part of Sample #9 for studying the effects of thermal excitation (874 μm X 589 μm)

In Figure 114 above, the position of the electron beam is shown with the red circle. Electron beam energy is at 30 keV and the probe current at $3\text{E}-9$ A. The applied voltage was -15 V DC bias and it was switched on and off for 30 times continuously with 15 sec intervals between each cycle. The acquired results are shown in Figure 115. It can be seen from the figure that the values of the electric field is not in an horizontal line, as expected in a theoretical situation like this, but they have some fluctuations ($\approx 4\%$) due to thermal excitation. By microscopic analysis, there were not any signs of electromigration or changes in the formation of the structure.

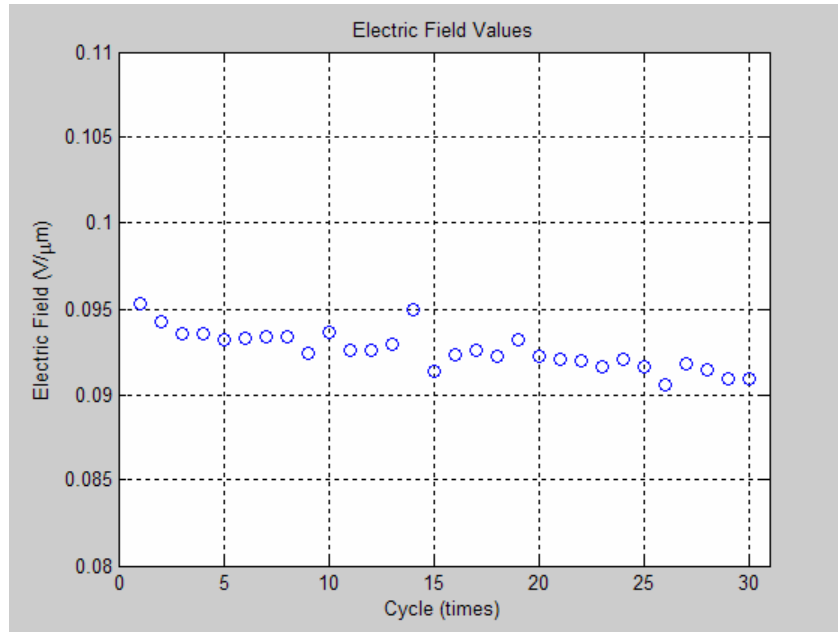


Figure 115. E-Field values vs. times of power cycling.

In summary, this work has successfully demonstrated that transport imaging can be used as a quantitative method for electric field mapping. The technique has potential in the study of defect behavior and electromigration, areas with extreme scientific significance in the micro-electronics industry.

APPENDIX A. MATLAB CODE FOR EVALUATING THE DC MATHEMATICAL MODEL

```
%FIND THEORETICAL DC MODEL EQUATION  
%CREATED BY PAVLOS ANDRIKOPOULOS
```

```
%READ EXCEL FILES AND EXTRACT DATA
```

```
A=xlsread('MODEL_DATA')
```

```
x1= A(:,1)
```

```
[mx1,r]=max(x1)
```

```
mmx1=max(mx1)
```

```
x2= A(:,2)
```

```
[mx2,r]=max(x2)
```

```
mmx2=max(mx2)
```

```
x3= A(:,3)
```

```
[mx3,r]=max(x3)
```

```
mmx3=max(mx3)
```

```
x4= A(:,4)
```

```
[mx4,r]=max(x4)
```

```
mmx4=max(mx4)
```

```
x5= A(:,5)
```

```
[mx5,r]=max(x5)
```

```
mmx5=max(mx5)
```

```
x6= A(:,6)
```

```
[mx6,r]=max(x6)
```

```
mmx6=max(mx6)
```

```
x7= A(:,7)
```

```
[mx7,r]=max(x7)
```

```
mmx7=max(mx7)
```

```
x8= A(:,8)
```

```
[mx8,r]=max(x8)
```

```
mmx8=max(mx8)
```

```
x9= A(:,9)
```

```
[mx9,r]=max(x9)
```

```
mmx9=max(mx9)
```

```
x10= A(:,10)
```

```
[mx10,r]=max(x10)
```

```
mmx10=max(mx10)
```

```
x11= A(:,11)
```

```
[mx11,r]=max(x11)
```

```
mmx11=max(mx11)
```

```
x12= A(:,12)
```

```
[mx12,r]=max(x12)
```

```
mmx12=max(mx12)
```

```
x13= A(:,13)
```

```
[mx13,r]=max(x13)
```

```
mmx13=max(mx13)
```

```
x14= A(:,14)
```

```
[mx14,r]=max(x14)
```

```
mmx14=max(mx14)
```

```
x15= A(:,15)
```

```
[mx15,r]=max(x15)
```

```
mmx15=max(mx15)
```

```
x16= A(:,16)
```

```

[mx16, r]=max(x16)
mmx16=max(mx16)
x17= A(:, 17)
[mx17, r]=max(x17)
mmx17=max(mx17)
x18= A(:, 18)
[mx18, r]=max(x18)
mmx18=max(mx18)
x19= A(:, 19)
[mx19, r]=max(x19)
mmx19=max(mx19)
x20= A(:, 20)
[mx20, r]=max(x20)
mmx20=max(mx20)
x21= A(:, 21)
[mx21, r]=max(x21)
mmx21=max(mx21)
x22= A(:, 22)
[mx22, r]=max(x22)
mmx22=max(mx22)
x23= A(:, 23)
[mx23, r]=max(x23)
mmx23=max(mx23)
x24= A(:, 24)
[mx24, r]=max(x24)
mmx24=max(mx24)
x25= A(:, 25)
[mx25, r]=max(x25)
mmx25=max(mx25)
x26= A(:, 26)
[mx26, r]=max(x26)
mmx26=max(mx26)
x27= A(:, 27)
[mx27, r]=max(x27)
mmx27=max(mx27)
x28= A(:, 28)
[mx28, r]=max(x28)
mmx28=max(mx28)
x29= A(:, 29)
[mx29, r]=max(x29)
mmx29=max(mx29)
x30= A(:, 30)
[mx30, r]=max(x30)
mmx30=max(mx30)
x31= A(:, 31)
[mx31, r]=max(x31)
mmx31=max(mx31)
x32= A(:, 32)
[mx32, r]=max(x32)
mmx32=max(mx32)
x33= A(:, 33)
[mx33, r]=max(x33)
mmx33=max(mx33)
x34= A(:, 34)
[mx34, r]=max(x34)
mmx34=max(mx34)
x35= A(:, 35)

```

```

[mx35,r]=max(x35)
mmx35=max(mx35)
x36= A(:,36)
[mx36,r]=max(x36)
mmx36=max(mx36)

%CREATE MATRIX FOR MAX VALUES
X=[mmx1 mmx2 mmx3 mmx4 mmx5 mmx6 mmx7 mmx8 mmx9 mmx10 mmx11 mmx12 mmx13
mmx14 mmx15 mmx16 mmx17 mmx18 mmx19 mmx20 mmx21 mmx22 mmx23 mmx24 mmx25
mmx26 mmx27 mmx28 mmx29 mmx30 mmx31 mmx32 mmx33 mmx34 mmx35 mmx36]

%DETERMINE THE X VECTOR
x=(-30:0.5:30)

%CREATE THE GRAPH INTENSITY VS x
plot(x,A(:,1),'b')
hold on
plot(x,A(:,4),'g')
hold on
plot(x,A(:,6),'r')
hold on
plot(x,A(:,9),'c')
hold on
plot(x,A(:,11),'m')
hold on
plot(x,A(:,13),'y')
hold on
plot(x,A(:,15),'k')
hold on
plot(x,A(:,17),'b-')
hold on
plot(x,A(:,19),'g-')
hold on
plot(x,A(:,22),'r-')
hold on
plot(x,A(:,25),'c-')
hold on
plot(x,A(:,27),'m-')
hold on
plot(x,A(:,29),'y-')
hold on
plot(x,A(:,32),'k-')
hold on
plot(x,A(:,34),'b.')
hold on
plot(x,A(:,36),'g.')
hold off

grid on
xlabel('x')
ylabel('Intensity Ratio')
title('Normalized Intensity Ratio (Theoretical Model)')
legend('0 V/\mum','30E-4 V/\mum','44E-4 V/\mum','70E-4 V/\mum','100E-4
V/\mum','131.50E-4 V/\mum','170E-4 V/\mum','209.50E-4 V/\mum','250E-4
V/\mum','313.50E-4 V/\mum','370E-4 V/\mum','412E-4 V/\mum','450E-4
V/\mum','521E-4 V/\mum','560E-4 V/\mum','600E-4 V/\mum',2)

```

```

%CURVE FITTING OF THE RESULTS
B=xlsread('VOLTAGE_DATA')
Eold= B(:,1)
E=Eold'
Iold=X
Inorm=Iold/0.01739318611415140
n=2;
p=polyfit(Inorm,E,n)
xi=(0.40:0.01:1.0);
yi=polyval(p,xi);
figure
plot(Inorm,E,'o',xi,yi,'-')
grid on
xlabel('Peak Intensity Ratio'),ylabel('E-Field (V/\mum)')
title('Curve Fit for DC Theoretical Model')
text(0.45,0.005,'(0.0842*I^2)-(0.2162*I)+(0.1351)')
legend('Theoretical Model','Curve Fitting',1)
figure
plot (E,Inorm,'o')
grid on
xlabel('E-Field (V/\mum)'),ylabel('Peak Intensity Ratio')
title('Intensity ratio vs Applied Electric Field')

% Etheory=(0.0842*I.*I)-(0.2162*I)+0.1351

```

APPENDIX B. MATLAB CODE FOR MAPPING ELECTRIC FIELD VIA TRANSPORT IMAGING TECHNIQUE

```
%MATLAB CODE FOR FINDING THE ELECTRIC FIELD FROM SEM IMAGES  
%DC CURRENT  
%CREATED BY ANDRIKOPOULOS PAVLOS
```

```
%POSITION_1-0V UP TO POSITION_23-0V  
%READ TIF FILES AND EXTRACT THE MAX VALUE
```

```
Z1=imread('P1_0V.TIF')  
Z1=double(Z1)  
[Y1,X]=max(Z1)  
mmx1=max(Y1)  
Z2=imread('P2_0V.TIF')  
Z2=double(Z2)  
[Y2,X]=max(Z2)  
mmx2=max(Y2)  
Z3=imread('P3_0V.TIF')  
Z3=double(Z3)  
[Y3,X]=max(Z3)  
mmx3=max(Y3)  
Z4=imread('P4_0V.TIF')  
Z4=double(Z4)  
[Y4,X]=max(Z4)  
mmx4=max(Y4)  
Z5=imread('P5_0V.TIF')  
Z5=double(Z5)  
[Y5,X]=max(Z5)  
mmx5=max(Y5)  
Z6=imread('P6_0V.TIF')  
Z6=double(Z6)  
[Y6,X]=max(Z6)  
mmx6=max(Y6)  
Z7=imread('P7_0V.TIF')  
Z7=double(Z7)  
[Y7,X]=max(Z7)  
mmx7=max(Y7)  
Z8=imread('P8_0V.TIF')  
Z8=double(Z8)  
[Y8,X]=max(Z8)  
mmx8=max(Y8)  
Z9=imread('P9_0V.TIF')  
Z9=double(Z9)  
[Y9,X]=max(Z9)  
mmx9=max(Y9)  
Z10=imread('P10_0V.TIF')  
Z10=double(Z10)  
[Y10,X]=max(Z10)  
mmx10=max(Y10)  
Z11=imread('P11_0V.TIF')  
Z11=double(Z11)  
[Y11,X]=max(Z11)  
mmx11=max(Y11)
```



```

Z12=imread('P12_0V.TIF')
Z12=double(Z12)
[Y12,X]=max(Z12)
mmx12=max(Y12)
Z13=imread('P13_0V.TIF')
Z13=double(Z13)
[Y13,X]=max(Z13)
mmx13=max(Y13)
Z14=imread('P14_0V.TIF')
Z14=double(Z14)
[Y14,X]=max(Z14)
mmx14=max(Y14)
Z15=imread('P15_0V.TIF')
Z15=double(Z15)
[Y15,X]=max(Z15)
mmx15=max(Y15)
Z16=imread('P16_0V.TIF')
Z16=double(Z16)
[Y16,X]=max(Z16)
mmx16=max(Y16)
Z17=imread('P17_0V.TIF')
Z17=double(Z17)
[Y17,X]=max(Z17)
mmx17=max(Y17)
Z18=imread('P18_0V.TIF')
Z18=double(Z18)
[Y18,X]=max(Z18)
mmx18=max(Y18)
Z19=imread('P19_0V.TIF')
Z19=double(Z19)
[Y19,X]=max(Z19)
mmx19=max(Y19)
Z20=imread('P20_0V.TIF')
Z20=double(Z20)
[Y20,X]=max(Z20)
mmx20=max(Y20)
Z21=imread('P21_0V.TIF')
Z21=double(Z21)
[Y21,X]=max(Z21)
mmx21=max(Y21)
Z22=imread('P22_0V.TIF')
Z22=double(Z22)
[Y22,X]=max(Z22)
mmx22=max(Y22)
Z23=imread('P23_0V.TIF')
Z23=double(Z23)
[Y23,X]=max(Z23)
mmx23=max(Y23)

%POSITION_1-15V UP TO POSITION_23-15V
%READ TIF FILES AND EXTRACT THE MAX VALUE

A1=imread('P1_15V.TIF')
A1=double(A1)
[B1,X]=max(A1)
mmy1=max(B1)

```

```

A2=imread('P2_15V.TIF')
A2=double(A2)
[B2,X]=max(A2)
mmy2=max(B2)
A3=imread('P3_15V.TIF')
A3=double(A3)
[B3,X]=max(A3)
mmy3=max(B3)
A4=imread('P4_15V.TIF')
A4=double(A4)
[B4,X]=max(A4)
mmy4=max(B4)
A5=imread('P5_15V.TIF')
A5=double(A5)
[B5,X]=max(A5)
mmy5=max(B5)
A6=imread('P6_15V.TIF')
A6=double(A6)
[B6,X]=max(A6)
mmy6=max(B6)
A7=imread('P7_15V.TIF')
A7=double(A7)
[B7,X]=max(A7)
mmy7=max(B7)
A8=imread('P8_15V.TIF')
A8=double(A8)
[B8,X]=max(A8)
mmy8=max(B8)
A9=imread('P9_15V.TIF')
A9=double(A9)
[B9,X]=max(A9)
mmy9=max(B9)
A10=imread('P10_15V.TIF')
A10=double(A10)
[B10,X]=max(A10)
mmy10=max(B10)
A11=imread('P11_15V.TIF')
A11=double(A11)
[B11,X]=max(A11)
mmy11=max(B11)
A12=imread('P12_15V.TIF')
A12=double(A12)
[B12,X]=max(A12)
mmy12=max(B12)
A13=imread('P13_15V.TIF')
A13=double(A13)
[B13,X]=max(A13)
mmy13=max(B13)
A14=imread('P14_15V.TIF')
A14=double(A14)
[B14,X]=max(A14)
mmy14=max(B14)
A15=imread('P15_15V.TIF')
A15=double(A15)
[B15,X]=max(A15)
mmy15=max(B15)
A16=imread('P16_15V.TIF')

```

```

A16=double(A16)
[B16,X]=max(A16)
mmy16=max(B16)
A17=imread('P17_15V.TIF')
A17=double(A17)
[B17,X]=max(A17)
mmy17=max(B17)
A18=imread('P18_15V.TIF')
A18=double(A18)
[B18,X]=max(A18)
mmy18=max(B18)
A19=imread('P19_15V.TIF')
A19=double(A19)
[B19,X]=max(A19)
mmy19=max(B19)
A20=imread('P20_15V.TIF')
A20=double(A20)
[B20,X]=max(A20)
mmy20=max(B20)
A21=imread('P21_15V.TIF')
A21=double(A21)
[B21,X]=max(A21)
mmy21=max(B21)
A22=imread('P22_15V.TIF')
A22=double(A22)
[B22,X]=max(A22)
mmy22=max(B22)
A23=imread('P23_15V.TIF')
A23=double(A23)
[B23,X]=max(A23)
mmy23=max(B23)

%CREATE MATRIX FOR MAX VALUES OF 0 VOLTS
X=[mxx1 mx2 mx3 mx4 mx5 mx6 mx7 mx8 mx9 mx10 mx11 mx12 mx13
mxx14 mx15 mx16 mx17 mx18 mx19 mx20 mx21 mx22 mx23]

%CREATE MATRIX FOR MAX VALUES OF 15 VOLTS
Y=[mmy1 mmy2 mmy3 mmy4 mmy5 mmy6 mmy7 mmy8 mmy9 mmy10 mmy11 mmy12 mmy13
mmy14 mmy15 mmy16 mmy17 mmy18 mmy19 mmy20 mmy21 mmy22 mmy23]

%CALCULATE NORMALIZED INTENSITY
Io=240
I=(Y-Io)./(X-Io)

%CALCULATE VALUES FOR DISTANCE
%SET VALUES FOR X (H=HORIZONTAL)
H=[10.02,10.05,10.07,10.09,10.11,10.13,10.15,10.17,10.19,10.21,10.23,10
.25,10.27,10.29,10.31,10.33,10.35,10.37,10.39,10.41,10.51,10.53,10.55]
%SET VALUES FOR Y (V=VERTICAL)
V=[13.80,13.80,13.80,13.80,13.80,13.80,13.80,13.80,13.80,13.80,13.80,13
.80,13.80,13.80,13.80,13.78,13.78,13.78,13.78,13.78,13.78,13.78,13.78]

%EVALUATE THE DISTANCE FROM INITIAL POINT
D=sqrt((H-10.02).*(H-10.02)+(13.80-V).*(13.80-V))

```

```

%CREATE THE GRAPH
plot(D,I,'bo')
grid on
xlabel('Distance (mm)')
ylabel('Normalized Intensity Ratio')
title('Normalized Intensity Ratio vs Distance')

%EVALUATION OF THEORITICAL MODEL FOR DC AND CREATION OF THE
CORRESPONDING GRAPH
E=[0 0.001 0.002 0.003 0.004 0.0044 0.005 0.006 0.007
0.008 0.01 0.012 0.0132 0.015 0.017 0.02 0.021 0.023
0.025 0.027 0.029 0.0314 0.033 0.035 0.037 0.039 0.0412
0.043 0.045 0.047 0.049 0.0521 0.054 0.056 0.058 0.06];
Iold=[0.0173931861141514 0.0173686237268924 0.0172957143671621
0.0171766638980226 0.0170149206611566 0.0169392356157452
0.0168149071852186 0.0166530028607825 0.0164875036781727
0.0162940163629757 0.0158421498452957 0.0153323559252167
0.0150242440677031 0.0145185911735649 0.0139712700358284
0.0131890887893245 0.0129837833235535 0.0125496590763713
0.0121406835833828 0.0117481446599407 0.0113730073666232
0.0109547598726452 0.0106754611667708 0.0103523335916252
0.0100454544116619 0.00975404133410867 0.00945037407473868
0.00921432745937045 0.00896439018545242 0.00872663147449506
0.00850034248019468 0.00818920174584799 0.00801488318079925
0.00783888525452678 0.00767012138997172 0.00750822234977514];
Inorm=Iold/0.01739318611415140
n=2;
p=polyfit(Inorm,E,n)
xi=(0.40:0.01:1.0);
yi=polyval(p,xi);

figure
plot(Inorm,E,'o',xi,yi,'-')
grid on
xlabel('Intensity Ratio'),ylabel('E-Field (V/mum)')
title('Curve Fit for DC Theoretical Model')
text(0.42,0.005,'Etheory=(0.0842*I^2)-(0.2162*I)+0.1351')

%APPLY CORRECTION
Etheory=(0.0842*I.*I)-(0.2162*I)+0.1351

%CREATE THE FINAL GRAPH
figure
plot(D,I,'o')
grid on
xlabel('Distance (mm)'),ylabel('Normalized Intensity Ratio')
title('Experimental Measurement')

figure
plot(D,Etheory,'o')
grid on
xlabel('Distance (mm)'),ylabel('E-Field (V/\mum)')
title('E-Field vs Distance')

```

THIS PAGE INTENTIONALLY LEFT BLANK

APPENDIX C. MATLAB CODE FOR EVALUATION OF CONTACT RESISTANCE

```
%EVALUATION OF DROP OF VOLTAGE BETWEEN THE CONTACT PLATES
%DC CURRENT
%CREATED BY ANDRIKOPOULOS PAVLOS
```

```
%POSITION 1, MEASUREMENTS 1-31, 0V (DC)
%READ TIF FILES AND EXTRACT THE MAX VALUE
```

```
Z1=imread('P1_0V.TIF')
Z1=double(Z1)
[Y1,X]=max(Z1)
mmx1=max(Y1)
Z2=imread('P2_0V.TIF')
Z2=double(Z2)
[Y2,X]=max(Z2)
mmx2=max(Y2)
Z3=imread('P3_0V.TIF')
Z3=double(Z3)
[Y3,X]=max(Z3)
mmx3=max(Y3)
Z4=imread('P4_0V.TIF')
Z4=double(Z4)
[Y4,X]=max(Z4)
mmx4=max(Y4)
Z5=imread('P5_0V.TIF')
Z5=double(Z5)
[Y5,X]=max(Z5)
mmx5=max(Y5)
Z6=imread('P6_0V.TIF')
Z6=double(Z6)
[Y6,X]=max(Z6)
mmx6=max(Y6)
Z7=imread('P7_0V.TIF')
Z7=double(Z7)
[Y7,X]=max(Z7)
mmx7=max(Y7)
Z8=imread('P8_0V.TIF')
Z8=double(Z8)
[Y8,X]=max(Z8)
mmx8=max(Y8)
Z9=imread('P9_0V.TIF')
Z9=double(Z9)
[Y9,X]=max(Z9)
mmx9=max(Y9)
Z10=imread('P10_0V.TIF')
Z10=double(Z10)
[Y10,X]=max(Z10)
mmx10=max(Y10)
Z11=imread('P11_0V.TIF')
Z11=double(Z11)
[Y11,X]=max(Z11)
mmx11=max(Y11)
```

```

Z12=imread('P12_OV.TIF')
Z12=double(Z12)
[Y12,X]=max(Z12)
mmx12=max(Y12)
Z13=imread('P13_OV.TIF')
Z13=double(Z13)
[Y13,X]=max(Z13)
mmx13=max(Y13)
Z14=imread('P14_OV.TIF')
Z14=double(Z14)
[Y14,X]=max(Z14)
mmx14=max(Y14)
Z15=imread('P15_OV.TIF')
Z15=double(Z15)
[Y15,X]=max(Z15)
mmx15=max(Y15)
Z16=imread('P16_OV.TIF')
Z16=double(Z16)
[Y16,X]=max(Z16)
mmx16=max(Y16)
Z17=imread('P17_OV.TIF')
Z17=double(Z17)
[Y17,X]=max(Z17)
mmx17=max(Y17)
Z18=imread('P18_OV.TIF')
Z18=double(Z18)
[Y18,X]=max(Z18)
mmx18=max(Y18)
Z19=imread('P19_OV.TIF')
Z19=double(Z19)
[Y19,X]=max(Z19)
mmx19=max(Y19)
Z20=imread('P20_OV.TIF')
Z20=double(Z20)
[Y20,X]=max(Z20)
mmx20=max(Y20)
Z21=imread('P21_OV.TIF')
Z21=double(Z21)
[Y21,X]=max(Z21)
mmx21=max(Y21)
Z22=imread('P22_OV.TIF')
Z22=double(Z22)
[Y22,X]=max(Z22)
mmx22=max(Y22)
Z23=imread('P23_OV.TIF')
Z23=double(Z23)
[Y23,X]=max(Z23)
mmx23=max(Y23)
Z24=imread('P24_OV.TIF')
Z24=double(Z24)
[Y24,X]=max(Z24)
mmx24=max(Y24)
Z25=imread('P25_OV.TIF')
Z25=double(Z25)
[Y25,X]=max(Z25)
mmx25=max(Y25)
Z26=imread('P26_OV.TIF')

```

```

Z26=double (Z26)
[Y26,X]=max (Z26)
mmx26=max (Y26)
Z27=imread ('P27_0V.TIF')
Z27=double (Z27)
[Y27,X]=max (Z27)
mmx27=max (Y27)
Z28=imread ('P28_0V.TIF')
Z28=double (Z28)
[Y28,X]=max (Z28)
mmx28=max (Y28)
Z28=imread ('P28_0V.TIF')
Z28=double (Z28)
[Y28,X]=max (Z28)
mmx28=max (Y28)
Z29=imread ('P29_0V.TIF')
Z29=double (Z29)
[Y29,X]=max (Z29)
mmx29=max (Y29)
Z30=imread ('P30_0V.TIF')
Z30=double (Z30)
[Y30,X]=max (Z30)
mmx30=max (Y30)
Z31=imread ('P31_0V.TIF')
Z31=double (Z31)
[Y31,X]=max (Z31)
mmx31=max (Y31)

%POSITION 1-FROM 0V TO 15V (0.5V INCREMENTS) (DC)
%READ TIF FILES AND EXTRACT THE MAX VALUE

A1=imread ('P1.TIF')
A1=double (A1)
[B1,X]=max (A1)
mmy1=max (B1)
A2=imread ('P2.TIF')
A2=double (A2)
[B2,X]=max (A2)
mmy2=max (B2)
A3=imread ('P3.TIF')
A3=double (A3)
[B3,X]=max (A3)
mmy3=max (B3)
A4=imread ('P4.TIF')
A4=double (A4)
[B4,X]=max (A4)
mmy4=max (B4)
A5=imread ('P5.TIF')
A5=double (A5)
[B5,X]=max (A5)
mmy5=max (B5)
A6=imread ('P6.TIF')
A6=double (A6)
[B6,X]=max (A6)
mmy6=max (B6)
A7=imread ('P7.TIF')

```



```
A7=double(A7)
[B7,X]=max(A7)
mmy7=max(B7)
A8=imread('P8.TIF')
A8=double(A8)
[B8,X]=max(A8)
mmy8=max(B8)
A9=imread('P9.TIF')
A9=double(A9)
[B9,X]=max(A9)
mmy9=max(B9)
A10=imread('P10.TIF')
A10=double(A10)
[B10,X]=max(A10)
mmy10=max(B10)
A11=imread('P11.TIF')
A11=double(A11)
[B11,X]=max(A11)
mmy11=max(B11)
A12=imread('P12.TIF')
A12=double(A12)
[B12,X]=max(A12)
mmy12=max(B12)
A13=imread('P13.TIF')
A13=double(A13)
[B13,X]=max(A13)
mmy13=max(B13)
A14=imread('P14.TIF')
A14=double(A14)
[B14,X]=max(A14)
mmy14=max(B14)
A15=imread('P15.TIF')
A15=double(A15)
[B15,X]=max(A15)
mmy15=max(B15)
A16=imread('P16.TIF')
A16=double(A16)
[B16,X]=max(A16)
mmy16=max(B16)
A17=imread('P17.TIF')
A17=double(A17)
[B17,X]=max(A17)
mmy17=max(B17)
A18=imread('P18.TIF')
A18=double(A18)
[B18,X]=max(A18)
mmy18=max(B18)
A19=imread('P19.TIF')
A19=double(A19)
[B19,X]=max(A19)
mmy19=max(B19)
A20=imread('P20.TIF')
A20=double(A20)
[B20,X]=max(A20)
mmy20=max(B20)
A21=imread('P21.TIF')
A21=double(A21)
```

```

[B21, X]=max(A21)
mmy21=max(B21)
A22=imread('P22.TIF')
A22=double(A22)
[B22, X]=max(A22)
mmy22=max(B22)
A23=imread('P23.TIF')
A23=double(A23)
[B23, X]=max(A23)
mmy23=max(B23)
A24=imread('P24.TIF')
A24=double(A24)
[B24, X]=max(A24)
mmy24=max(B24)
A25=imread('P25.TIF')
A25=double(A25)
[B25, X]=max(A25)
mmy25=max(B25)
A26=imread('P26.TIF')
A26=double(A26)
[B26, X]=max(A26)
mmy26=max(B26)
A27=imread('P27.TIF')
A27=double(A27)
[B27, X]=max(A27)
mmy27=max(B27)
A28=imread('P28.TIF')
A28=double(A28)
[B28, X]=max(A28)
mmy28=max(B28)
A29=imread('P29.TIF')
A29=double(A29)
[B29, X]=max(A29)
mmy29=max(B29)
A30=imread('P30.TIF')
A30=double(A30)
[B30, X]=max(A30)
mmy30=max(B30)
A31=imread('P31.TIF')
A31=double(A31)
[B31, X]=max(A31)
mmy31=max(B31)

%CREATE MATRIX FOR MAX VALUES OF 0 VOLTS
X=[mxx1 mx2 mx3 mx4 mx5 mx6 mx7 mx8 mx9 mx10 mx11 mx12 mx13
mxx14 mx15 mx16 mx17 mx18 mx19 mx20 mx21 mx22 mx23 mx24 mx25
mxx26 mx27 mx28 mx29 mx30 mx31]

%CREATE MATRIX FOR MAX VALUES OF 15 VOLTS
Y=[mmy1 mmy2 mmy3 mmy4 mmy5 mmy6 mmy7 mmy8 mmy9 mmy10 mmy11 mmy12 mmy13
mmy14 mmy15 mmy16 mmy17 mmy18 mmy19 mmy20 mmy21 mmy22 mmy23 mmy24 mmy25
mmy26 mmy27 mmy28 mmy29 mmy30 mmy31]

%CALCULATE NORMALIZED INTENSITY
Io=240
I=(Y-Io)./(X-Io)

```

```

%SET VALUES FOR APPLIED VOLTAGE
V=0:0.5:15

%EVALUATE APPLIED VOLTAGE W.R.T. DISTANCE BETWEEN PLATES (V/μm)
%SET VALUES FOR OUTPUT CURRENT
% Iout=[0.001 0.032 0.537 1.049 4.080 6.335 8.710 11.158 13.658 16.200
18.767 21.355 23.952 26.562 29.190 31.836 34.503 37.187 39.895 42.647
45.420 48.390 51.230 54.090 56.960 59.890 62.760 65.640 68.540 71.340
74.230]
% P=V.*Iout
% R=(V.*V)./P
% V1=Iout.*R/191
V1=V/191

%CREATE THE GRAPH
plot(V,I,'bo')
grid on
xlabel('Applied Voltage (V)')
ylabel('Intensity Ratio')
title('Normalized Intensity Ratio vs Applied Voltage (Experimental
Data)')

%EVALUATION OF THEORITICAL MODEL FOR DC AND CREATION OF THE
CORRESPONDING GRAPH
E=[0 0.001 0.002 0.003 0.004 0.0044 0.005 0.006 0.007
0.008 0.01 0.012 0.0132 0.015 0.017 0.02 0.021 0.023
0.025 0.027 0.029 0.0314 0.033 0.035 0.037 0.039 0.0412
0.043 0.045 0.047 0.049 0.0521 0.054 0.056 0.058 0.06];
Iold=[0.0173931861141514 0.0173686237268924 0.0172957143671621
0.0171766638980226 0.0170149206611566 0.0169392356157452
0.0168149071852186 0.0166530028607825 0.0164875036781727
0.0162940163629757 0.0158421498452957 0.0153323559252167
0.0150242440677031 0.0145185911735649 0.0139712700358284
0.0131890887893245 0.0129837833235535 0.0125496590763713
0.0121406835833828 0.0117481446599407 0.0113730073666232
0.0109547598726452 0.0106754611667708 0.0103523335916252
0.0100454544116619 0.00975404133410867 0.00945037407473868
0.00921432745937045 0.00896439018545242 0.00872663147449506
0.00850034248019468 0.00818920174584799 0.00801488318079925
0.00783888525452678 0.00767012138997172 0.00750822234977514];
Inorm=Iold/0.01739318611415140
n=2;
p=polyfit(Inorm,E,n)
xi=(0.40:0.01:1.0);
yi=polyval(p,xi);

figure
plot(Inorm,E,'o',xi,yi,'-')
grid on
xlabel('Intensity Ratio'),ylabel('E-Field (V/mum)')
title('Curve Fit for DC Theoretical Model')
legend('Theoretical','Curve Fit')
text(0.42,0.005,'Etheory=(0.0842*I^2)-(0.2162*I)+0.1351')

```

```

%APPLY CORRECTION
Etheory=(0.0842*I.*I)-(0.2162*I)+0.1351

%CREATE THE FINAL GRAPH
figure
plot(V,Etheory,'o')
hold on
plot(V,V1,'-')
hold off
legend('Experimental','Theoretical')
grid on
xlabel('Applied Voltage (V)'),ylabel('E-Field (V/\mum)')
title('E-Field vs Applied Voltage')

%CREATE THE FINAL GRAPH (Log Scale)
figure
semilogy(V,Etheory,'-o')
hold on
semilogy(V,V1,'-')
hold off
legend('Experimental','Theoretical')
grid on
xlabel('Applied Voltage (V)'),ylabel('E-Field (V/\mum)')
title('E-Field vs Applied Voltage')

%CREATE THE FINAL GRAPH (Log Scale)
figure
loglog(V,Etheory,'-o')
hold on
loglog(V,V1,'-')
hold off
legend('Experimental','Theoretical')
grid on
xlabel('Applied Voltage (V)'),ylabel('E-Field (V/\mum)')
title('E-Field vs Applied Voltage')

%CREATE THE FINAL GRAPH WITHOUT LINE
figure
plot(V,Etheory,'-o')
legend('Experimental')
grid on
xlabel('Applied Voltage (V)'),ylabel('E-Field (V/\mum)')
title('E-Field vs Applied Voltage')

```

THIS PAGE INTENTIONALLY LEFT BLANK

APPENDIX D. MATLAB CODE FOR COMSOL DATA

```
%ANALYZE DATA FROM COMSOL
%CREATED BY PAVLOS ANDRIKOPOULOS

%READ DATA FROM .txt FILES
load EX.txt
load EY.txt
load EZ.txt
x1=EX(:,2)
y1=EX(:,1)
x2=EY(:,2)
y2=EY(:,1)
x3=EZ(:,2)
y3=EZ(:,1)
x=sqrt(x1.*x1+x2.*x2+x3.*x3)
d=y1

%CREATE THE GRAPHS

%CREATE GRAPH FOR ELECTRIC FIELD IN X-DIRECTION
figure
plot(y1,x1)
grid on
xlabel('Distance (m)')
ylabel('Electric Field (V/m)')
title('Electric Field - x component')

%CREATE GRAPH FOR ELECTRIC FIELD IN Y-DIRECTION
figure
plot(y2,x2)
grid on
xlabel('Distance (m)')
ylabel('Electric Field (V/m)')
title('Electric Field - y component')

%CREATE GRAPH FOR ELECTRIC FIELD IN Z-DIRECTION
figure
plot(y3,x3)
grid on
xlabel('Distance (m)')
ylabel('Electric Field (V/m)')
title('Electric Field - z component')

%CREATE GRAPH FOR MAGNITUDE OF TOTAL ELECTRIC FIELD
figure
plot(d,x)
grid on
xlabel('Distance (m)')
ylabel('Electric Field (V/m)')
title('Electric Field (V/m)')
```

THIS PAGE INTENTIONALLY LEFT BLANK

LIST OF REFERENCES

1. Driggers, Ronald G., Cox, Paul and Edwards, Timothy, *Introduction to Infrared and Electro-optical Systems*, Artech House, Boston-London, 1999.
2. Haegel, N.M., Fabri, J.D. and Coleman, M.P., *Direct Transport Imaging in Planar Structures*, Applied Physics Letter, Volume 84, Number 8, 2004.
3. Kasap, S.O., *Principles of Electronic Materials and Devices*, 3rd edition, McGraw Hill, 2006.
4. Yacobi, B.G. and Holt, D.B., *Cathodoluminescence Microscopy of Inorganic Solids*, Plenum Press, New York and London, 1990.
5. Everhart, T.E., and Hoff, P.H., *J. Applied Physics*, 42, 5837, 1971.
6. Goldstein, Joseph and others, *Scanning Electron Microscopy and X-Ray Microanalysis*, 3rd edition, Kleiner Academic – Plenum Publishers.
7. Hovington, P., Drouin, D., and Gauvin, R., *Scanning*, 19, 1, 1997.
8. Kanaya, K., and Okayama, S., *J. Phys. D. Appl. Phys.* 7, 1303, 1972.
9. Luber, David R., *Direct Imaging of Minority Charge Carrier Transport in Luminescent Semiconductors*, Master's Thesis, Naval Postgraduate School, Monterey, California, September 2005.
10. Boone, Thomas D., Tsukamoto, Hironori and Woodall, Jerry M., *Intensity and Spatial Modulation of Spontaneous Emission in GaAs by Field Aperture Selecting Transport*, Applied Physics Letter, Volume 82, Number 19, 2003.
11. COMSOL MULTIPHYSICS, version 3.3, *User Manual*, 2006.
12. Sze, S.M., *Semiconductor Devices, Physics and Technology*, 2nd edition, John Wiley & Sons, Inc., 2002.
13. Ohring, Milton, *Reliability and Failure of Electronic Materials and Devices*, Academic Press, 1998.

THIS PAGE INTENTIONALLY LEFT BLANK

INITIAL DISTRIBUTION LIST

1. Defense Technical Information Center
Ft. Belvoir, Virginia
2. Dudley Knox Library
Naval Postgraduate School
Monterey, California
3. Professor James H. Luscombe
Chairman, Department of Physics
Naval Postgraduate School
Monterey, California
4. Professor Dan Boger
Chairman, Department of Systems Engineering
Naval Postgraduate School
Monterey, California
5. Professor Nancy M. Haegel
Naval Postgraduate School
Monterey, California
6. Professor David Jenn
Naval Postgraduate School
Monterey, California
7. Dr. Thomas Boone
Hitachi Global Storage
San Jose, California
8. Dr. Matt Coleman
Fairfield University
Fairfield, Connecticut
9. Embassy of Greece, Military Attaché
Washington, DC
10. Pavlos Andrikopoulos
Hellenic Army General Staff, Artillery Directorate
Athens, Greece
11. Pavlos Andrikopoulos
Athens, Greece